

A probabilistic view on transport and mixing in closed and open flows

Der Fakultät Management und Technologie
der Leuphana Universität Lüneburg
zur Erlangung des Grades

Doktor der Naturwissenschaften
– Dr. rer. nat. –

genehmigte Dissertation von Anna Klünker

geboren am 04.03.1989 in Hildesheim

Eingereicht am: 25.01.2023

Mündliche Verteidigung (Disputation) am: 22.6.2023

Erstbetreuerin und -gutachterin: Prof. Dr. Kathrin Padberg-Gehle

Zweitgutachter: Prof. Dr. Péter Koltai

Drittgutachter: Prof. Dr. Peter Niemeyer

Erschienen unter dem Titel: A probabilistic view on transport and mixing in closed and open flows

Druckjahr: 2023

Elektronisch veröffentlicht durch die Bibliothek der Leuphana Universität Lüneburg

Abstract

The computational analysis and the optimization of transport and mixing processes in fluid flows are of ongoing scientific interest. Transfer operator methods are powerful tools for the study of these processes in dynamical systems. The focus in this context has been mostly on closed dynamical systems and the main applications have been geophysical flows. In this thesis, we consider transport and mixing in closed flow systems and in open flow systems that mimic technical mixing devices.

Via transfer operator methods, we study the coherent behavior in closed example systems including a turbulent Rayleigh-Bénard convection flow and consider the finite-time mixing of two fluids. We extend the transfer operator framework to specific open flows. In particular, we study time-periodic open flow systems with constant inflow and outflow of fluid particles and consider several example systems. In this case, the transfer operator is represented by a transition matrix of a time-homogeneous absorbing Markov chain restricted to finite transient states. The chaotic saddle and its stable and unstable manifolds organize the transport processes in open systems. We extract these structures directly from leading eigenvectors of the transition matrix. For a constant source of two fluids in different colors, the mass distribution in the mixer and its outlet region converges to an invariant mixing pattern. In parameter studies, we quantify the degree of mixing of the resulting patterns by several mixing measures.

More recently, network-based methods that construct graphs on trajectories of fluid particles have been developed to study coherent behavior in fluid flow. We use a method based on diffusion maps to extract organizing structures in open example systems directly from trajectories of fluid particles and extend this method to describe the mixing of two types of fluids.

Zusammenfassung

Die computergestützte Analyse und Optimierung von Transport- und Mischprozessen in Fluidströmungen ist von anhaltendem wissenschaftlichem Interesse. Leistungsfähige Werkzeuge für die Untersuchung dieser Prozesse in dynamischen Systemen sind Transferoperator-Methoden. Hierbei lag der Fokus bisher weitestgehend auf geschlossenen dynamischen Systemen und die wesentlichen Anwendungen waren geophysikalische Strömungen. In dieser Arbeit betrachten wir Transport- und Mischprozesse in geschlossenen Strömungssystemen und in offenen Strömungssystemen, die technische Mischvorrichtungen nachahmen.

Mit Hilfe von Transferoperator-Methoden untersuchen wir das kohärente Verhalten in geschlossenen Beispielsystemen, einschließlich einer zweidimensionalen turbulenten Rayleigh-Bénard-Konvektionsströmung, und betrachten das Mischen von zwei Fluiden in endlicher Zeit. Wir erweitern das Transferoperator-Framework für spezielle offene Systeme. Insbesondere untersuchen wir zeitperiodische offene Systeme mit konstantem Zu- und Abfluss von Fluidteilchen und betrachten verschiedene Beispielsysteme. Der Transferoperator wird in diesem Fall durch eine Übergangsmatrix einer zeithomogenen absorbierenden Markovkette approximiert, die auf endlich viele transiente Zustände beschränkt ist. Der chaotische Sattel und seine stabile und instabile Mannigfaltigkeiten organisieren die Transportprozesse in offenen Systemen. Wir extrahieren diese Strukturen direkt aus führenden Eigenvektoren der Übergangsmatrix. Für eine konstante Quelle von zwei verschiedenfarbigen Fluiden konvergiert die Massenverteilung im Mischer und seiner Auslassregion zu einem invarianten Mischungsmuster. In Parameterstudien bestimmen wir die Mischgüte der resultierenden Muster mit verschiedenen Mischmaßen.

In jüngerer Zeit wurden netzwerkbasierte Methoden entwickelt, die Graphen auf den Trajektorien von Fluidteilchen konstruieren, um das kohärente Verhalten in Fluidströmungen zu untersuchen. Wir verwenden eine auf Diffusion Maps basierende Methode, um organisierende Strukturen in offenen Beispielsystemen direkt aus den Trajektorien von Fluidteilchen zu extrahieren, und erweitern diese Methode, um das Mischen von zwei Arten von Fluiden zu beschreiben.

Acknowledgements

The biggest thanks goes to my supervisor, Prof. Dr. Kathrin Padberg-Gehle, for her kindness and her many offers of help and for her constant support and motivation to bring this thesis to existence. I am very grateful for the support of Professor Jean-Luc Thiffeault at the University of Wisconsin-Madison, with whom I had the honor of working on a publication along with my supervisor. I am thankful for Prof. Dr. Péter Koltai and Prof. Dr. Peter Niemeyer for serving as the second and third examiners of the dissertation. At this point, I would also like to thank Prof. Dr. Péter Koltai for inviting me to visit him and his research group at the FU Berlin and for his time for discussions. For further fruitful discussions, I want to thank Associate Professor Sanjeeva Balasuriya at the University of Adelaide and Prof. Dr. Alexandra von Kameke at the TUHH. Further, I thank the latter and Eike Steuwe for providing me with a data set. Special thanks go to Lisa Klünker, Saskia Schwedes and Lena Dammann for proofreading parts of this thesis. Moreover, I want to thank my colleagues at the institute for the warm atmosphere. At this point, I would especially like to thank my former colleague Dr. Christiane Schneide, with whom I shared the office for a few years. I am grateful for the partial support of this research by the Deutsche Forschungsgemeinschaft within the Priority Programme DFG-SPP 1881 on Turbulent Superstructures. A special thanks for having my back during the final process goes to Lorenz Peisker. Finally, I would like to express a deep gratitude to my family, who made it possible and encouraged me to study mathematics in the first place.

Contents

1. Introduction	1
2. Basic concepts and definitions	7
2.1. Autonomous dynamical systems	7
2.2. Nonautonomous dynamical systems	11
2.3. Open dynamical systems	12
2.4. Ergodic theory	13
2.5. Markov chains	14
2.5.1. Basic definitions	14
2.5.2. Canonical form of a transition matrix	16
2.5.3. Spectrum, stationary distribution and quasi-stationary distribution	17
2.5.4. Expected residence times	21
3. Set-oriented description of transport in closed systems	23
3.1. Transfer operator	23
3.2. Organizing structures	26
3.2.1. Autonomous coherent structures	26
3.2.2. Nonautonomous coherent structures	29
3.2.3. Finite-time entropy.	32
4. Set-oriented description of mixing	35
4.1. Modeling	36
4.2. Quantification	36
5. Transport and mixing studies in closed systems	39
5.1. Double gyre flow	40
5.1.1. Coherent structures in the double gyre flow with windage	41
5.1.2. Mixing of two types of fluids	49
5.2. Rayleigh-Bénard convection flow	52
5.2.1. Extraction of organizing structures	53
5.2.2. Mixing of two types of fluids	58
6. Set-oriented description of transport in open systems	61
6.1. Conditional transfer operator	61
6.2. Transport in double-open systems	63
6.3. Organizing structures	65

7. Transport and mixing studies in open systems	69
7.1. The double gyre mixer	70
7.1.1. Organizing structures	71
7.1.2. Mixing of two types of fluids	79
7.2. The lid-driven cavity mixer.	82
7.2.1. Organizing structures.	83
7.2.2. Mixing of two types of fluids	84
7.3. A channel with an obstacle	85
8. Trajectory-oriented description of transport and mixing	89
8.1. Theory and numerics	89
8.2. Example systems	92
8.2.1. Double gyre flow	92
8.2.2. Double gyre mixer	93
8.2.3. Channel with an obstacle	98
9. Conclusion	105
A. SEBA	109
B. Double gyre systems	110
C. RBC	114
List of figures	119
Bibliography	126

Chapter 1.

Introduction

Transport and mixing processes in fluid flows can be observed in a wide variety of natural and industrial systems, such as the global ocean and chemical reactors. The interest of research ranges from modeling and analysis to optimization of the underlying processes. This includes the understanding and identification of different fluid regimes in the dynamics, in a wider sense for example the evolution of oil or garbage patches in the ocean [1–3], and the enhancing of mixing in industrial devices, such as stirred-tank reactors or microfluidic devices [4–6].

When we ignore molecular diffusion, the advection of fluid particles can be presented by a deterministic dynamical system. Idealized fluid particles follow passively trajectories that are solutions of

$$\dot{\mathbf{x}} = \mathbf{u}(\mathbf{x}, t),$$

where \mathbf{u} is a velocity field, \mathbf{x} ($\in \mathbb{R}^3$ or \mathbb{R}^2) is the position of the particle and t is the time. If we consider the transport on a two dimensional domain $X \subset \mathbb{R}^2$ and the flow is incompressible, the velocity field $\mathbf{u} = (u_1, u_2)$ can be derived of a stream function $\Psi : X \times \mathbb{R} \rightarrow X$ as

$$u_1 = \frac{\partial \Psi}{\partial x_2}, \quad u_2 = -\frac{\partial \Psi}{\partial x_1}.$$

In case the underlying velocity field \mathbf{u} is time-dependent, the motion of the fluid particles is in general chaotic. The concept of chaotic advection was introduced by Aref [4] more than three decades ago. Since then, the dynamical systems perspective on advection in fluid flow has inspired a multitude of scientific works (see [7] for a review).

When we observe the advection of a scalar (representing for example a blob of dye) in a closed chaotic flow, small scale structures are created by repeated actions of stretching and folding. By taking now into account molecular diffusion, which by itself is a very slow process, the small scale structures are then blended further to homogeneity. In this way, chaotic advection can also be used to enhance the mixing in microfluidic devices, where the Reynolds number is small and mixing by turbulence is not possible [7, 8, p. 13].

Coherent structures act as organizers of the transport and mixing processes. Over the last two decades, a number of different Lagrangian based approaches have been proposed to detect coherent behavior in fluid flow (see [9, 10] for a review and comparison).

Geometric approaches aim to detect Lagrangian coherent structures (LCSs), which are robust material lines in 2D and material surfaces in 3D that form transport barriers and organize the remaining trajectory patterns. The concepts are based on the construction of the Cauchy-Green strain tensor field. Ridges in the derived finite-time Lyapunov exponent (FTLE) field [11] indicate hyperbolic (repelling and attracting) LCSs (see [12] for further developments).

The main focus in this thesis will be probabilistic transfer operator approaches within a set-oriented numerical framework that aim to detect maximally coherent regions that minimally mix with the surrounding phase space. Dellnitz and Hohmann developed a set-oriented framework for the approximation of a global attractor in a dynamical system [13]. Based on these ideas, Dellnitz and Junge [14, 15] developed a transfer operator method for the approximation of spatially fixed regions in phase space with low escape probability – so-called almost-invariant sets – and components of invariant sets that are almost cyclically permuted – so-called almost-cyclic sets (see also in [16, 17] for further extensions).

The methods are based on the Perron-Frobenius operator, which evolves densities. In a closed setting, this transfer operator is a Markov operator with spectrum in the unit circle. The Ulam approximation [18] of the transfer operator generates a transition matrix of a finite-state Markov chain. An eigenvector with unit eigenvalue corresponds to a stationary distribution. Under some assumptions, any initial distribution converges to this stationary distribution. The rate of mixing is then determined by the second largest eigenvalue, which controls the exponential rate at which an initial distribution approaches the stationary distribution. Eigenvectors corresponding to real eigenvalues close to one contain information about almost-invariant sets [15].

Froyland et al. [19, 20] extended the transfer operator framework to the identification of time-asymptotic and finite-time coherent sets, mobile regions that minimally mix with the surrounding region (see also [21, 22]). Subdominant singular vectors of numerically approximated transfer operators approximate finite-time coherent sets.

Transfer operators contain also information about finite-time expansive behavior along trajectories. The finite-time entropy (FTE) field, approximated from the transition matrix, captures nonlinear stretching directly from the entropy growth experienced by a small localized density evolved by the transfer operator [23]. The FTE field can be considered as a probabilistic analogy of the FTLE field [9].

The transfer operator methods have been applied to many different dynamical systems. Applications in fluid flows of these approaches are (mainly) geophysical flows as oceanic [1, 24–26] and atmospheric flows [27].

The transfer operator framework relies on the addition of small amount of diffusion. In the zero-diffusion limit, one arrives the dynamic Laplacian operator [28]. Coherent sets can be identified by dominant eigenfunctions of this operator and can be geometrically characterized by having boundary to volume ratios that remain minimal under the evolution of the dynamic. The recently developed finite-element approach [29] to approximating the dynamic Laplacian provides a robust method for sparse trajectory data.

Also, very recently, data-based or trajectory based approaches have been developed that consider trajectories as nodes in a network or graph, see [30–34]. These methods work also for sparse trajectory data, whereas the approximation of the transfer operator (aside from the dynamic Laplacian) requires the computation of relatively many short trajectories. Here, we apply the numerical scheme developed by Banisch and Koltai [34] based on diffusion maps, which generates a Markov chain on the given trajectories. The introduced diffusion map transition matrix in this method can be considered as a data-based averaged transfer operator and can be connected to the dynamic Laplacian.

Much research has focused on the study of closed flows but there is a small but growing literature on open systems. The restriction of the dynamics to certain almost-invariant sets within the transfer operator framework would lead to open dynamical systems with small escape rates [35]. The transfer operator method was extended to the identification of almost-invariant sets in certain open dynamical systems containing a hole by Froyland et al. using a closing scheme [36]. A slightly different closing technique of an open system was used in [3]. Since in many application areas for example modeling of plankton dynamics [37] and design of industrial mixers, one has to deal with open flows, characterized by constant in- and outflows (double-open systems), this topic remains an important one and much remains to be done.

In open systems, chaotic advection proceeds differently than in closed system, as typical fluid particles leave the domain in finite time and the outgoing fluid is only partially mixed [7, 37]. Some rare fluid particles may have trapped orbits confined on a fractal structure with Lebesgue measure zero – this is called the chaotic saddle [38–40]. The existence of such a chaotic saddle influences the transport and mixing tremendously: fluid patches near its stable manifold are transported to a neighborhood of the chaotic saddle, where they will be repeatedly stretched and folded before they flow out along its unstable manifold. Open flows can also contain stable regions, so called KAM islands, from which fluid does not escape. Whereas in closed flows the existence of KAM islands prevent mixing to homogeneity, it can enhance mixing in open flows by holding particles longer in the mixing region [7, 37].

Several mixing measures that quantify the degree of mixedness of a density field have been introduced [41–44]. In open flows, residence time distributions have been considered to measure the mixing efficiency [45]. Furthermore, the fractal dimension of the stable (or equivalently of the unstable) manifold measures the strength of mixing [37]. Persistent patterns or strange eigenmodes, related to eigenfunctions of a transfer operator in the limit of small diffusivity, have been studied for closed [46–51] and open flows [45, 52]. The derived eigenmode index is a mixing measure in open flows [45].

Based on Sobolev space norms of negative index as the mix-norm [42], optimal stirring protocols were designed [6, 44, 53–56]. Optimal mixing based on the transfer operator or its generator were considered in [57–59]. Beside these concepts to optimize velocity fields by perturbations to enhance mixing, one can also consider the problem of finding the optimal initial distributions for a given system, see for example in [60].

In this thesis, we consider transport and mixing processes of fluid particles first in closed and then in open non-dissipate systems. We present transfer-operator based studies in closed flows. We propose a transfer operator framework to model and study mixing in open flows with in- and outflow and present studies in example systems. Finally, we extend a trajectory-based method and present studies in closed and open example systems. In more detail, the contribution of this thesis splits into the following parts:

1. Set-oriented aspects and applications of transport and mixing in closed systems.

- We study the robustness of almost-invariant sets and coherent sets under a constant perturbation (windage) in the well-studied periodically forced double gyre flow [61].
- We apply the transfer operator approach to a turbulent Rayleigh-Bénard convection (RBC) system in a two-dimensional setting [62]. We extract coherent sets and FTE fields, which we compare with the respective FTLE fields. In particular, we study the robustness of the results with respect to the numerical approximation of the transfer operator. We have already published parts of the study of coherent behavior in [63], together with a study of coherent behavior in a three-dimensional setting.
- We model the mixing for two types of fluids within the transfer operator approach, describe mixing measures that can be applied in this setting and consider mixing in the double gyre flow and the RBC system.

2. Set-oriented aspects and applications of transport and mixing in specific open systems.

- We propose a computational approach based on transfer operators that allows us to study transport and mixing in specific models of open flows.

In particular, we consider 2D time-periodic open systems, where a constant inflow and outflow of mass (double-open systems) can be realized. The domains of these systems have the form of a channel with an inlet and outlet region and a compact mixing region. Our specific setting is inspired by mixing devices that can be realized experimentally [45, 52, 64] and can be seen as an idealized model of an open flow mixer.

We describe the evolution of densities by means of a substochastic transition matrix, resulting from a finite-rank approximation of a Perron–Frobenius operator for the open system. We use the recent description of a flux through a Markov chain [65] to model further a constant inflow of new mass, which leads to an affine transformation involving the numerical transfer operator. See also [66] for related Markov chain models of mixing processes.

Additionally, the proposed framework allows us to extract the crucial organizing structures relevant for mixing, such as the chaotic saddle and its

manifolds, as well as expected residence times from the transition matrix with negligible additional computational effort.

- We construct open example systems by combining initially closed systems with a background flow that transports fluid particles through a compact phase space region where the periodic mixer acts. Here, we construct open versions of the double gyre flow [61] and the lid-driven cavity flow [67], which are known to exhibit extended regions of stretching and folding.

We study the underlying organizing structures (chaotic saddle and its manifolds). We model transport in these systems with a given inflow distribution and study and quantify how two types of fluids for different system parameters are mixed. In particular, the resulting limit outflow pattern corresponding to the partially mixed fluid is a fixed point of the affine transformation. The partially-mixed fluid can then be analyzed by means of different established mixing measures. For the double gyre mixer we additionally consider the influence of the constant source and examine how the mixing quality can be quantified from the underlying structures.

We have already published the proposed framework and a part of the studies in [68].

- As a third example system serves a model of a magnetic mixing valve [69], where we extract organizing structures with the transfer operator method. The mixing valve can be considered as a channel with an obstacle, which creates a mixing region.

3. Trajectory-oriented aspects and applications of transport and mixing in closed and open systems.

- We model mixing for two types of fluids in closed and (double) open systems within a trajectory-based framework based on the diffusion map transition matrix [34].
- We revisit some of the previously considered example systems within the trajectory-based approach. We apply mixing measures in the closed double gyre system, extract organizing structures in the (double open) double gyre mixer and model transport (including a constant source of new trajectories) and mixing of two types of fluids in the mixing valve and extract underlying organizing structures.

This thesis is structured as follows:

In **Chapter 2** we begin by introducing definitions and concepts from dynamical systems theory, ergodic theory and Markov chains theory.

In **Chapter 3** we describe the transport of densities in closed flows within a transfer operator approach. We review the numerical approximation of the transfer operator as transition matrix of a Markov chain and the extraction of coherent structures as almost-invariant sets and coherent sets.

In **Chapter 4** we describe briefly the mixing of two types of fluids within the set oriented framework, and discuss several measures for the quantification of mixing, such as the variance or multiscale mix-norm.

In **Chapter 5** we present our transfer operator based transport and mixing studies in closed example flows, the double gyre flow and the two-dimensional turbulent RBC system.

In **Chapter 6** we describe the transport of densities in particular (double) open flows within a transfer operator approach. Furthermore, we discuss the organizers of open flow mixing, such as the chaotic saddle and its manifolds, and their numerical approximation.

In **Chapter 7** we present our transfer operator based transport and mixing studies in open example flows, the double gyre mixer and the lid-driven-cavity mixer and the mixing valve.

In **Chapter 8** we describe transport and mixing within a trajectory-oriented approach for closed and open flows. We describe briefly the numerical extraction of organizing structures and the modeling and quantification of mixing of two types of fluids. Finally, we present studies in example systems, the closed double gyre system, the (double open) double gyre flow and the mixing valve.

We conclude this thesis with a discussion in **Chapter 9**.

Chapter 2.

Basic concepts and definitions

In this chapter, we present relevant definitions and concepts from dynamical systems theory, ergodic theory and Markov chain theory, which will serve as reference for the following chapters. For an overview on some of the presented concepts, we refer to the textbooks [70–74].

In Section 2.1 and Section 2.2 we introduce autonomous dynamical systems and nonautonomous dynamical systems. Section 2.3 presents open dynamical systems as extension of the better-known closed systems. Section 2.4 provides measure theoretic definitions from ergodic theory. Finally, in Section 2.5 we introduce Markov chains.

2.1. Autonomous dynamical systems

We start with the definition of an *autonomous dynamical system*:

Definition 2.1.1. Let $(\mathbb{T}, +)$ be a semigroup with neutral element 0. Let $\mathcal{S} = \{S_t\}_{t \in \mathbb{T}}$ be a family of transformations on a manifold $X \subset \mathbb{R}^d$. The triple $(\mathcal{S}, X, \mathbb{T})$ is an *autonomous dynamical system* if

- (1.) $S_0(\mathbf{x}) = \mathbf{x}$ for all $\mathbf{x} \in X$;
- (2.) $S_{t_1+t_2}(\mathbf{x}) = S_{t_1}(S_{t_2}(\mathbf{x}))$ for all $t_1, t_2 \in \mathbb{T}$ and $\mathbf{x} \in X$; and
- (3.) the mapping $(t, \mathbf{x}) \mapsto S_t(\mathbf{x})$ is continuous;

are satisfied.

X is called the *phase space* and \mathbb{T} is the *time*. S_t is the *time- t -map* of the *evolution* \mathcal{S} . The time \mathbb{T} can be either continuous (\mathbb{R} or $\mathbb{R}_{\geq 0}$), or discrete (\mathbb{Z} or \mathbb{N}_0). In the discrete case, the continuity in (t, \mathbf{x}) in (3.) reduces to the continuity in \mathbf{x} .

Remark. The family of transformations $\mathcal{S} = \{S_t\}_{t \in \mathbb{T}}$ together with the function composition is a semigroup. It is a group when $(\mathbb{T}, +)$ is a group. In this sense, some authors differentiate further between *semi-dynamical systems* and *dynamical systems* (also in [70, p. 191]) but here we will call both dynamical systems. Besides, the continuity property is often omitted from the definition of a dynamical system.

The set $O(\mathbf{x}) := \{S_t(\mathbf{x}) : t \in \mathbb{T}\}$ is called *trajectory* or *orbit* for $\mathbf{x} \in X$. If $O(\mathbf{x}) = \{\mathbf{x}\}$, the trajectory is a *fixed point*. The trajectory is *periodic* if there is a period $\omega > 0$ such that $S_{t+\omega}(\mathbf{x}) = S_t(\mathbf{x})$ for all $t \in \mathbb{T}$, otherwise it is *aperiodic*. If $S_{t_1}(\mathbf{x}) \neq S_{t_2}(\mathbf{x})$ for all $t_1 \neq t_2$ with $t_1, t_2 \in \mathbb{T}$, the trajectory is *nonintersecting*. An aperiodic trajectory has to be nonintersecting.

Example 2.1.2. Consider a system of ordinary differential equations (ODEs) on X

$$\dot{\mathbf{x}}(t) = \mathbf{u}(\mathbf{x}(t)),$$

where unique solutions $S_t(\mathbf{x}_0) := \mathbf{x}(t)$ with initial value $\mathbf{x}(0) = \mathbf{x}_0$ exist for all $\mathbf{x}_0 \in X$. Then $(\{S_t\}_{t \in \mathbb{R}}, X, \mathbb{R})$ is an example of a *continuous dynamical system*.

We will often consider discrete dynamical systems that are generated by the iteration of a single transformation S :

Example 2.1.3. Let $S : X \rightarrow X$ be a homeomorphism on X and let $\{S_t : X \rightarrow X\}_{t \in \mathbb{N}_0}$ be the family of mappings with

$$S_t(\mathbf{x}) := S^t(\mathbf{x}) = \underbrace{S \circ \dots \circ S}_{t \text{ times}}(\mathbf{x}) \quad t \in \mathbb{N}_0.$$

Then the triple $(\{S_t\}_{t \in \mathbb{N}_0}, X, \mathbb{N}_0)$ represents a (non-invertible) *discrete autonomous dynamical system*. Since S is invertible we can extend the time to \mathbb{Z} by defining

$$S_{-t}(\mathbf{x}) := S^{-t}(\mathbf{x}) = \underbrace{S^{-1} \circ \dots \circ S^{-1}}_{t \text{ times}}(\mathbf{x}) \quad t \in \mathbb{N}_0.$$

The triple $(\{S_t\}_{t \in \mathbb{Z}}, X, \mathbb{Z})$ represents then an *invertible discrete autonomous dynamical system*.

Remark. We can naturally construct a discrete dynamical system from a system of ODEs as in Example 2.1.2 by choosing S to be the shift map for a fixed time τ along the trajectories, that is, $S = S_\tau$.

A set A is called a *forward invariant set* if

$$S_t(A) \subset A \quad \text{for } t > 0.$$

A set A is called a *backward invariant set* if

$$S_t(A) \subset A \quad \text{for } t < 0.$$

A set that is a forward and backward invariant set is called an *invariant set*. In other words, a set A is an *invariant set* if

$$S_t(A) = A \quad \text{for } t \in \mathbb{T}.$$

A fixed point $A_1 = \{\mathbf{x}\}$ and a periodic trajectory $A_2 = \{S_t(\mathbf{x}) \mid 0 \leq t \leq \omega\}$ are simple examples of invariant sets.

In the following, let $d(\mathbf{x}, \mathbf{y}) := \|\mathbf{x} - \mathbf{y}\| = \sqrt{\sum_{i=1}^d (x_i - y_i)^2}$ denote the Euclidean distance between two points $\mathbf{x}, \mathbf{y} \in X \subset \mathbb{R}^d$. We define the distance between a point $\mathbf{x} \in X$ and a set $A \subset X$ as $d(\mathbf{x}, A) := \inf_{\mathbf{y} \in A} d(\mathbf{x}, \mathbf{y})$.

Many invariant sets are limit sets of trajectories. The ω -limit set of \mathbf{x} is defined as

$$\omega(\mathbf{x}) = \{\mathbf{y} \in X \mid \exists \text{ a sequence } t_j \rightarrow \infty \text{ such that } S_{t_j}(\mathbf{x}) \rightarrow \mathbf{y}\}.$$

Elements of $\omega(\mathbf{x})$ are called ω -limit points of \mathbf{x} .

A closed invariant set A is an *attracting set* if there is some neighborhood U of A such that $S_t(\mathbf{x}) \in U$ for $t \geq 0$ and $S_t(\mathbf{x}) \rightarrow A$ as $t \rightarrow \infty$, for all $\mathbf{x} \in U$.

Remark. In non-dissipative (or fluid-like) systems attracting sets cannot arise. However, we will also consider *open* systems, where the limit points of almost all points lie in a *hole* H (relevant definitions are given in Section 2.3).

A bounded aperiodic trajectory that does not converge to a periodic trajectory and is unstable is called a *chaotic trajectory*. We define a *chaotic invariant set* following [72, p. 737]:

Definition 2.1.4. A compact invariant set A is a *chaotic invariant set* if

- (1.) $S_t(\mathbf{x})$ has sensitive dependence on initial conditions on A , that is, if there exists an $\epsilon > 0$ such that, for any $\mathbf{x} \in A$ and any neighborhood U of \mathbf{x} , there exists $\mathbf{y} \in U$ and $t > 0$ such that $d(S_t(\mathbf{x}), S_t(\mathbf{y})) > \epsilon$; and
- (2.) A is topologically transitive, that is, if for any two open subsets $U, V \subset A$ there is a $t \in \mathbb{T}$ such that $S_t(U) \cap V \neq \emptyset$.

'*Hyperbolicity*' is an important term in the development of dynamical systems when chaotic behavior occurs.

Definition 2.1.5. Let $S : X \rightarrow X$ a diffeomorphism, generating an discrete autonomous dynamical system as in Example 2.1.3. Let Λ be an invariant set. A *hyperbolic structure* for Λ is a continuous invariant direct sum decomposition $T_\Lambda X = E_\Lambda^u \oplus E_\Lambda^s$ with the property that there are constants $c > 0$, $0 < \lambda < 1$ such that

- (1.) if $\mathbf{v} \in E_\mathbf{x}^u$, then $\|DS^{-n}(\mathbf{x})\mathbf{v}\| \leq c\lambda^n \|\mathbf{v}\|$ and
- (2.) if $\mathbf{v} \in E_\mathbf{x}^s$, then $\|DS^n(\mathbf{x})\mathbf{v}\| \leq c\lambda^n \|\mathbf{v}\|$.

Here, $T_\Lambda X$ consists of all tangent vectors to X at all points of Λ and DS denotes the derivative of S . Let $T_\mathbf{x} X$ denote the tangent space at $\mathbf{x} \in \Lambda$. The direct sum splitting holds for all for all $\mathbf{x} \in \Lambda$, that is $T_\mathbf{x} X = E_\mathbf{x}^u \oplus E_\mathbf{x}^s$ is a direct sum splitting of this vector space into subspaces with dimensions u and s ($u + s = d$). The continuity of the splitting means that $E_\mathbf{x}^u$ and $E_\mathbf{x}^s$ depend continuously on \mathbf{x} . The invariance means that $DS(\mathbf{x})E_\mathbf{x}^u = E_{S(\mathbf{x})}^u$ and $DS(\mathbf{x})E_\mathbf{x}^s = E_{S(\mathbf{x})}^s$. Vectors in E_Λ^s are contracted by DS in forward time and vectors in E_Λ^u are contracted in backward time.

The following theorem, also known as the stable manifold theorem for hyperbolic sets, provides a characterization of the behavior of points close to an invariant hyperbolic set, and leads to a characterization of the chaotic behavior within the set. We follow the presentation by [71, p. 246]:

Theorem 2.1.6. (*Hirsch and Pugh, 1970*): *Let $\Lambda \subset X$ be an invariant set with a hyperbolic structure $E_\Lambda^u \oplus E_\Lambda^s$ of a C^r diffeomorphism S . Then there is an $\epsilon > 0$ and there are two collections of differentiable manifolds $W_\epsilon^s(\mathbf{x})$ and $W_\epsilon^u(\mathbf{x})$, $\mathbf{x} \in \Lambda$, which have the following properties:*

$$(1.) \quad W_\epsilon^s(\mathbf{x}) = \{\mathbf{y} \in X : d(S^j(\mathbf{y}), S^j(\mathbf{x})) < \epsilon \text{ for all } j \geq 0\} \text{ and} \\ W_\epsilon^u(\mathbf{x}) = \{\mathbf{y} \in X : d(S^{-j}(\mathbf{y}), S^{-j}(\mathbf{x})) < \epsilon \text{ for all } j \geq 0\}.$$

$$(2.) \quad T_{\mathbf{x}}W_\epsilon^s(\mathbf{x}) = E_{\mathbf{x}}^s \text{ and } T_{\mathbf{x}}W_\epsilon^u(\mathbf{x}) = E_{\mathbf{x}}^u.$$

$$(3.) \quad \text{There are constants } c > 0, 0 < \lambda < 1 \text{ such that} \\ d(S^j(\mathbf{y}), S^j(\mathbf{x})) \leq c\lambda^j d(\mathbf{x}, \mathbf{y}) \quad \text{for } \mathbf{y} \in W_\epsilon^s(\mathbf{x}), j \geq 0, \text{ and} \\ d(S^{-j}(\mathbf{y}), S^{-j}(\mathbf{x})) \leq c\lambda^j d(\mathbf{x}, \mathbf{y}) \quad \text{for } \mathbf{y} \in W_\epsilon^u(\mathbf{x}), j \geq 0.$$

$$(4.) \quad W_\epsilon^s(\mathbf{x}) \text{ and } W_\epsilon^u(\mathbf{x}) \text{ are continuously dependent on } \mathbf{x}.$$

We can now define the *global stable* and *global unstable manifolds* of $\mathbf{x} \in \Lambda$ by

$$W^s(\mathbf{x}) = \bigcup_{j \geq 0} S^{-j}(W_\epsilon^s(S^j(\mathbf{x}))) \quad \text{and} \quad W^u(\mathbf{x}) = \bigcup_{j \geq 0} S^j(W_\epsilon^u(S^{-j}(\mathbf{x}))).$$

The *stable* and *unstable manifolds* of Λ are given by

$$W^s(\Lambda) = \bigcup_{\mathbf{x} \in \Lambda} W_\epsilon^s(\mathbf{x}) \quad \text{and} \quad W^u(\Lambda) = \bigcup_{\mathbf{x} \in \Lambda} W_\epsilon^u(\mathbf{x}).$$

In particular, they are characterized by

$$W^s(\Lambda) := \{\mathbf{y} \in X : d(S^j(\mathbf{y}), S^j(\Lambda)) \rightarrow 0 \text{ for } j \rightarrow \infty\} \text{ and} \\ W^u(\Lambda) := \{\mathbf{y} \in X : d(S^{-j}(\mathbf{y}), S^{-j}(\Lambda)) \rightarrow 0 \text{ for } j \rightarrow \infty\}.$$

The simplest example of a hyperbolic invariant set is a hyperbolic fixed point $\{\mathbf{x}\}$, that is, a fixed point for which the Jacobian matrix $DS(\mathbf{x})$ has no eigenvalues on the unit circle.

A more complex example is generated by the well-known Smale's horseshoe map, first introduced in [75]. On a square Q the map is defined by vertically compressing the square, then stretching it horizontally, and then folding it back onto itself, see Figure 2.1. Here, the invariant hyperbolic set is a Cantor-like set. This map can be seen as an abstraction of the action of stretching and folding in dynamical systems that is the cause of chaos. In [72, Chapter 23] one finds a detailed description of a horseshoe-like map, the construction of the invariant set and a precise description of the chaotic dynamics. However, when one considers the dynamics only on the square Q , this is not a (closed) dynamical system as

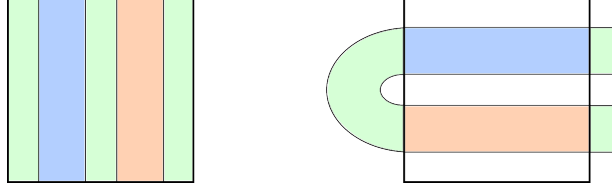


Figure 2.1.: One iteration of the Smale's horseshoe map contracts the square (left), expands it, folds it around into the shape of a horseshoe and places it back on itself (right).

in Definition 2.1.1 (and the map is not a diffeomorphism). Instead, this can be considered as an example of an open dynamical system, which we will introduce in Section 2.3. It can be fixed to a closed system by extending the domain by two half-discs, one on the left and the other on the right side of the square.

Hyperbolic invariant sets are examples of nonattracting chaotic invariant sets, that is, a *chaotic saddle*. 'Chaotic saddle' is a newer term in the development of dynamical systems that has become popular in the last three decades, see in [72, p. 756] for a more detailed historical overview. A chaotic saddle has typically a Cantor-like structure and can be hyperbolic or nonhyperbolic [76], [40, p. 83].

2.2. Nonautonomous dynamical systems

We now want to consider systems that depend not only on the elapsed time but also on the actual time t .

For a time set \mathbb{T} we define $\mathbb{T}_{\geq}^2 = \{(t_1, t_0) \in \mathbb{T} \times \mathbb{T} : t_1 \geq t_0\}$.

Definition 2.2.1. We consider a transformation $\mathcal{S} : \mathbb{T}_{\geq}^2 \times X \rightarrow X$. We call $(\mathcal{S}, X, \mathbb{T})$ a *nonautonomous dynamical system* if the following properties are satisfied:

- (1.) $\mathcal{S}(t_0, t_0, \mathbf{x}) = \mathbf{x}$ for all $\mathbf{x} \in X$ and $t_0 \in \mathbb{T}$;
- (2.) $\mathcal{S}(t_2, t_0, \mathbf{x}) = \mathcal{S}(t_2, t_1, \mathcal{S}(t_1, t_0, \mathbf{x}))$ for all $(t_1, t_2), (t_1, t_0) \in \mathbb{T}_{\geq}^2$ and $\mathbf{x} \in X$;
and
- (3.) the mapping $(t, t_0, \mathbf{x}) \mapsto \mathcal{S}(t, t_0, \mathbf{x})$ is continuous.

By writing $S_{t_1, t_0}(\mathbf{x}) := \mathcal{S}(t_1, t_0, \mathbf{x})$, we can interpret $\mathcal{S} = \{S_{t_1, t_0}\}_{(t_1, t_0) \in \mathbb{T}_{\geq}^2}$ as a family of transformations on X .

Remark. This is not the only possible way of defining a nonautonomous dynamical system. In [77] two ways are presented: the above definition that followed the definition of processes by [78] and a second common way that uses an autonomous dynamical system as driving system, which is also used for the definition of a random dynamical system (cf. [79]).

Example 2.2.2. Consider a system of ordinary differential equations of the form

$$\dot{\mathbf{x}}(t) = \mathbf{u}(\mathbf{x}(t), t),$$

where unique solutions $\mathcal{S}(t, t_0, \mathbf{x}_0) := \mathbf{x}(t)$ with initial value $\mathbf{x}(t_0) = \mathbf{x}_0$ exist for all $\mathbf{x}_0 \in X, t_0 \in \mathbb{R}$. Then $(\mathcal{S}, X, \mathbb{R})$ is an example of a *continuous nonautonomous dynamical system*.

Example 2.2.3. Consider

$$\mathbf{x}_{n+1} = S_n(\mathbf{x}_n),$$

where $S_n : \mathbb{R}^d \rightarrow \mathbb{R}^d, n \in \mathbb{Z}$, are continuous mappings. The solutions are given as

$$\mathcal{S}(t, t_0, \mathbf{x}_0) := S_{t-1} \circ \dots \circ S_{t_0}(\mathbf{x}_0)$$

for all $t, t_0 \in \mathbb{Z}$ with $t > t_0$ and $\mathbf{x}_0 \in X$ with initial value $\mathcal{S}(t_0, t_0, \mathbf{x}_0) := \mathbf{x}(t_0) = \mathbf{x}_0$. The triple $(\mathcal{S}, \mathbb{R}^d, \mathbb{Z})$ is an example of a *discrete nonautonomous dynamical system*.

We often use analogue definitions from the autonomous systems for nonautonomous systems. For example, A is an *invariant set* if

$$\mathcal{S}(t, t_0, A) = A \quad \text{for all } (t, t_0) \in \mathbb{T}_{\geq}^2.$$

A less strictly definition is the following: A family of sets $\{A_t\}_{t \in \mathbb{T}}$ is called *invariant* if $\mathcal{S}(t, t_0, A_{t_0}) = A_t$ for all $(t, t_0) \in \mathbb{T}_{\geq}^2$.

2.3. Open dynamical systems

Open dynamical systems refer to systems, where trajectories can escape the phase space through a boundary or by falling into a hole. In many real world problems it is natural to have an open system instead of a closed system. Early work on open dynamical systems can be found in [80], where the authors considered the dynamics on a billiard table with a small hole.

A common way to construct an open dynamical system is the following (cf. [81]):

Consider an autonomous dynamical system generated by transformation S on X . We want to study the dynamics on a subset $A \subset X$ for which $S(A) \cap A \neq \emptyset$ and $S(A) \not\subset A$. $H = X \setminus A$ is called a *hole*. Once a trajectory enters H , that is, $S^n(\mathbf{x}) \in H$, we not longer track it, it has fallen in the hole. The system that is generated by the restriction of S to the subset A is an *open dynamical system*.

More generally, one could think of considering nonautonomous systems with moving holes, see for example in [82].

We formulate the following general definition of an open dynamical system:

Definition 2.3.1. Let $(\mathcal{S}, X, \mathbb{T})$ be an autonomous (resp. nonautonomous) dynamical system. Let A be a subset of X (or a family of subsets $\{A_t\}_{t \in \mathbb{T}}$) that is not forward invariant. Once trajectories enter the *hole* $H := X \setminus A$ (resp. the

hole $H_t := X \setminus A_t$ at time t), we not longer track them. Let \mathcal{S}_A be the family of transformations containing the transformations S_t restricted to A (resp. transformations S_{t,t_0} restricted to A_t). We call $(\mathcal{S}_A, A, \mathbb{T})$ an *open dynamical system*.

Remark. In this thesis, we consider open systems with a relatively large ‘hole’ that is fixed in space.

For $\mathbf{x} \in A$, the smallest $n > 0$ such that $S^n(\mathbf{x}) \in H$ is called its *time of escape*, also referred to as *survival time*, *residence time* or *killing time*. An analogous concept for an open dynamical system with holes in Markov chain theory is a Markov chain with absorbing states, where we find matching terms, described in Section 2.5.

2.4. Ergodic theory

In studying transport and mixing we are concerned with the evolution of densities rather than single trajectories. Therefore, we equip the phase space X with a Borel-structure. Let $(X, \mathcal{B}(X), \mu)$ be a probability space, where $\mathcal{B}(X)$ denotes the Borel- σ algebra of X and $\mu : \mathcal{B}(X) \rightarrow [0, 1]$ is a probability measure. This means, $\mu(X) = 1$ and μ is σ -additive, that is, $\mu(\bigcup_{i \in I} A_i) = \sum_{i \in I} \mu(A_i)$ for all countable collections of pairwise disjoint sets $\{A_i\}_{i \in I}$.

A transformation $S : X \rightarrow X$ is *measurable* if $S^{-1}(A) \in \mathcal{B}(X)$ for all $A \in \mathcal{B}(X)$, where $S^{-1}(A)$ denotes the set-theoretic inverse or preimage of A .

Definition 2.4.1. Let $S : X \rightarrow X$ be a measurable transformation.

1. S is called *non-singular* if $\mu(A) = 0$ implies $\mu(S^{-1}(A)) = 0$ for all $A \in \mathcal{B}(X)$.
2. The measure μ is *invariant* under S if $\mu(S^{-1}(A)) = \mu(A)$ for all $A \in \mathcal{B}(X)$. When this holds, we also say that the transformation S is *measure-preserving*.
3. A measure-preserving transformation S is *ergodic* if either $\mu(A) = 0$ or $\mu(A) = 1$ for all invariant sets A .
4. A measure-preserving transformation S is called *mixing* if

$$\lim_{k \rightarrow \infty} \mu(A_1 \cap S^{-k}(A_2)) = \mu(A_1) \mu(A_2) \quad \text{for all } A_1, A_2 \in \mathcal{B}(X). \quad (2.1)$$

This means, that for any two measurable subsets A_1 and A_2 the proportion of particles starting in A_1 and ending in A_2 is given asymptotically as the product of $\mu(A_1)$ and $\mu(A_2)$.

Remark. The above definitions can be generalized for a family of transformations $\{S_t\}_{t \geq 0}$ on X . For example, a family $\{S_t\}_{t \geq 0}$ of measure-preserving transformations is mixing if

$$\lim_{t \rightarrow \infty} \mu(A_1 \cap S_t^{-1}(A_2)) = \mu(A_1) \mu(A_2) \quad \text{for all } A_1, A_2 \in \mathcal{B}(X).$$

The evolution of a density f under a transformation S can be described by a transfer operator:

Definition 2.4.2. Let $S : X \rightarrow X$ be a nonsingular transformation. The *Perron-Frobenius* operator $\bar{P} : L^1(X) \rightarrow L^1(X)$ corresponding to S is defined by

$$\int_A \bar{P}f d\mu = \int_{S^{-1}A} f d\mu \quad \text{for all } A \in \mathcal{B}(X), f \in L^1(X). \quad (2.2)$$

More on Perron-Frobenius operators can be found in [83, Chapter 3]. We will state some of its properties in the next chapter.

Let us now consider an important definition for open dynamical systems. Consider a subset $A := X \setminus H$, where H is a measurable set. Let μ_A be a probability measure on A .

Definition 2.4.3. μ_A is *conditional invariant* or *quasi invariant* under $S_A : A \rightarrow X$ if

$$\mu_A(S^{-1}(B)) = \mu_A(B) \cdot \mu_A(S^{-1}(A)) \quad \text{for all measurable } B \subset A.$$

The factor $\mu_A(S^{-1}(A))$ describes here the proportion of mass that will stay in A under one iterate of S . In case $\mu_A(S^{-1}(A)) = 1$, μ_A is an invariant measure.

2.5. Markov chains

In the next chapters, we will model the dynamics of a dynamical system by a Markov chain. By discretizing the domain of an dynamical system, we introduce a small amount of noise in the former deterministic system. As we will see in the next chapter, the discretized transfer operators are transition matrices of Markov chains. When we consider open systems, we deal with transition matrices of absorbing Markov chains. This section provides the relevant background theory from the Markov chain theory. We first introduce basic definitions, which can be found for example in the textbook [73]. Then we define a canonical form of a transition matrix to explore in a next step spectral properties and identify stationary and quasi-stationary distributions. Finally, we present expected residence times, which will serve to identify organizing structures in open dynamical systems.

2.5.1. Basic definitions

A *Markov chain* is a stochastic process $(Y_k)_{k \in \mathbb{N}_0}$ that takes values on a finite or countable set M (state space) and has the Markov property (memorylessness), that is,

$$\mathbb{P}(Y_{k+1} = j \mid Y_k = i, Y_{k-1} = i_{k-1}, \dots, Y_0 = i_0) = \mathbb{P}(Y_{k+1} = j \mid Y_k = i).$$

Let now M be a finite state space. The *transition matrix* $\bar{P}(k)$ for a given time $k \in \mathbb{N}_0$ is the matrix that contains the entries

$$\bar{P}_{ij}(k) := \mathbb{P}(Y_{k+1} = j \mid Y_k = i).$$

A Markov chain is *time-homogeneous* if the transition matrix $\bar{P}(k)$ is the same for all times $k \in \mathbb{N}_0$. In the following, we assume the Markov chain is time-homogeneous and we denote the transition matrix by \bar{P} .

A state j is *accessible* or *reachable* from state i , denoted as $i \rightarrow j$, if there is a nonzero probability to reach j after a finite number of steps when starting from i , that is, $(\bar{P}^k)_{ij} > 0$ for some $k \in \mathbb{N}_0$. A state i is said to *communicate* with state j if $i \rightarrow j$ and $j \rightarrow i$.

A *communicating class* C is a maximal set of states such that every pair of states in C communicates with each other. A communicating class C_j is accessible from another communicating class C_i , denoted as $C_i \rightarrow C_j$, if there is a state in C_j that is accessible from a state in C_i . A communicating class C that is accessible from itself we refer to as a *self-communicating class*. A communicating class that consists of more than one state is always self-communicating.

A Markov chain is said to be *irreducible* if it is possible to get to any state from any state (one communicating class). If there is more than one communicating class the Markov chain is *reducible*.

Remark. Consider the directed graph that is induced by the transition matrix, the state transition diagram. In terms from graph theory, a communicating class refers to a ‘strongly connected component’.

We now state some properties of states:

1. A state i is said to be *transient* if, given that we start in state i , there is a non-zero probability that we never return to i . Otherwise it is *recurrent*. A recurrent state i is said to be *positive recurrent* if the mean time to return to this state is finite.
2. A state i is called an *absorbing state* or *sink* if $\bar{P}_{ij} = 0$ for all $j \neq i$, so in this state mass is accumulating. A Markov chain is *absorbing* if every state eventually reaches an absorbing state. All states that are nonabsorbing are then transient.
3. A state i is *essential* if for all j with $i \rightarrow j$ also $j \rightarrow i$, and there is at least one j with $i \rightarrow j$. That is, i is absorbing or i communicates with all states that are accessible from i . Otherwise i is *inessential* (and hence transient).
4. A state i is *periodic* with period d if it is the greatest common divisor of those k for which $(\bar{P}^k)_{ii} > 0$. If there is no periodic state the Markov chain is called *aperiodic*.

Remark. As a state we can call a communicating class ‘(positive) recurrent’, ‘transient’, ‘essential’, ‘inessential’, ‘absorbing’ or ‘periodic with period d ’. This causes no problems, because these state properties are class properties, meaning that if one state in the communicating class has one of these properties all states in the class have the same property.

A communicating class C is called *closed* if $\bar{P}_{ij} = 0$ for all $i \in C$ and $j \notin C$, that is, if the class is essential.

An irreducible Markov chain that is aperiodic and positive recurrent is *ergodic*. Observe that a finite closed class is always positive recurrent. Hence, an aperiodic irreducible Markov chain on a finite state space is ergodic.

2.5.2. Canonical form of a transition matrix

Consider a reducible Markov chain on a finite state space $M = \{1, \dots, N\}$ with set of communicating classes $\mathcal{C} = \{\bar{C}_1, \bar{C}_2, \dots, \bar{C}_k, C_1, C_2, \dots, C_r\}$, where $\bar{C}_1, \dots, \bar{C}_k$ are the essential classes and C_1, \dots, C_r the inessential (transient) classes.

Assume that the states are sorted by communicating classes, that is, if $i, j \in A$, there is no $h \in B$ for which $i > h > j$ for all $A, B \in \mathcal{C}$ with $A \neq B$. Further the states are sorted such that for a state i and a state j : $i > j$ if

1. $i \in A$ and $j \in B$ with $A \rightarrow B$ for all $A, B \in \mathcal{C}$ with $A \neq B$, or
2. i is inessential and j is essential.

Then the $N \times N$ transition matrix \bar{P} has the *canonical form* of a general non-negative matrix (following [73, p. 14]):

$$\bar{P} = \left[\begin{array}{ccc|c} \bar{P}_1 & & 0 & 0 \\ & \ddots & & \vdots \\ 0 & & \bar{P}_k & 0 \\ \hline & R & & P \end{array} \right], \quad P = \begin{bmatrix} P_1 & & 0 \\ \vdots & \ddots & \\ * & \dots & P_r \end{bmatrix} \quad (2.3)$$

The diagonal blocks $\bar{P}_1, \dots, \bar{P}_k$ denote here the (stochastic) transition matrices restricted to the essential classes $\bar{C}_1, \dots, \bar{C}_k$ and the blocks P_1, \dots, P_r denote the (substochastic) transition matrices restricted to the inessential classes C_1, \dots, C_r . P may have nonzero entries to the left of any of its diagonal blocks – describing the transition probabilities between different inessential classes. The submatrix R describes the transition probabilities between the inessential states and the essential states.

Let us now consider the transition matrix of a reducible absorbing Markov chain. The only essential states are then absorbing states. Let $M_a = \{1, \dots, N - n\}$ denote the set of $k = N - n$ absorbing states and let $M_{tr} = \{N - n + 1, \dots, N\}$ denote the set of n non-absorbing states. The *canonical form* of the transition matrix of a reducible absorbing Markov chain is given as:

$$\bar{P} = \begin{bmatrix} I & 0 \\ R & P \end{bmatrix}, \quad P = \begin{bmatrix} P_1 & & 0 \\ \vdots & \ddots & \\ * & \dots & P_r \end{bmatrix}, \quad (2.4)$$

where I denotes the $(N - n) \times (N - n)$ identity matrix – this is the submatrix of \bar{P} restricted to the absorbing states – and P denotes the $n \times n$ submatrix of \bar{P} restricted to the non-absorbing states. Each block P_i is the transition matrix restricted to the transient class C_i . R is now the $n \times (N - n)$ submatrix that describes the proportions of mass that flows from the transient states to the absorbing states.

2.5.3. Spectrum, stationary distribution and quasi-stationary distribution

The transition matrix \bar{P} is nonnegative. In case \bar{P} is irreducible, the well-known Perron-Frobenius Theorem gives the spectral properties:

Theorem 2.5.1. (*Perron-Frobenius Theorem*). *Let A be a nonnegative and irreducible $n \times n$ matrix. Then A has a simple positive real eigenvalue λ (the Frobenius-Perron eigenvalue) which is equal to its spectral radius. There are corresponding unique (up to a scalar) left and right λ -eigenvectors $\mathbf{w}, \hat{\mathbf{w}} > 0$ (component-wise), that is,*

$$\mathbf{w}A = \lambda\mathbf{w} \text{ and } A\hat{\mathbf{w}} = \lambda\hat{\mathbf{w}}.$$

If A is additionally aperiodic, there is no other eigenvalue with same absolute value as λ .

Since \bar{P} is stochastic, it can be followed that $\lambda = 1$ and the right 1-eigenvector $\hat{\mathbf{w}}$ is the all-ones vector. The corresponding (normalized) positive real left 1-eigenvector \mathbf{w} is the unique *stationary distribution* on M , that is, $\sum_i w_i = 1$ and

$$\sum_{i \in M} w_i \bar{P}_{ij} = w_j.$$

Moreover,

$$\sum_{i \in M} w_i (\bar{P}^k)_{ij} = w_j \quad \text{for all } k \in \mathbb{N}. \quad (2.5)$$

Remark. The normalized nonnegative left 1-eigenvector \mathbf{w} defines a discrete invariant probability measure ν on M with $\nu(B) := \sum_{i \in B} w_i, B \subset M$.

If the Markov chain is additionally aperiodic, the stationary distribution is the limit distribution for an arbitrary initial distribution \mathbf{p} , that is,

$$\lim_{k \rightarrow \infty} \mathbf{p}\bar{P}^k = \mathbf{w}.$$

In the reducible case, \bar{P} has the form of a lower triangular block matrix as in equation (2.3). The spectrum of \bar{P} is determined by the union of spectra of all \bar{P}_i . Each submatrix \bar{P}_i is irreducible and has a Frobenius-Perron eigenvalue λ_i . For the closed classes $\lambda_i = 1$ and for the inessential classes $0 \leq \lambda_i < 1$. The nonnegative left 1-eigenvectors of \bar{P} are stationary distributions. For each closed class \bar{C}_i there is a (up to scalar multiples) unique left 1-eigenvector \mathbf{w} of \bar{P} such that $w_j > 0$ if $j \in \bar{C}_i$ and $w_j = 0$ otherwise. If \mathbf{w} is a nonnegative left 1-eigenvector, then \mathbf{w} is a linear combination with nonnegative coefficients of these eigenvectors. For each closed class \bar{C}_i there is a right 1-eigenvector $\hat{\mathbf{w}}$ with all entries for states in the respected closed communicating class are 1 and else zero. The only closed classes of an absorbing Markov chain are the absorbing states and the stationary distributions are restricted to these states.

Let us now consider the submatrix P of an absorbing Markov chain. P is substochastic and has the form of a lower triangular block matrix as in equation

(2.4), where a block P_i on the diagonal is the transition matrix for transient communicating class C_i . P_i is irreducible and substochastic and has Frobenius-Perron eigenvalue λ_i , $0 \leq \lambda_i < 1$. Classes that are not self-communicating consist only of one single state and their blocks have eigenvalue 0. Therefore, the non-zero part of the spectrum of P is determined by the spectrum of P restricted to self-communicating classes (cf. [84])

Let now T denote the survival time $T := \inf\{k \geq 0 \mid Y_k \in M_a\}$. The normalized nonnegative left x -eigenvectors \mathbf{w} of P are *quasi-stationary distributions* on M_{tr} (cf. [84]), that is, $\sum_i w_i = 1$ and

$$\mathbb{P}_{\mathbf{w}}(Y_k = j \mid T > k) = w_j \quad \text{for all } j \in M_{tr}, k \in \mathbb{N}, \quad (2.6)$$

where $\mathbb{P}_{\mathbf{w}}(\cdot) := \sum_i w_i \mathbb{P}(\cdot \mid Y_0 = i)$. Since the chain has survived until k if $Y_k = j$ and $j \in M_{tr}$, the condition (2.6) can be written as

$$\mathbb{P}_{\mathbf{w}}(Y_k = j) = \mathbb{P}_{\mathbf{w}}(T > k) \cdot w_j \quad \text{for all } j \in M_{tr}, k \in \mathbb{N}. \quad (2.7)$$

For more details on quasi-stationary distributions, we also refer to the book [74].

Observe that the condition (2.5) for a stationary and the condition (2.7) for a quasi-stationary distribution differ by the factor $\mathbb{P}_{\mathbf{w}}(T > k)$ on the right hand side of the equation. For $k = 1$, this factor is the eigenvalue x , since $\mathbb{P}_{\mathbf{w}}(T > 1) = \mathbf{w}P\mathbf{1} = x\mathbf{w}\mathbf{1} = x$, where $\mathbf{1}$ denotes the all-ones vector. Thus, the eigenvalue x is the survival probability for initial distribution \mathbf{w} .

Remark. The normalized nonnegative left x -eigenvector \mathbf{w} defines a discrete quasi-invariant probability measure ν on M_{tr} with $\nu(B) := \sum_{i \in B} w_i$, $B \subset M_{tr}$.

Summarized results on identifying all nonnegative left eigenvectors and consequently all quasi-stationary distributions can be found in [84], which we will present in the following theorem. For this, we need an additional definition: A class C_i is called a *maximal class* if $\lambda_j < \lambda_i$ for all $j \neq i$ such that $C_i \rightarrow C_j$.

Theorem 2.5.2. [84]

- (1.) *There exists a nonnegative left x -eigenvector of P if and only if there exists a maximal class C_i such that $x = \lambda_i$.*
- (2.) *If C_i is a maximal class, then there is a (up to scalar multiples) unique left λ_i -eigenvector \mathbf{w} of P such that $w_j > 0$ if j is accessible from C_i and $w_j = 0$ otherwise.*
- (3.) *If \mathbf{w} is a nonnegative left x -eigenvector of P , then w is a linear combination with nonnegative coefficients of the eigenvectors defined in (2.) corresponding to the maximal classes C_i with $x = \lambda_i$.*

For the right eigenvectors we can conclude the following:

Corollary 2.5.3. (1.) *There exists a nonnegative right x -eigenvector of P if and only if there exists a maximal class C_i of P^T such that $x = \lambda_i$.*

(2.) If C_i is a maximal class of P^T , then there is a (up to scalar multiples) unique right λ_i -eigenvector $\hat{\mathbf{w}}$ of P such that $\hat{w}_j > 0$ if C_i is accessible from j and $\hat{w}_j = 0$ otherwise.

(3.) If $\hat{\mathbf{w}}$ is a nonnegative right x -eigenvector of P , then $\hat{\mathbf{w}}$ is a linear combination with nonnegative coefficients of the eigenvectors defined in (2.) corresponding to the maximal classes C_i with $x = \lambda_i$.

Remark. P and P^T have the same communicating classes but not always the same maximal classes.

Under some assumptions, a quasi-stationary distribution is the limiting conditional distribution for an initial distribution \mathbf{p} , that is,

$$\lim_{k \rightarrow \infty} \mathbb{P}_{\mathbf{p}}(Y_k = j \mid T > k) = w_j.$$

In the simplest case, P itself is irreducible and aperiodic, then there is a unique quasi-stationary distribution \mathbf{w} , which is the limiting conditional distribution for all initial distributions \mathbf{p} [85]. A generalization for the reducible case is presented in [84].

Signed x -eigenvectors of P can reveal states that can be reached or can reach a (not necessarily maximal) self-communicating class. We can relatively easily show that states in the support of a left (or right) eigenvector corresponding to a nonzero eigenvalue can be reached (or can reach) a self-communicating class:

Proposition 2.5.4. *Let $x \neq 0$. If there is a left x -eigenvector \mathbf{w} of P such that $w_i > 0$ or $w_i < 0$, then a self-communicating class can reach i . If there is a right x -eigenvector $\hat{\mathbf{w}}$ such that $\hat{w}_i > 0$ or $\hat{w}_i < 0$, then i can reach a self-communicating class.*

Proof. Let $i = i_1$ be a state that cannot be reached from a self-communicating class and let P be in the canonical form. Assume that there is a left eigenvector \mathbf{w} with $w_{i_1} \neq 0$ such that

$$\begin{aligned} \mathbf{w}P &= x\mathbf{w} \\ \Leftrightarrow (\dots, w_{i_1}, \dots, w_{i_2}, \dots)P &= x(\dots, w_{i_1}, \dots, w_{i_2}, \dots). \end{aligned}$$

Since i_1 is not self-communicating, the corresponding block to this state is the 1×1 matrix $P_{i_1 i_1} = 0$. At least one state i_2 that can reach i_1 in one time step has to be a nonzero entry w_{i_2} . Since i_2 itself cannot be reached from a self-communicating class and is not self-communicating, there has to be a state i_3 with nonzero entry w_{i_3} that can reach i_2 and cannot be reached from a self-communicating class, and so on. Since we have only finite states this leads to a contradiction.

Analogously one can follow that there cannot be a right eigenvector $\hat{\mathbf{w}}$ with $\hat{w}_i \neq 0$ for a state i that cannot reach a self-communicating class. \square

In the next example, we study the left eigenvectors when there are two self-communicating classes. In particular, we consider the case where one of the self-communicating classes is accessible from the other.

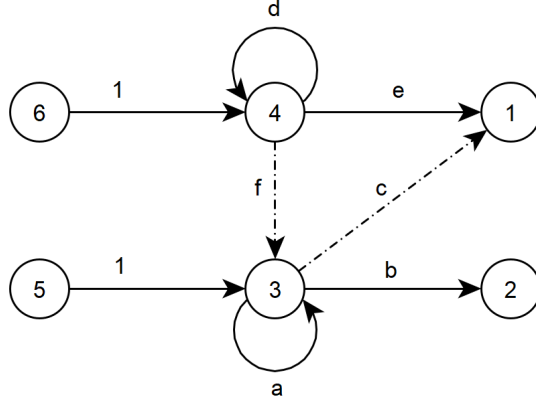


Figure 2.2.: State-transition diagram (restricted to transient states) of an absorbing Markov chain with two self-communicating classes.

Example 2.5.5. Consider the following toy example of an absorbing Markov chain with transition matrix

$$P = \begin{pmatrix} 0 & 0 & 0 & 0 & 0 & 0 \\ 0 & 0 & 0 & 0 & 0 & 0 \\ c & b & a & 0 & 0 & 0 \\ e & 0 & f & d & 0 & 0 \\ 0 & 0 & 1 & 0 & 0 & 0 \\ 0 & 0 & 0 & 1 & 0 & 0 \end{pmatrix}$$

restricted to the transient states $\{1, 2, 3, 4, 5, 6\}$, where the transition probabilities a, b, d, e are positive and c and f are nonnegative. The corresponding state-transition diagram is presented in Figure 2.2.

The Markov chain has two self-communicating classes $C_1 = \{3\}$ and $C_2 = \{4\}$ with corresponding Frobenius-Perron eigenvalues a and d . All other eigenvalues of P are zero. For a left x -eigenvector \mathbf{w} holds:

$$\begin{aligned} \mathbf{w}P &= x\mathbf{w} \\ \Leftrightarrow (w_1, w_2, w_3, w_4, w_5, w_6)P &= x(w_1, w_2, w_3, w_4, w_5, w_6) \\ \Leftrightarrow (w_3c + w_4e, w_3b, w_3a + w_4f, w_4d + w_6, 0, 0) &= x(w_1, w_2, w_3, w_4, w_5, w_6). \end{aligned}$$

It follows directly that $w_5 = 0$ and $w_6 = 0$. Hence we have

$$(w_3c + w_4e, w_3b, w_3a + w_4f, w_4d, 0, 0) = x(w_1, w_2, w_3, w_4, 0, 0).$$

Assume now $f > 0$, that is, $C_2 \rightarrow C_1$.

First, we consider $x = a$ and the left a -eigenvector corresponding to the maximal class C_1 . By the above equations and since an eigenvector is by definition nonzero, we can follow that $w_4 = 0$ (since $f > 0$), $w_3 \neq 0$, $w_2 = \frac{b}{a}w_3$ and

$w_1 = w_3c$ (hence this entry is only nonzero if $c > 0$). The nonzero entries have the same sign and the eigenvector can be chosen to be nonnegative.

Now, we consider $x = d$ and the left d -eigenvector corresponding to class C_2 . For $a \neq d$, we can follow $w_3 = w_4 \frac{f}{d-a}$. We can consider three cases:

- If $a > d$ (only C_1 is a maximal class), it follows by the above equation that w_3 and w_4 have different signs. w_2 has the same sign as w_3 . w_1 has the same sign as w_4 if $c = 0$ or if $|w_4e| \geq |w_3c|$. In particular, $w_1 = 0$ if $|w_4e| = |w_3c|$.
- If $a < d$ (both C_1 and C_2 are maximal classes), it follows w_3 and w_4 have the same sign and further w_2 and w_1 have the same sign as w_3 and w_4 .
- If $a = d$ (only C_1 is a maximal class), it follows $w_4 = 0$, $w_2 = \frac{b}{a}w_3$ and $w_1 = w_3c$ (hence this entry is only nonzero if $c > 0$).

This shows: In case of two self-communicating classes, there has to be no eigenvector \mathbf{w} with $w_i \neq 0$ for a state i that can be reached by a self-communicating class. Here this is the case for state 4 (and also for state 1 if $c = 0$) when $a = d$. The eigenvalue has algebraic multiplicity 2 and geometric multiplicity 1.

Furthermore, the eigenvector \mathbf{w} corresponding to a non-maximal class may not reveal all states that can be reached by the class. Here this is the case when $a > d$ and the state 1 is reached from both self-communicating classes with same amount of signed mass. The entry of the d -eigenvector corresponding to state 1 is then 0.

2.5.4. Expected residence times

Let $(Y_k)_{k \in \mathbb{N}_0}$ be a homogeneous absorbing Markov chain and let P be the transition matrix restricted to the transient states M_{tr} . The expected number of time steps the chain is in M_{tr} before absorption, when starting in a given state $i \in M_{tr}$, is given as

$$\mathbb{E}(T \mid Y_0 = i) = \sum_{j \in M_{tr}} (I - P)_{ij}^{-1}.$$

We call $\mathbb{E}(T \mid Y_0 = i)$ the *expected residence time* of state i . One might also refer to it as *mean first passage time* from i to an absorbing state as e.g. in [73, p. 419]. The matrix $(I - P)^{-1}$ is called *fundamental matrix* of the absorbing Markov chain. A derivation of the above equation can be found for example in the textbook [86, p. 419]. In practice, we compute the expected residence times by solving the system of linear equations

$$(I - P)\mathbf{r} = \mathbf{1},$$

where the vector \mathbf{r} contains the entries $r_i := \mathbb{E}(T \mid Y_0 = i)$ and $\mathbf{1}$ denotes the all-ones vector.

More generally, one can compute the expected residence times for a set A of a (not necessarily absorbing) Markov chain $(Y_k)_{k \in \mathbb{N}_0}$ on finite state space M (see e.g. in [25] for an application). Let \bar{P}_A be the transition matrix \bar{P} restricted to the states in A . Assume that $\bar{P}_A^k \rightarrow 0$ as $k \rightarrow \infty$. The expected residence time to stay in A when starting in i is then given as

$$\sum_{j \in A} (I - \bar{P}_A)^{-1}_{ij}.$$

Chapter 3.

Set-oriented description of transport in closed systems

In this chapter, we address advective transport in closed flows. We follow a probabilistic approach, which considers the evolution of sets, or, more abstractly, densities of probability measures.

For simplicity, we assume that the flow consists of ideal fluid particles that move passively following a given fluid velocity $\mathbf{u}(\mathbf{x}, t)$ on a domain $X \subset \mathbb{R}^d$ ($d = 2$ or $d = 3$). The particle trajectories obey the ODE

$$\dot{\mathbf{x}}(t) = \mathbf{u}(\mathbf{x}(t), t), \quad \mathbf{x}(t_0) = \mathbf{x}_0 \in X. \quad (3.1)$$

Here, we restrict to incompressible flows, that is, with divergence $\nabla \cdot \mathbf{u} = 0$.

We now want to analyze the transport over a finite time-interval $[t_0, t_0 + \tau]$ in a closed system with compact domain $M \subset X$. In the closed case, we assume that M is an invariant set, such that no particle starting in M can leave M and no particle starting in $X \setminus M$ can enter M .

In the following, we describe the mathematical model setup for the transport in the general case, that \mathbf{u} is a nonautonomous velocity field, which includes the cases of nonautonomous periodic velocity fields and autonomous velocity fields.

In Section 3.1 we therefore introduce the Perron-Frobenius operator with some of its properties and describe its numerical approximation as transition matrix. Finally, we consider the transport over a series of time intervals, which leads to a homogeneous Markov chain when \mathbf{u} is a nonautonomous periodic or autonomous velocity field. Section 3.2 describes coherent structures that function as organizing structures and explains their numerical extraction from the transition matrix. At the end of the chapter, a nonlinear stretching measure is presented.

3.1. Transfer operator

To describe now the transport of a closed flow on M generated by the ODE in equation (3.1), we equip M with its Borel σ -algebra $\mathcal{B}(M)$ and a probability measure μ . We choose μ to be the normalized Lebesgue measure $\bar{\ell}$, that is, $\bar{\ell}(B) = \frac{\ell(B)}{\ell(M)}$ for all $B \in \mathcal{B}(M)$, where ℓ denotes Lebesgue measure (area or volume) on \mathbb{R}^d .

We define a measure-preserving transformation $S : M \rightarrow M$ with $S(\mathbf{x}_0) = \mathbf{x}(t_0 + \tau)$ that maps a particle $\mathbf{x}(t_0) \in M$ to its new position $\mathbf{x}(t_1)$ after a given

time step $\tau = t_1 - t_0$. In practice, we obtain the particle trajectories (and hence the final positions of the particles at time $t_0 + \tau$) by numerical integration methods like the classical Runge-Kutta method.

The evolution of a probability density $f \in L^1(M, \bar{\ell})$ or more general mass distributions $f \in L^1(M, \bar{\ell})$ such as signed densities under S can now be described by the Perron-Frobenius operator $\bar{\mathcal{P}}$ defined by (see equation (2.2)):

$$\int_B \bar{\mathcal{P}}f d\bar{\ell} = \int_{S^{-1}B} f d\bar{\ell} \quad \text{for all } B \in \mathcal{B}(M).$$

If f now denotes a mass distribution at time t_0 , the pushforward $\bar{\mathcal{P}}f$ describes the mass distribution at time $t_0 + \tau$.

We summarize some properties for the above defined Perron-Frobenius operator in the following theorem:

Theorem 3.1.1. *Let $\|\cdot\|$ denotes the L^1 norm, that is, $\|f\| := \int_M |f| d\bar{\ell}$. The above defined Perron-Frobenius operator $\bar{\mathcal{P}}$ satisfies:*

(1.) $\bar{\mathcal{P}}$ is a linear operator:

$$\bar{\mathcal{P}}(\lambda_1 f_1 + \lambda_2 f_2) = \lambda_1 \bar{\mathcal{P}}f_1 + \lambda_2 \bar{\mathcal{P}}f_2, \quad \text{for all } f_1, f_2 \in L^1(M, \bar{\ell}), \lambda_1, \lambda_2 \in \mathbb{R}.$$

(2.) $\bar{\mathcal{P}}f \geq 0$, for all $f \geq 0$, $f \in L^1(M, \bar{\ell})$.

(3.) $\|\bar{\mathcal{P}}f\| = \|f\|$ for all $f \geq 0$, $f \in L^1(M, \bar{\ell})$.

(4.) $\bar{\mathcal{P}}\mathbf{1}_M = \mathbf{1}_M$ due to measure-preservation of S .

The properties (1.)-(3.) make the Perron-Frobenius operator to a Markov operator. For a comprehensive overview on Markov operators and Perron-Frobenius operators, see e.g. in [70, Chapter 3].

Using Ulam's method [18] we obtain a finite-rank approximation of the infinite-dimensional transfer operator $\bar{\mathcal{P}}$ as a matrix \bar{P} . Following [15], we partition therefore the domain M into n connected sets B_i , $i = 1, \dots, n$, where $B_i \cap B_j = \emptyset$ for all $i \neq j$, which we call boxes in the following. The proportion of mass that is mapped from box B_i to B_j under S is given by the matrix entry

$$\bar{P}_{ij} = \frac{\bar{\ell}(B_i \cap S^{-1}(B_j))}{\bar{\ell}(B_i)} = \frac{\ell(B_i \cap S^{-1}(B_j))}{\ell(B_i)}, \quad (3.2)$$

where $S^{-1}(\cdot)$ denotes the preimage under S .

In practice, uniformly distributed test particles are initialized in box B_i . The entry \bar{P}_{ij} of the matrix \bar{P} is then estimated as the proportion of these particles that gets mapped to box B_j under the action of S .

In our applications, the domain M is a (generalized) rectangle. We use the software package GAIO [87] for the approximation of the transfer operator, where the partition elements B_i are obtained by successive bisectioning of M into smaller rectangles and using a binary tree for the storage. \bar{P} is typically a sparse matrix.

The matrix \bar{P} is row-stochastic and can be interpreted as the transition matrix of a Markov chain on a finite state space, where the boxes B_i , $i = 1, \dots, n$, are the states. In the discrete context, any $n \times 1$ row vector \mathbf{v}_0 represents now a mass distribution on M . Probability densities are represented by probability vectors $\mathbf{v}_0 \geq 0$ (component-wise), that is, $\sum_i v_{0,i} = 1$ – defining a discrete probability measure ν by $v_{0,i} = \nu(B_i)$. The interpretation of the \bar{P} -induced dynamics is that

$$\mathbf{v}_1 = \mathbf{v}_0 \bar{P}$$

is the pushforward of \mathbf{v}_0 under the discretized action of S .

Remark. The above definition and approximation of the Perron-Frobenius operator was given for the whole domain M . However, for computational reasons, in some applications a non-global version can be useful. Assume, we want to study the transport from a subset $M_1 \subset M$ to a small neighborhood M_2 of $S(M_1)$. The transfer operator from M_1 to M_2 can be approximated by (cf. [20]):

$$\bar{P}_{ij} = \frac{\ell(B_i \cap S^{-1}(\tilde{B}_j))}{\ell(B_i)}, \quad (3.3)$$

where $\{B_1, \dots, B_n\}$ is a partition of M_1 and $\{\tilde{B}_1, \dots, \tilde{B}_m\}$ is a partition of M_2 . The $n \times m$ matrix \bar{P}_{ij} is row-stochastic. When $M_1 = M_2 = M$ and $\{B_1, \dots, B_n\} = \{\tilde{B}_1, \dots, \tilde{B}_m\}$ we obtain the transition matrix as in equation (3.2).

Remark. When we want to study the transport on M over a series of time intervals $[t_0, t_1], [t_1, t_2], \dots, [t_k, t_{k+1}]$, we can construct a family of transition matrices $\{\bar{P}(i)\}_{i=0, \dots, k}$, where $\bar{P}(i)$ is the transition matrix with respect to the time interval $[t_i, t_{i+1}]$.

For a time-dependent (aperiodic) velocity field \mathbf{u} , the matrices $\bar{P}(0), \bar{P}(1), \dots, \bar{P}(k)$ are different in general. Let \mathbf{v}_i describe the mass distribution at time $t = t_i$. The mass distribution at time $t = t_{i+1}$ is then given as

$$\mathbf{v}_{i+1} = \mathbf{v}_i \bar{P}(i).$$

Starting with the initial distribution \mathbf{v}_0 , we have

$$\mathbf{v}_{i+1} = \mathbf{v}_0 \bar{P}(0) \cdot \bar{P}(1) \cdot \dots \cdot \bar{P}(i). \quad (3.4)$$

When \mathbf{u} is now an autonomous velocity field, $\bar{P}(i)$ only depends on the length $\tau = t_i - t_{i-1}$ of the time interval. When the length of all time intervals is the same, we have $\bar{P} := \bar{P}(0) = \bar{P}(1) = \dots = \bar{P}(k)$ for all time steps.

Further, when \mathbf{u} is a time-dependent periodic velocity field with period τ , that is, $\mathbf{u}(\mathbf{x}, t) = \mathbf{u}(\mathbf{x}, t + \tau)$, and the length of all time intervals is τ , we obtain $\bar{P} := \bar{P}(0) = \bar{P}(1) = \dots = \bar{P}(k)$.

In the last two cases, the equation (3.4) simplifies to

$$\mathbf{v}_{i+1} = \mathbf{v}_0 \bar{P}^i.$$

We can interpret \bar{P} as transition matrix of a time-homogeneous Markov chain and analyze the asymptotic behavior in terms of this Markov chain.

3.2. Organizing structures

Coherent structures are sets in the phase space that slowly mix with their neighborhood. Following [20, 88], we measure how coherent a structure is by the *coherence ratio*:

Definition 3.2.1. Given a reference probability measure μ on M , the *coherence ratio* for two sets $A_1, A_2 \subset M$ quantifies the fraction of mass transported from A_1 to A_2 under S and is given as

$$\rho_\mu(A_1, A_2) := \frac{\mu(A_1 \cap S^{-1}(A_2))}{\mu(A_1)}.$$

For all sets $A_1, A_2 \subset M$, $0 \leq \rho_\mu(A_1, A_2) \leq 1$. The coherence ratio is 0 if no mass flows from A_1 to A_2 under S and it is 1 if all of the mass of A_1 flows from A_1 to A_2 under S .

Consider a box-discretization $\{B_1, \dots, B_n\}$ of M . Let \bar{P} be the respective transition matrix. For box-discrete sets $A_1 = \bigcup_{i \in I} B_i$ and $A_2 = \bigcup_{j \in J} B_j$, $I, J \subset \{1, \dots, n\}$, the coherence ratio is approximated as (cf. [20])

$$\hat{\rho}_\mu(A_1, A_2) = \frac{\sum_{i \in I, j \in J} \mu(B_i) \bar{P}_{ij}}{\sum_{i \in I} \mu(B_i)}. \quad (3.5)$$

If $A_1 = A_2$, we also write $\rho_\mu(A_1) := \rho_\mu(A_1, A_1)$ and $\hat{\rho}_\mu(A_1) := \hat{\rho}_\mu(A_1, A_1)$.

In Subsection 3.2.1 we define autonomous coherent structures such as almost-invariant sets [15] in terms of the coherence ratio. In Subsection 3.2.2 we turn to nonautonomous coherent structures such as finite-time coherent sets [20]. Following [89], we define both the autonomous and nonautonomous coherent structures in a general time-dependent setting. We define the autonomous coherent structures for general invariant reference probability measures μ . We define coherent sets for a general reference probability measures μ , that has not to be invariant under S . However, in our applications, we will use the normalized Lebesgue measure as reference probability measure μ that is invariant under S .

3.2.1. Autonomous coherent structures

Autonomous coherent structures refer to coherent structures that are fixed in space. The simplest example of autonomous coherent structures are invariant sets, defined in Section 2.1 and Section 2.2. Let S maps a particle at initial time t_0 to its position after a time span τ . The next definition presents a finite-time version of an invariant set.

Definition 3.2.2. Let μ be an invariant reference probability measure on M . A set $A \subset M$ is called *S-invariant* (cf. [24]) if

$$\rho_\mu(A) = \frac{\mu(A \cap S^{-1}(A))}{\mu(A)} = 1.$$

That is, the set A remains unchanged under the evolution of S .

Remark. S -invariant sets include invariant sets in autonomous or nonautonomous dynamical systems defined in Section 2.1 and Section 2.2. But here, S -invariant sets can also include sets that obey the invariance principle only for that specific transformation S that maps a particle at initial time t_0 to its position after a time span τ and not for all other initial times or time spans. A more stricter definition was used in [24], where the invariance was considered over the time interval $[t_0, t_0 + \tau]$.

Assume that S is not ergodic and the domain decomposes into k S -invariant sets A_1, \dots, A_k that are preserved by the spatial discretization of the phase space M . This is the case, when the boundaries of the boxes lie on the boundaries of the invariant sets. The transition matrix \bar{P} is then reducible with k closed communicating classes $\bar{C}_1, \dots, \bar{C}_k$, which correspond to the k invariant sets. (In the closed setting, there cannot be transient communicating classes but only closed communicating classes for a measure preserving S .) Hence, \bar{P} has a k -fold eigenvalue 1.

The communicating classes can be extracted efficiently by using a graph-based approach such as Tarjan's algorithm [90].

However, in most cases the spatial discretization destroys all invariant sets apart from the phase space M and the respective transition matrix \bar{P} becomes irreducible or even ergodic. In the discretized space, A_1, \dots, A_k would instead be identified as sets with relatively large coherence ratio, so-called almost-invariant sets:

Definition 3.2.3. Let μ be an invariant reference probability measure on M . A set $A \subset M$ with $\mu(A) \neq 0$ is called (ρ_0, S) -almost-invariant (cf. [89]) if

$$\rho_\mu(A) = \frac{\mu(A \cap S^{-1}(A))}{\mu(A)} = \rho_0.$$

If $A \subset M$ is (ρ_0, S) -almost-invariant with $\rho_0 \approx 1$, then the probability (according to μ) of a trajectory leaving A at some time in $[t_0, t_0 + \tau]$ and not returning to A by time $t_0 + \tau$ is relatively small. This set obey an approximate invariance principle $S(A) \approx A$. In other words, A almost retains its shape under S . Such almost-invariant sets can be identified by means of eigenvectors of \bar{P} with real eigenvalue close to one [15, 22].

Remark. In [19] a ρ_0 -almost-invariant set is slightly stricter defined for the time interval $[t_0, t_0 + \tau]$. To differentiate invariant sets from almost-invariant sets: For truly invariant sets, eigenvalues converge to 1 as the number of boxes go to ∞ . The eigenvalues that correspond to truly almost-invariant are bounded by a number smaller 1.

We describe now the numerical extraction of almost-invariant sets from the transition matrix \bar{P} , following [16]. In this method, one uses a time-symmetrized transition matrix instead of directly \bar{P} .

An approximation of the invariant reference probability measure μ on M is given by the left 1-eigenvector \mathbf{p} of \bar{P} , where $\mu(B_i) = p_i$, $i = 1, \dots, n$. We form

the transition matrix \bar{P}^R of the time-reversed Markov chain of \bar{P} via

$$\bar{P}_{ij}^R = \frac{p_j \bar{P}_{ji}}{p_i}.$$

Remark. If S is volume preserving and the boxes B_i have the same size, all entries of \mathbf{p} are in theory equal and hence also $\bar{P}^R = \bar{P}^T$.

Then we form the time-symmetric matrix

$$R = (\bar{P} + \bar{P}^R)/2.$$

R is a transition matrix of a reversible Markov chain with stationary distribution \mathbf{p} . Observe, that the coherence ratio $\hat{\rho}_\mu(A, A)$ defined in equation (3.5) does not change if \bar{P} is substituted by \bar{P}^R or R .

First, we consider and restate the maximization problem and its solution to obtain two optimal almost-invariant sets in [16]. We want to find a partition of M into two optimal almost-invariant sets of similar measure, A and A^c , that maximize the coherence ratio under set-oriented discretization:

$$\max_{\substack{A=\bigcup_{i \in I} B_i, A^c=\bigcup_{i \in J} B_i \\ I \cup J = \{1, \dots, n\}, I \cap J = \emptyset}} \{ \hat{\rho}_\mu(A) + \hat{\rho}_\mu(A^c) : (\mu(A) - \mu(A^c))^2 < \epsilon \}$$

where ϵ is small. The constraint $(\mu(A) - \mu(A^c))^2 < \epsilon$ makes sure, that the measures of A and A^c are similar. Because of this, we drop the denominators $\mu(A) = \sum_{i \in I} p_i$ and $\mu(A^c) = \sum_{i \in J} p_i$ of the coherence ratios $\hat{\rho}_\mu(A)$ and $\hat{\rho}_\mu(A^c)$ and obtain the following problem:

$$\max_{\substack{I \cup J = \{1, \dots, n\}, \\ I \cap J = \emptyset}} \left\{ \sum_{i,j \in I} p_i R_{ij} + \sum_{i,j \in J} p_i R_{ij} : \left(\sum_{i \in I} p_i - \sum_{i \in J} p_i \right)^2 < \epsilon \right\}$$

An equivalent minimization problem is:

$$\min_{\substack{I \cup J = \{1, \dots, n\}, \\ I \cap J = \emptyset}} \left\{ 4 \left(1 - \sum_{i,j \in I} p_i R_{ij} - \sum_{i,j \in J} p_i R_{ij} \right) : \left(\sum_{i \in I} p_i - \sum_{i \in J} p_i \right)^2 < \epsilon \right\}$$

We reformulate the problem by writing the constraint into the denominator of the cost function (cf. [16]):

$$\min_{\substack{I \cup J = \{1, \dots, n\}, \\ I \cap J = \emptyset}} \frac{4(1 - \sum_{i,j \in I} p_i R_{ij} - \sum_{i,j \in J} p_i R_{ij})}{1 - (\sum_{i \in I} p_i - \sum_{i \in J} p_i)^2}$$

Consider a vector $\mathbf{x} \in \{-1, 1\}^n$, where entry $x_i = 1$ for $i \in I$, that is, the corresponding box belongs to A , and $x_i = -1$ for $i \in J$, that is, the corresponding box belongs to A^c . We obtain the equivalent problem (cf. [16]):

$$\min_{\substack{I \cup J = \{1, \dots, n\}, \\ I \cap J = \emptyset \\ x_i = 1, i \in I \\ x_i = -1, i \in J}} \frac{\sum_{i,j} p_i R_{ij} (x_i - x_j)^2}{\sum_i p_i x_i^2 - (\sum_i p_i x_i)^2}$$

Constructing the optimal \mathbf{x} is a difficult combinatorial problem. By allowing the vector to take other values than ± 1 , we obtain the relaxed minimization problem (cf. [16]):

$$\min_{\mathbf{x} \text{ is nonconstant}} \frac{\sum_{i,j} p_i R_{ij} (x_i - x_j)^2}{\sum_i p_i x_i^2 - (\sum_i p_i x_i)^2}.$$

By Rayleigh's theorem, the above problem is solved by $\mathbf{x} = \boldsymbol{\vartheta}_2$ with value $2(1 - \lambda_2)$, where $\boldsymbol{\vartheta}_2$ is the right eigenvector corresponding to the second largest eigenvalue λ_2 of R [16].

Remark. Since the matrix R is reversible, there exist theoretical lower and upper bounds of the maximal coherence ratio for a box-discrete set A with $\mu(A) \leq \frac{1}{2}$ in terms of the second largest real eigenvalue λ_2 of R [16]:

$$1 - \sqrt{2(1 - \lambda_2)} \leq \max_{A=\bigcup_{i \in I} B_i} \hat{\rho}_\mu(A) \leq \frac{1 + \lambda_2}{2}.$$

The signed vector entries of $\boldsymbol{\vartheta}_2$ can be interpreted as relaxations of the indicator function of the set A and its complement. Thus the vector $\boldsymbol{\vartheta}_2$ defines fuzzy almost-invariant sets on M . We use now $\boldsymbol{\vartheta}_2$ to divide the phase space M into two almost-invariant sets, A and A^c , maximizing

$$\hat{\rho}_\mu(A, A) + \hat{\rho}_\mu(A^c, A^c), \quad (3.6)$$

where $A = \bigcup_{\vartheta_{2,i} > b} B_i$ and $A^c = \bigcup_{\vartheta_{2,i} \leq b} B_i$. Choosing $b = 0$ will lead to two almost-invariant sets with similar measures. When we allow the sets to have measures that differ from $\frac{1}{2}$, we choose a b that maximizes (3.6). Since $\boldsymbol{\vartheta}_2$ has only finitely many entries, one can choose the optimal $b = b^*$ from the set of entries $\{\vartheta_{2,1}, \dots, \vartheta_{2,n}\}$ by a simple line search. The sets $A = \bigcup_{\vartheta_{2,i} > b^*} B_i$ and $A^c = \bigcup_{\vartheta_{2,i} \leq b^*} B_i$ are the optimal almost-invariant sets [16].

However, there are often $k > 2$ eigenvalues close to one (followed by a spectral gap) whose corresponding eigenvectors highlight the location of almost-invariant sets. To obtain a partition into k almost-invariant sets, one can use more information from the further eigenvectors $\boldsymbol{\vartheta}_3, \dots, \boldsymbol{\vartheta}_k$ of R [16]. One can postprocess the k leading eigenvectors by a k -means clustering [91]. Alternatively, to preserve the eigenspace structure, one can project the eigenvectors to a sparse basis (SEBA) [92], where the entries of each vector denote likelihoods that the underlying box B_i belongs to a specific almost-invariant set (see Chapter A). Hard assignment of boxes to sets may then be performed by thresholding [92]. The approach to find k almost-invariant sets is summarized in Algorithm 1.

3.2.2. Nonautonomous coherent structures

Unlike autonomous coherent structures, nonautonomous coherent sets are allowed to move in phase space under the evolution of S .

We define a *coherent pair* for a subset $M_1 \subset M$ and a small neighborhood M_2 of $S(M_1)$. For a global analysis, one chooses $M = M_1 = M_2$.

Algorithm 1: Extracting k almost-invariant sets.

Input: irreducible transition matrix \bar{P} on partition $\mathcal{B} = \{B_1, \dots, B_n\}$ of M

Output: k almost-invariant sets

- 1 Compute fixed left eigenvector \mathbf{p} of \bar{P} ;
 - 2 Form the time-reversed matrix \bar{P}^R with entries $\bar{P}_{ij}^R = \frac{p_j \bar{P}_{ji}}{p_i}$;
 - 3 Compute the reversible transition matrix $R = (\bar{P} + \bar{P}^R)/2$;
 - 4 Compute k right eigenvectors $\boldsymbol{\vartheta}_1, \boldsymbol{\vartheta}_2, \dots, \boldsymbol{\vartheta}_k$ corresponding to the k largest eigenvalues of R ;
 - 5 Perform a clustering as k -means or SEBA on the k eigenvectors into k clusters;
 - 6 Return the clustering result;
-

Definition 3.2.4. Let μ be a reference probability measure on M_1 at time t_0 , and ν the pushforward probability measure on M_2 under S . A (ρ_0, S) -coherent pair (cf. [89]) is defined as a pair of sets (A_1, A_2) , with $A_1 \in M_1$ and $A_2 \in M_2$, such that

$$\rho_\mu(A_1, A_2) = \frac{\mu(A_1 \cap S^{-1}(A_2))}{\mu(A_1)} = \rho_0.$$

and $\mu(A_1) = \nu(A_2)$. We refer to A_1 as the ρ_0 -coherent set at initial time and refer to A_2 as the ρ_0 -coherent set at final time.

Remark. Observe, that for an arbitrary set $A \subset M$ of positive measure, there is the trivially coherent pair $(A_{t_0}, S(A_{t_0}))$ with coherence ratio $\rho_0 = 1$. However, such a coherent pair is not of interest for us when $S(A_{t_0})$ is very filamented in space. In presence of diffusion, this set will mix fast with its neighborhood. Since the box-discretization introduces diffusion into the system, the numerical extraction of coherent pairs that is described in the following ignores such trivially coherent pairs.

Let $\mathcal{B} = \{B_1, \dots, B_n\}$ be a partition of M_1 and $\tilde{\mathcal{B}} = \{\tilde{B}_1, \dots, \tilde{B}_m\}$ be a partition of M_2 . Let \bar{P} be the corresponding transition matrix between M_1 and M_2 , defined by equation (3.3). Following [20], we now describe the numerical extraction of optimal coherent pairs from the transition matrix \bar{P} .

The reference probability measure μ on M_1 at time t_0 is discretely represented as a probability vector \mathbf{p} with $p_i = \mu(B_i)$, $i = 1, \dots, n$. The image probability vector on M_2 at time $t_0 + \tau$, representing the reference probability measure ν on M_2 , is then simply computed as $\mathbf{q} = \mathbf{p}\bar{P}$. We assume both $\mathbf{p} > 0$ and $\mathbf{q} > 0$ and form a normalized matrix L via

$$L_{ij} = \frac{p_i \bar{P}_{ij}}{q_j}.$$

This matrix has the property that $\mathbf{1}L = \mathbf{1}$.

Consider the inner products $\langle \mathbf{x}, \mathbf{y} \rangle_{\mathbf{p}} = \sum_{i=1}^n x_i p_i y_i$ and $\langle \mathbf{x}, \mathbf{y} \rangle_{\mathbf{q}} = \sum_{i=1}^m x_i q_i y_i$. Let L^* denote the dual of L satisfying $\langle \mathbf{x}L, \mathbf{y} \rangle_{\mathbf{q}} = \langle \mathbf{x}, \mathbf{y}L^* \rangle_{\mathbf{p}}$. Here, $L^* = \bar{P}^T$.

We want to find two coherent pairs (A_1, A_2) , (A_1^c, A_2^c) , where

$$A_1 = \bigcup_{i \in I_1} B_i, \quad A_1^c = \bigcup_{i \in J_1} B_i, \quad A_2 = \bigcup_{i \in I_2} \tilde{B}_i, \quad A_2^c = \bigcup_{i \in J_2} \tilde{B}_i,$$

$$I_1 \cup J_1 = \{1, \dots, n\}, I_1 \cap J_1 = \emptyset, I_2 \cup J_2 = \{1, \dots, m\}, I_2 \cap J_2 = \emptyset,$$

that maximize the coherence ratio under the constraint that $\mu(A_1)$, $\mu(A_1^c)$, $\nu(A_2)$ and $\nu(A_2^c)$ are similar.

Let the vector $\mathbf{x} \in \{-1, 1\}^n$ represent the boxes belonging to A_1 respective A_1^c , that is, $x_i = 1$ if $i \in I_1$ and $x_i = -1$ if $i \in J_1$. Analogously, let vector $\mathbf{y} \in \{-1, 1\}^m$ represent the boxes belonging to A_2 respective A_2^c , that is, $y_i = 1$ if $i \in I_2$ and $y_i = -1$ if $i \in J_2$. Observe that (cf. [20])

$$\begin{aligned} \langle L\mathbf{x}, \mathbf{y} \rangle_q &= \hat{\rho}_\mu(A_1, A_2)\mu(A_1) + \hat{\rho}_\mu(A_1^c, A_2^c)\mu(A_1^c) \\ &\quad - \hat{\rho}_\mu(A_1, A_2^c)\mu(A_1) - \hat{\rho}_\mu(A_1^c, A_2)\mu(A_1^c). \end{aligned}$$

Thus, we achieve a high coherence ratio for the two pairs when we maximize $\langle L\mathbf{x}, \mathbf{y} \rangle_q$. We consider now the maximization problem (cf. [20]):

$$\max_{\substack{\mathbf{x} \in \{-1, 1\}^n \\ \mathbf{y} \in \{-1, 1\}^m}} \{ \langle L\mathbf{x}, \mathbf{y} \rangle_q : |\langle \mathbf{x}, \mathbf{1} \rangle_p|, |\langle \mathbf{y}, \mathbf{1} \rangle_q| < \epsilon \}$$

for a small ϵ . This is again a difficult combinatorial problem. We formulate a relaxed problem (cf. [20]):

$$\max_{\substack{\mathbf{x} \in \mathbb{R}^n \\ \mathbf{y} \in \mathbb{R}^m}} \left\{ \frac{\langle L\mathbf{x}, \mathbf{y} \rangle_q}{\|\mathbf{x}\|_p \|\mathbf{y}\|_q} : |\langle \mathbf{x}, \mathbf{1} \rangle_p|, |\langle \mathbf{y}, \mathbf{1} \rangle_q| = 0 \right\},$$

where $\|\mathbf{x}\|_p = \langle \mathbf{x}, \mathbf{x} \rangle_p^{1/2}$ and $\|\mathbf{y}\|_q = \langle \mathbf{y}, \mathbf{y} \rangle_q^{1/2}$. The normalization term is needed since the vectors \mathbf{x} and \mathbf{y} can now take values from whole \mathbb{R} .

As shown in [20], the problem is solved by $\mathbf{x} = \boldsymbol{\psi}_2 \in \mathbb{R}^n$ and $\mathbf{y} = \boldsymbol{\varphi}_2 \in \mathbb{R}^m$, where $\boldsymbol{\psi}_2$ is the left eigenvectors of LL^* and $\boldsymbol{\varphi}_2$ is the left eigenvector of L^*L to the second largest eigenvalue $\lambda_2 < 1$. These two eigenvalue problems can be turned into the task of finding leading singular values and corresponding left and right singular vectors of a sparse matrix, which can be very efficiently computed by iterative schemes (e.g. `svds` in MATLAB). Therefore, we define the diagonal matrices Π_p and Π_q , where $(\Pi_p)_{ii} = p_i, i = 1, \dots, n$, and $(\Pi_q)_{ii} = q_i, i = 1, \dots, m$. We compute the left and right singular vectors $\tilde{\boldsymbol{\psi}}_2$ and $\tilde{\boldsymbol{\varphi}}_2$ to the second largest singular value $\lambda_2 < 1$ of $\Pi_p^{-\frac{1}{2}} \bar{P} \Pi_q^{-\frac{1}{2}}$, which is a sparse matrix. Then, $\boldsymbol{\psi}_2 = \tilde{\boldsymbol{\psi}}_2 \Pi_p^{-\frac{1}{2}}$ and $\boldsymbol{\varphi}_2 = \tilde{\boldsymbol{\varphi}}_2 \Pi_q^{-\frac{1}{2}}$. The signed vector entries of $\boldsymbol{\psi}_2$ and $\boldsymbol{\varphi}_2$ can be interpreted as relaxations of indicator functions of the sets A_1 and A_2 and their complements. Thus the vector $\boldsymbol{\psi}_2$ defines fuzzy coherent sets on M_1 , whereas $\boldsymbol{\varphi}_2$ represents their image on M_2 . Optimal partitions of M_1 into finite-time coherent pairs can be approximated via a line search in $\boldsymbol{\psi}_2$ and $\boldsymbol{\varphi}_2$, allowing A_1 and A_1^c to have different measures than $\frac{1}{2}$ but making sure that $\mu(A_1) \approx \nu(A_2)$ and $\mu(A_1^c) \approx \nu(A_2^c)$.

As already described for the almost-invariant sets in Section 3.2.1, one can obtain k coherent sets by clustering the leading k singular vectors corresponding to singular values close to 1. The numerical extraction of k coherent pairs is summarized in Algorithm 2.

Algorithm 2: Extracting k coherent pairs.

- Input:** transition matrix \bar{P} between partitions $\mathcal{B} = \{B_1, \dots, B_n\}$ and $\tilde{\mathcal{B}} = \{\tilde{B}_1, \dots, \tilde{B}_m\}$ of M_1 and M_2
- Output:** k coherent pairs
- 1 Compute \mathbf{p} with $p_i = \mu(B_i)$, $i = 1, \dots, k$;
 - 2 Compute $\mathbf{q} = \mathbf{p}P$;
 - 3 Define diagonal matrices $(\Pi_{\mathbf{p}})_{ii} = p_i, i = 1, \dots, n$ and $(\Pi_{\mathbf{q}})_{ii} = q_i, i = 1, \dots, m$;
 - 4 Compute left and right singular vectors $\tilde{\boldsymbol{\psi}}_1, \dots, \tilde{\boldsymbol{\psi}}_k$ and $\tilde{\boldsymbol{\varphi}}_1, \dots, \tilde{\boldsymbol{\varphi}}_k$ to the k largest singular values $\lambda_1, \lambda_2, \dots, \lambda_k$ of $\Pi_{\tilde{\mathbf{p}}}^{\frac{1}{2}} \bar{P} \Pi_{\tilde{\mathbf{q}}}^{-\frac{1}{2}}$;
 - 5 Set $\boldsymbol{\psi}_i := \tilde{\boldsymbol{\psi}}_i \Pi_{\tilde{\mathbf{p}}}^{-\frac{1}{2}}$ and $\boldsymbol{\varphi}_i := \tilde{\boldsymbol{\varphi}}_i \Pi_{\tilde{\mathbf{q}}}^{-\frac{1}{2}}, i = 1, \dots, k$;
 - 6 Perform a clustering as k -means or SEBA on $\boldsymbol{\psi}_1, \dots, \boldsymbol{\psi}_k$ into k clusters; and return the clustering result (coherent sets at initial time);
 - 7 Perform a clustering on $\boldsymbol{\varphi}_1, \dots, \boldsymbol{\varphi}_k$ into k clusters; and return the clustering result (coherent sets at final time);
-

3.2.3. Finite-time entropy.

Transfer operators can also be used to estimate finite-time expansive behavior along trajectories in autonomous and nonautonomous dynamical systems. In [23] a stretching measure has been derived using the evolution of \bar{P} . It is based on the concept of differential entropy $h(f) = - \int_{\Omega} f \log f \, d\ell$, where Ω is the support of the density f .

For a given initial condition \mathbf{x}_0 , let $f_{\epsilon, \mathbf{x}_0} := \frac{1}{\ell(B_{\epsilon}(\mathbf{x}_0))} \mathbb{1}_{B_{\epsilon}(\mathbf{x}_0)}$ denote a uniform density supported on $B_{\epsilon}(\mathbf{x}_0)$, a ball of radius ϵ about \mathbf{x}_0 . We define an ϵ -smoothing operator by

$$\mathcal{A}_{\epsilon} f(\mathbf{x}) := \frac{1}{\ell(B_{\epsilon}(\mathbf{x}))} \int_{B_{\epsilon}(\mathbf{x})} f \, d\ell.$$

The rate of increase in entropy experienced in the ϵ -neighborhood of \mathbf{x}_0 over the time span $[t_0, t_0 + \tau]$ of the ϵ -perturbed dynamics can now be described by (cf. [23])

$$FTE_{\epsilon}(\mathbf{x}_0, t_0; \tau) := \frac{1}{|\tau|} [h(\mathcal{A}_{\epsilon} \bar{P} f_{\epsilon, \mathbf{x}_0}) - h(f_{\epsilon, \mathbf{x}_0})]. \quad (3.7)$$

Several properties of FTE_{ϵ} and its deterministic limit $\lim_{\epsilon \rightarrow 0} FTE_{\epsilon}$ have been derived in [23]. In particular, FTE_{ϵ} measures nonlinear stretching directly from the entropy growth experienced by a small localized density evolved by the transfer operator.

An approximation of the FTE field can be obtained very efficiently within the set-oriented framework. Let S denote the map that transports a particle $\mathbf{x}(t_0)$ to its new position $\mathbf{x}(t_0 + \tau)$ and let $\bar{\mathcal{P}}$ be the transfer operator that describes the evolution of densities under S . Let $\{B_1, \dots, B_n\}$ be the box discretized phase space and let \bar{P} denote the corresponding finite-rank approximation of $\bar{\mathcal{P}}$. In the discrete context, densities (which are central to the FTE-construction in equation (3.7)) are now represented by discrete probability vectors \mathbf{p} and the entropy of \mathbf{p} is simply $H(\mathbf{p}) = -\sum_{i=1}^n p_i \log p_i$.

Let δ_i be a n -tuple with a 1 in the i -th position and 0 elsewhere. Under the assumption that all boxes in $\{B_1, \dots, B_n\}$ are of equal volume, the discrete FTE of a box B_i with respect to the map S is then given by (cf. [23])

$$FTE(B_i, t_0; \tau) = \frac{1}{|\tau|} H(\delta_i \bar{P}) = -\frac{1}{|\tau|} \sum_{j=1}^n \bar{P}_{ij} \log \bar{P}_{ij}. \quad (3.8)$$

Thus the FTE field (equation 3.7) can be very quickly approximated by using equation (3.9) when the transition matrix \bar{P} has been computed.

If the dynamics are described by a time-homogeneous transition matrix \bar{P} , that is, the underlying velocity field is autonomous or time-periodic with period τ , we use the following formula to compute the FTE field with respect to the map $S^k, k \in \mathbb{N}$ (cf. [23]):

$$FTE(B_i, k) = -\frac{1}{k} \sum_{j=1}^n (\bar{P}^k)_{ij} \log (\bar{P}^k)_{ij}. \quad (3.9)$$

In addition, the FTE field for the backward-time dynamics can be conveniently computed by using the backward time matrix of \bar{P} . When all boxes have the same measure, this backward time matrix is the transpose of \bar{P} with rows normalized. Furthermore, stretching rates for differing box volumes can be computed, see [23] for more details.

Remark. FTE can be compared with finite-time Lyapunov exponents (FTLE) in the deterministic limit. The FTLE field is defined as [11]

$$FTLE(\mathbf{x}, t_0; \tau) = \frac{1}{2|\tau|} \log (\lambda_{\max}[(DS(\mathbf{x}))^T DS(\mathbf{x})]),$$

where $DS(\mathbf{x})$ denotes the Jacobean matrix of S at \mathbf{x} and $\lambda_{\max}[\cdot]$ denotes the largest eigenvalue. Many of the geometric approaches for the identification of Lagrangian coherent structures (LCSs) are based on FTLE [12]. Ridges in the FTLE field indicate barriers of transport and hence boundaries of coherent regions. FTE computations showed similar results to finite-time Lyapunov exponent computations [23].

Chapter 4.

Set-oriented description of mixing

In this short chapter, we address the set-oriented modeling of mixing for two types of fluids, advected by the same velocity field.

The term mixing has a wide range of meanings. In general, mixing describes the intermingling of distinct fluid materials that were originally separated in space [93].

In ergodic theory, the term mixing is defined as an asymptotic concept (see equation (2.1)). A measure-preserving transformation $S : X \rightarrow X$ is called mixing if for any two measurable subsets M_1 and M_2 the proportion of particles starting in M_1 and ending in M_2 is given as the product of $\mu(M_1)$ and $\mu(M_2)$ after a long time. In this sense, for example an ergodic (irreducible and aperiodic) Markov chain is mixing.

However, in nature or technically-relevant systems as the global ocean flow or microfluidic flows, one is often interested in the degree of mixedness after a given time span (or how long it takes to obtain a certain degree of mixedness). In a mixing device the fluid will be in the mixing region only for a finite time span. Furthermore, for industrial processes, it might be of interest to consider the mixedness for two types of fluids, when particles of the first type starting in a given subset M_1 and particles of the second type in M_2 . An example for a closed system is a static mixer, where the two types should be well-mixed after a given time span. A mixing device with constant inflow and outflow is an example for a double open system.

Mixing processes in fluid systems are typically a combination of diffusive mixing and advective mixing. Diffusive mixing or molecular diffusion is based on the undirected motions of particles at the smallest scales. An initially inhomogeneous scalar field will eventually be homogenized by diffusion. Advective mixing or stirring is based on the directed motion of a conserved scalar field as it is advected by a known velocity vector field. Mixing alone by diffusion is a very slow process. To obtain much faster homogenization, advection can be used to create small-scale structures in the scalar fields, which are then quickly smoothed by diffusion.

In the following, we address the set-oriented modeling of mixing for two types of fluids and consider mixing measures that we can apply in our model set-up.

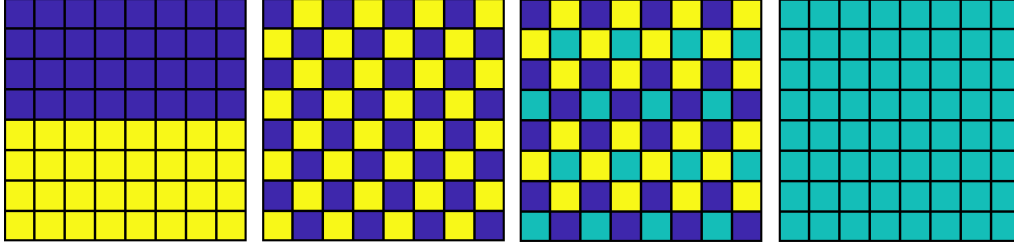


Figure 4.1.: Signed mass distributions on a discretized domain.

4.1. Modeling

We consider two types of fluid materials. These types have the same properties and are advected by the same velocity field and differ only in “color” – presented here as blue and yellow. So, in our discrete model, the transport of both mass distributions can be described by the same transition matrix \bar{P} on the box-discretized domain (see Section 3.1 for the closed setting resp. Section 6.1 for the open setting). Instead of following the mass distributions of the two fluids separately, we combine the two mass distributions to one signed mass distribution \mathbf{v} , where the sign distinguishes the two differently-colored fluid materials. A zero entry v_i would mean that in the respective box B_i the proportion of the two types is the same. We would consider a pattern to be perfectly mixed if the proportion of the two types in each box is equal to the proportion of the two types initialized into the system.

Mixing under transport by \bar{P} includes directly mixing by advection and indirectly mixing by diffusion. Diffusion happens not over the whole trajectories but only at the final positions of the trajectories after the discrete time step. The transition probabilities are calculated per box. Since particles are assumed to be uniformly spread in one box, diffusion increases with box diameter.

4.2. Quantification

We turn to the question, how to quantify the degree of mixedness of a signed scalar field $c(\cdot)$ (with zero mean), or the discretized mass distribution \mathbf{v} on a region X after a given time step (on a subset of the domain) or in case of limit distribution.

Figure 4.1 gives an illustration of signed mass distributions on a discretized domain. In the first panel, all fluid material of the first color is in the upper half, and all fluid material of the second color is in the lower half. So we would say it is poorly mixed. From left to right the mixing quality increases. We would consider the rightmost result to be perfectly mixed, because in each box there is the same proportion of both fluids.

Classical mixing measures are the intensity and scale of segregation by Dankwerts [41]. They are first- and second order statistics of the scalar field. In [94] three dimensions of mixing are proposed: the intensity and scale of segregation

and the exposure, which describes the potential to reduce segregation.

A classical measure of the intensity is the variance of the scalar field (or L^2 -norm for a zero-mean field). This leads to the first mixing measure in the discrete setting:

Definition 4.2.1. The sample variance is given by

$$s^2 = \frac{1}{n-1} \sum_{i=1}^n (v_i - \bar{v})^2,$$

where \bar{v} is the sample mean.

Remark. Note that in a purely advective setting, that is, without diffusion, the variance of the scalar field is unaffected by the dynamics. However, the transfer operator approach exhibits numerical diffusion such that the sample variance is a meaningful measure of advective mixing in our context.

For the first and second mass distributions in Figure 4.1 the sample variance is the same. But we would not say, that they are equally mixed. Or in other words, we need a second measure that takes the scales or the thickness of striations into account. That brings us to our next measure.

The semivariogram $\gamma(h)$ is a measure of spatial autocorrelation and provides information on the scales [43]. Let z_i be the indicator value in box B_i , $i = 1, \dots, n$, that is, 1 if $v_i > 0$ and 0 otherwise. We calculate the empirical indicator semivariogram by the estimator

$$\hat{\gamma}(h) = \frac{1}{2|N(h)|} \sum_{(B_i, B_j) \in N(h)} (z_i - z_j)^2,$$

where $(B_i, B_j) \in N(h)$, if the distance of the centers of B_i and B_j is $h \pm \delta$ for a bin width 2δ . The inverse of the initial slope of the variogram gives the mean length scale [95]:

Definition 4.2.2. The mean length scale is defined as

$$L = \frac{1}{2} \left[\frac{\partial \gamma}{\partial h} \right]_{h \rightarrow 0}^{-1}.$$

In our parameter studies, we estimate the mean length scale using the slope of the empirical indicator semivariogram $\hat{\gamma}$ and take into account spatial periodicity when appropriate.

The third measure we want to consider here is the mix-norm [42], a multiscale measure of mixing (equivalent to a negative Sobolev norm):

Definition 4.2.3. The mix-norm $\phi(c)$ of a scalar field $c(\cdot)$ on a 2-dimensional torus T^2 is defined as

$$\phi^2(c) = \int_0^1 \int_{T^2} \left(\frac{\int_{\mathbf{x} \in B(\mathbf{p}, s)} c(\mathbf{x}) \mu(d\mathbf{x})}{\mu(B(\mathbf{p}, s))} \right)^2 \mu(d\mathbf{p}) \mu(ds),$$

where $B(\mathbf{p}, s)$ is a 2-dimensional ball with center \mathbf{p} and radius $s/2$.

In the sense of the mix-norm a scalar field is considered to be well-mixed if its averages over arbitrary open sets are uniform. The variance by itself does not capture this property. In contrast to the L^2 -norm of a function, which is obtained by integrating the square of the function over the whole space, the mix-norm is obtained by integrating the square of average values of the function over a dense set of subsets contained in the whole space. It hence measures the mean variance of low-pass-filtered images of the scalar field.

For a scalar field $c(\cdot)$ with Fourier expansion $c(\mathbf{x}) = \sum_{\mathbf{k}} c_{\mathbf{k}} e^{i2\pi(\mathbf{k}\cdot\mathbf{x})}$, the mix-norm $\phi(c)$ is given by

$$\phi^2(c) = \sum_{\mathbf{k}} \frac{1}{(1 + (2\pi\|\mathbf{k}\|)^2)^{\frac{1}{2}}} |c_{\mathbf{k}}|^2.$$

Chapter 5.

Transport and mixing studies in closed systems

A closed system that is mixing according to the ergodic theoretical definition (see equation (2.1)) will lead to homogenization in the long run for two types of fluid materials. But these systems may show almost invariant and almost periodic behavior and contain regular sets that are characterized as phase space regions of positive Lebesgue measure that minimally mix with their surroundings (see Section 3.2).

In closed systems, these almost-invariant sets or coherent sets can be considered as organizers of mixing. They can act as "(leaky) ghost rods", where the surrounding fluid material is stretched and folded around them and thus may mix efficiently [67]. Respective eigenvalues of the transition matrix are strongly connected to the mixing rate, exchange rate or escape rate. This is however an asymptotic quantity and it does not have to say anything about the mixing quality after a finite time step. And of course, the resulting mixing patterns for two types of fluid materials on the whole domain would also depend on what proportions of the two types are initialized inside these regular sets.

Whereas there are many studies that consider the transport and mixing of a single scalar (for example a blob of dye) in chaotic and turbulent flows, there are less that consider the mixing of two scalars. Pratt, Meiss, and Crimaldi consider two initially distant reactive scalars (separated by a third nonreactive fluid) in example chaotic flows, where it comes to a reaction if the scalars come into contact. They observe that the reaction front is organized along the LCSs and the FTLE ridges serve to locate regions of enhanced reaction [96].

In this chapter, we present applications of transport and mixing in two closed example systems. As described in Section 3.2, eigenvectors with real eigenvalue close to one or respectively singular vectors with singular values close to one [15, 22] and FTE fields [23] extracted from the transition matrix identify the underlying structures that organize the mixing processes.

In Section 5.1, we consider a well-known double gyre system. In the first part of this section we analyze the robustness of coherent structures under deterministic constant perturbation. This will also serve as reference for Section 7.1, where we will open up this perturbed double gyre system. In the second part, we study the mixing patterns of two types of fluids that we initialized on the domain of the system and apply the mixing measures defined in Section 4.2.

In Section 5.2, we consider a turbulent 2-dimensional Rayleigh-Bénard convec-

tion flow (RBC). In the first part we demonstrate the applicability of the transfer operator method in this more complex flow and extract coherent sets for shorter and longer time spans. We compare the FTE fields extracted from the transition matrix with the FTLE fields, and the results of a k -means clustering with the results of the sparse eigenbasis approximation (SEBA). Additionally, we consider the robustness of the transfer operator method regarding the box-discretization. Most of this part was already published in [63]. In the brief second part, we initialize two types of fluids in the turbulent RBC system and study the mixing patterns.

5.1. Double gyre flow

The chaotic double gyre flow, introduced in [61], serves as testbed in many numerical studies, for example in [9, 22, 34, 96]. That the system is actually chaotic was formally proven in [97] by showing the existence of a horseshoe map. The extraction of almost-invariant sets and coherent sets in the double gyre system, can be found in [22].

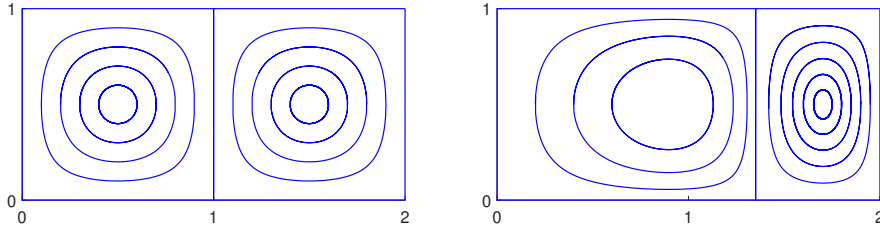


Figure 5.1.: Streamlines of the double gyre flow with $\alpha = 0.5$ and $\epsilon = 0.4$ at $t = 0$ (left) and $t = 0.25$ (right).

The periodically perturbed double gyre flow [61] has the stream function

$$\Psi_m = -\alpha \sin(f(x, t)\pi) \sin(\pi y),$$

where $f(x, t) = \epsilon \sin(\omega t)x^2 + (1 - 2\epsilon \sin(\omega t))x$ models the periodic perturbation with amplitude $\epsilon \geq 0$ and frequency ω , and $\alpha > 0$ controls the amplitude of the rotation speed of the gyres. We fix $\alpha = 0.5$ and set $\omega = 2\pi$, so that the period is $\tau = 1$. We consider the invariant domain $M = [0, 2] \times [0, 1]$.

For $\epsilon = 0$, the flow is time-independent and the phase portrait displays two counter-rotating gyres separated by a heteroclinic orbit connecting the hyperbolic fixed points at $(1, 0)$ and $(1, 1)$. For $\epsilon > 0$ the separatrix moves periodically. For $\epsilon \ll 1$, ϵ is approximately the maximum displacement of the separation line from the middle to the left or right, reached at times 0.25 and 0.75, respectively. For large ϵ , more than two gyres are formed at times 0.25 and 0.75.

Streamlines of the double gyre flow on M for two different time instances $t = 0$ and $t = 0.25$ are shown in Figure 5.1, with parameters $\alpha = 0.5$ and $\epsilon = 0.4$.

5.1.1. Coherent structures in the double gyre flow with windage

In this subsection, we use the double gyre flow to study the robustness of coherent structures (described in section 3.2) under deterministic perturbation. This sort of perturbation can be understood as wind that hits the ocean surface. Changes in shape, size, position of the coherent structures are conceivable. Under a high impact of wind a coherent structure could even disappear or a new coherent structure could form. The impact of wind-induced noise on LCSs was considered in [98].

We equip M with periodic boundaries, such that mass that would leave the domain at $x = 2$ enters again at $x = 0$, and introduce a deterministic perturbation, called *windage*, into our system. We consider wind with a constant velocity in a constant direction (from left to right), modeled by a constant velocity field

$$\Psi_b = \beta y, \quad \mathbf{u}_b = \begin{pmatrix} \beta \\ 0 \end{pmatrix}, \quad \text{with } \beta \geq 0.$$

We call β the wind factor.

The velocity field on M under impact of the wind has the form

$$\mathbf{u}(x, y, t) = \mathbf{u}_b(x, y) + \mathbf{u}_m(x, y, t),$$

where $\mathbf{u}_m(x, y, t)$ is derived from the stream function Ψ_m .

We divide the domain in 2^{16} boxes and initialize 100 test points in each box. For different system parameters $\epsilon = 0.1, 0.2, 0.3, 0.4$ combined with different wind factors $\beta = 0, 0.1, 0.3, 0.4, 0.5$, we integrate the test points in each box with the classical Runge-Kutta method RK4 for time-span $\tau = 1$ and compute the transition matrix P and the respective time-symmetrized matrix R .

We extract almost-invariant sets by using the leading eigenvectors of R . We heuristically expect to find two gyres and the background as three dominant almost-invariant sets in the system. The leading 10 eigenvalues of R for the different parameter choices are shown in Figure 5.3 (left). For almost all parameter choices there actually is a gap after the third eigenvalue (not always the largest). For $\epsilon = 0.3$ and $\beta = 0$ there is no gap after the third eigenvalue, but a gap arises with increasing β . Eigenvectors corresponding to the second and third eigenvalues of R are shown in Figure 5.3 and Figure 5.4. In order to compare the results for the different parameter choices, we apply a k -means clustering on the leading three eigenvectors of R even if it is not the optimal choice for $\epsilon = 0.3$ and $\beta = 0$. In Figure 5.5 we show the results of the clustering together with computed coherence ratios.

For $\epsilon = 0.1$ and $\epsilon = 0.2$ without windage, we obtain two almost-invariant sets (cyan and yellow clusters) that are connected and lumped. For $\epsilon = 0.1$, these clusters become smaller (by number of boxes) with increasing β with slightly smaller coherence ratio. The positions of the clusters slightly change, meaning there are boxes in the cluster that are not part of the clusters for $\beta = 0$. For $\epsilon = 0.2$, the cyan and yellow clusters become initially smaller (with slightly changing positions) and then the shape changes noticeably. The yellow and cyan

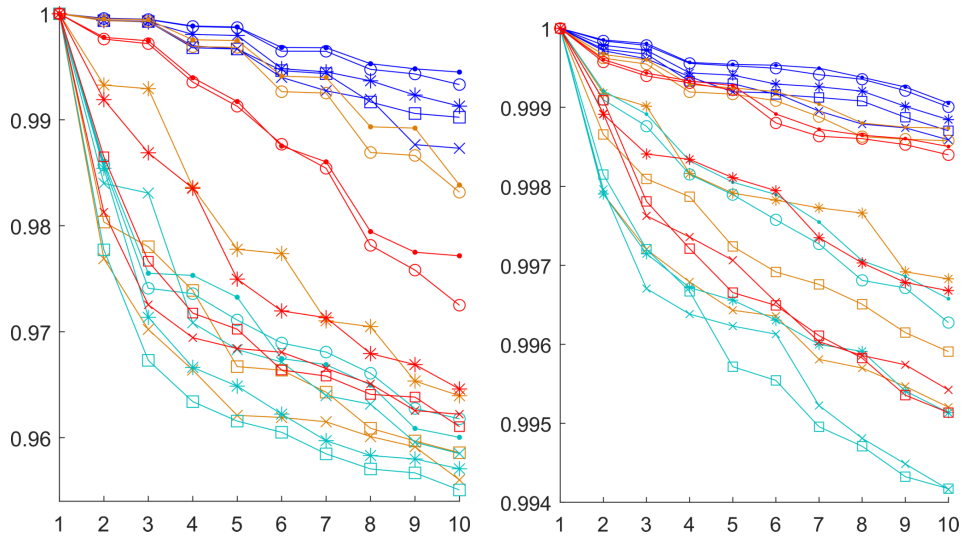


Figure 5.2.: Left: Leading 10 eigenvalues of R for time span $\tau = 1$. Right: Leading 10 singular values of L for time span $\tau = 4.5$. Blue: $\epsilon = 0.1$, orange: $\epsilon = 0.2$, cyan: $\epsilon = 0.3$, red: $\epsilon = 0.4$. Dots: $\beta = 0$, circles: $\beta = 0.1$, stars: $\beta = 0.3$, squares: $\beta = 0.4$ crosses: $\beta = 0.5$.

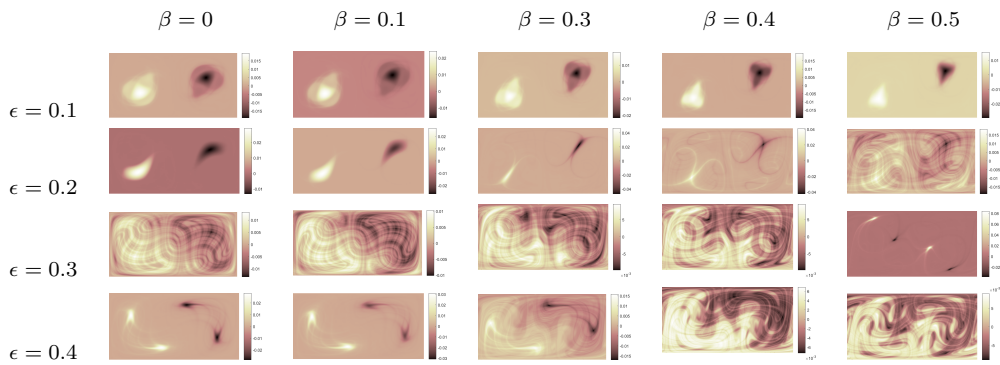


Figure 5.3.: Second eigenvectors of the time-symmetrized transition matrix R in the double gyre system with windage for time span $\tau = 1$ and different parameters of ϵ and β .

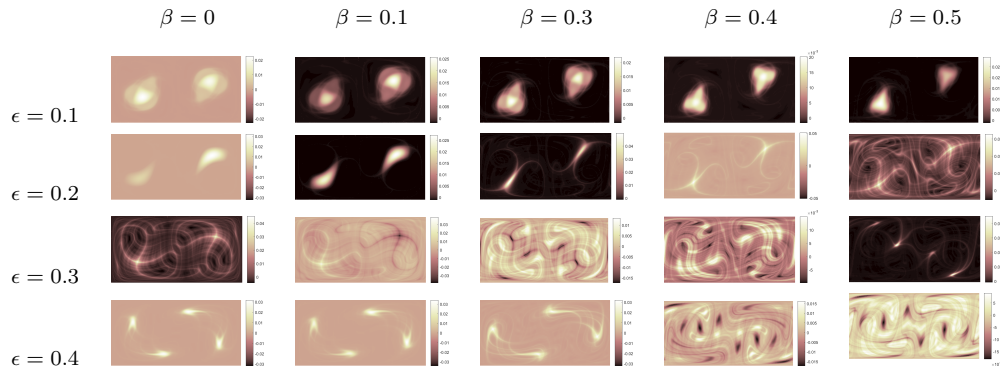


Figure 5.4.: Third eigenvectors of the time-symmetrized transition matrix R in the double gyre system with windage for time span $\tau = 1$ and different parameters of ϵ and β .

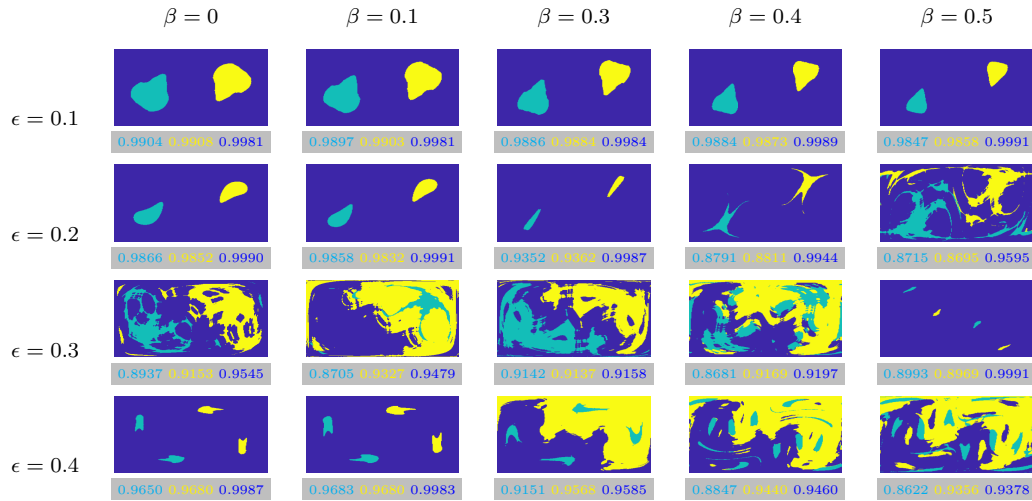


Figure 5.5.: Extraction of 3 clusters by using a k -means clustering on the leading eigenvectors of the time-symmetrized transition matrix R in the double gyre system with windage for time span $\tau = 1$ and different parameters of ϵ and β .

sets are stretched to the left and right over the whole domain and are in parts disconnected. (The eigenvectors of P does not show prominent lumped sets anymore, instead highlight curve-like structures.) For $\beta = 0.5$, the coherence ratios are relatively low.

For $\epsilon = 0.3$ and $\beta = 0$, there are no prominent lumped almost-invariant sets and the extracted clusters have relative low coherence ratios. For $\beta = 0.5$, the cyan and yellow clusters consist both of two relatively small lumped sets that are separated in space.

For $\epsilon = 0.4$ and $\beta = 0$, the cyan and yellow clusters consist both of two lumped sets that are separated in space. For $\beta = 0.3$, four smaller lumped sets form now one cluster and the background is separated instead further into two clusters. When β is increased further, the cyan cluster consists of more smaller lumped sets.

When we consider the behavior of the extracted almost-invariant sets for the system without windage ($\beta = 0$) in the systems with windage, the coherence ratios of these sets decrease much more. In Figure 5.6 (left), we show as an example the coherence ratios for the cyan colored set extracted in the system with $\beta = 0$ in the systems with windage. Except for $\epsilon = 0.3$, the extracted almost-invariant sets looks very similar for $\beta = 0.1$. However, the coherence ratios drop significantly. The most robust set is the cyan set for $\epsilon = 0.1$. The coherence ratio of this set drops from 0.9904 to 0.8653. The coherence ratio of cyan set for $\epsilon = 0.2$ drops from 0.9866 to 0.7116. And for the cyan set for $\epsilon = 0.4$ the coherence ratio drops from 0.965 to 0.4515. Under $\beta = 0.5$ the coherence ratio of the most robust set ($\epsilon = 0.1$) is 0.415.

For a longer time-span $\tau = 4.5$, we now want to extract coherent sets. We compute the transition matrix P and the respective matrix L for the system with parameters $\epsilon = 0.1, 0.2, 0.3, 0.4$ for different strength of windage $\beta = 0, 0.1, 0.3, 0.4, 0.5$. We extract coherent pairs by using a k -means clustering on the leading left and right singular vectors of L .

Figure 5.2 (right) shows the leading 10 singular values for the different system parameters, respective left and right singular vectors for the second and third singular values are shown in the Figures 5.7 - 5.10. Except for $\epsilon = 0.4$, there is a noticeable gap after the third singular value. For $\epsilon = 0.4$ and low wind factor a larger gap can be observed after the fifth singular value. For $\epsilon = 0.1$ the spectrum is relatively robust under the influence of β . That is also the case for the other choices of ϵ and a low wind factor $\beta = 0.1$. For $\epsilon = 0.2, 0.3, 0.4$ and higher wind factors, the spectrum underlies more changes (larger gaps can be found after the fourth, fifth and sixth singular values). In order to compare the change of the coherent sets, we extract three coherent pairs for all parameter choices.

In Figure 5.11 are the results of a k -means clustering on the leading three left singular vectors of L , presenting the coherent sets at initial time. Under each image the coherence ratios of the coherent pairs are given. Figure 5.12 shows the corresponding extracted coherent sets at final time. For $\epsilon = 0.1$, the cyan set becomes smaller with increasing wind factor. The yellow set becomes slightly bigger for $\beta = 0.1$ and then also becomes smaller with increasing β . A change in

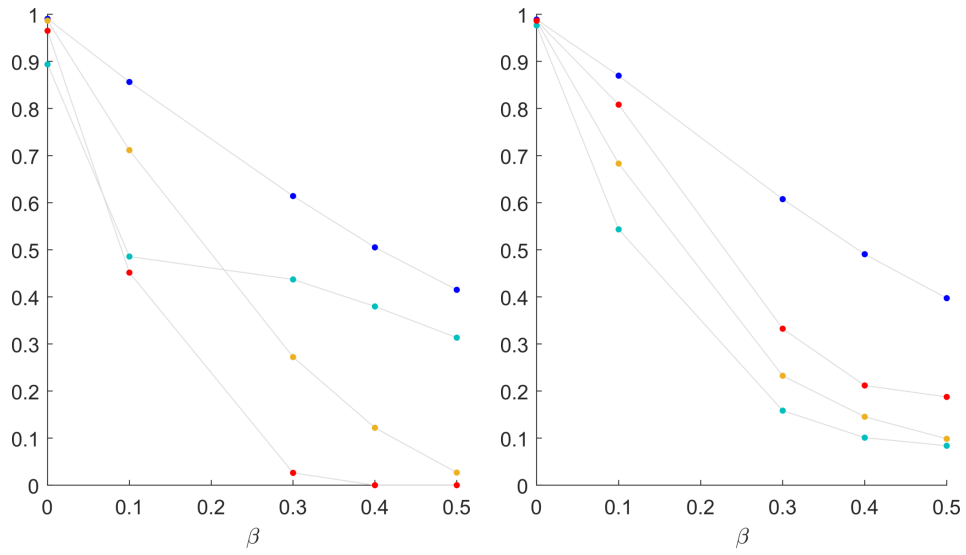


Figure 5.6.: Left: We consider the cyan colored almost-invariant set extracted for $\beta = 0$ and show the coherence ratios of this set in the systems with windage parameter $\beta = 0, 0.1, 0.3, 0.4$. Right: We consider the cyan colored coherent pair extracted for $\beta = 0$ and show the coherence ratio of this pair in the system with windage. Blue: $\epsilon = 0.1$, orange: $\epsilon = 0.2$, cyan: $\epsilon = 0.3$, red: $\epsilon = 0.4$.

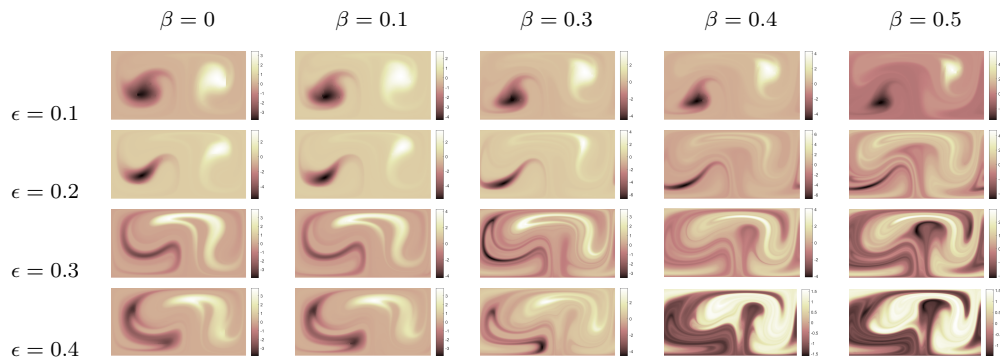


Figure 5.7.: Second left singular vectors of L in the double gyre system with windage for time span $\tau = 4.5$ and different parameters of ϵ and β .

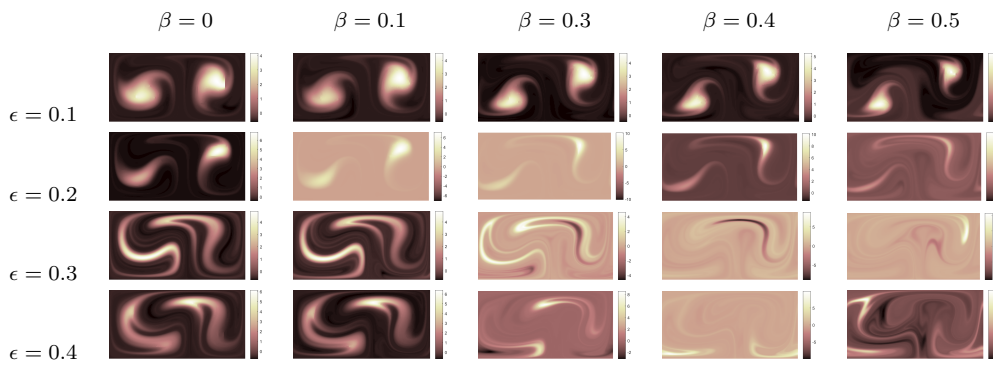


Figure 5.8.: Third left singular vectors of L in the double gyre system with windage for time span $\tau = 4.5$ and different parameters of ϵ and β .

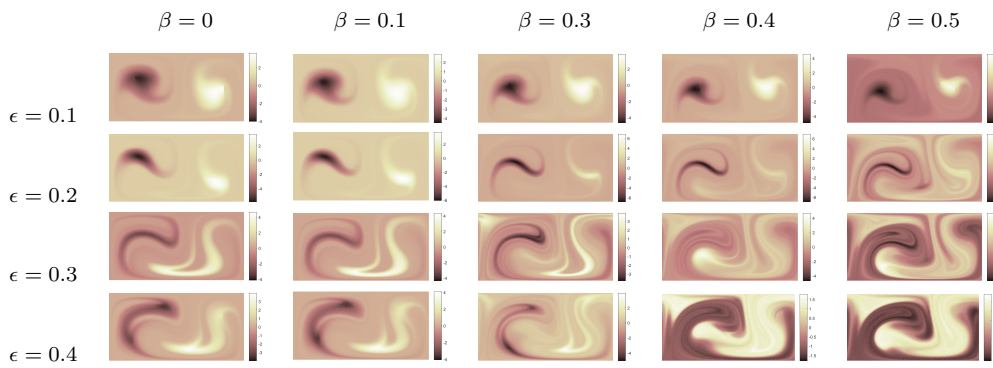


Figure 5.9.: Second right singular vectors of L in the double gyre system with windage for time span $\tau = 4.5$ and different parameters of ϵ and β .

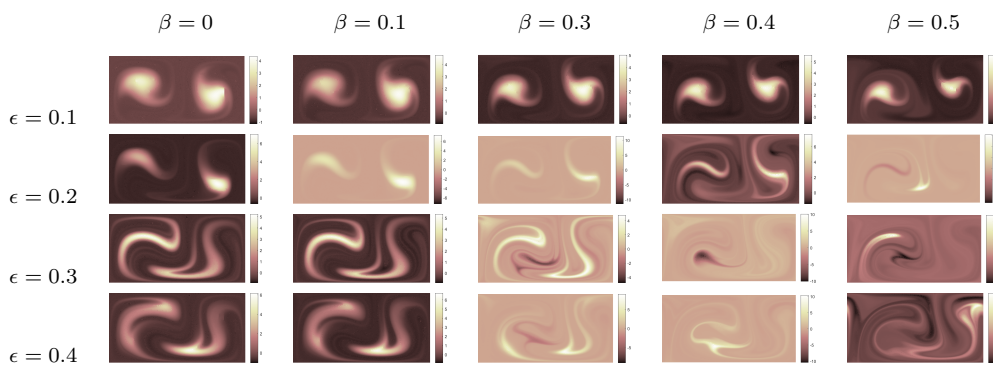


Figure 5.10.: Third right singular vectors of L in the double gyre system with windage for time span $\tau = 4.5$ and different parameters of ϵ and β .

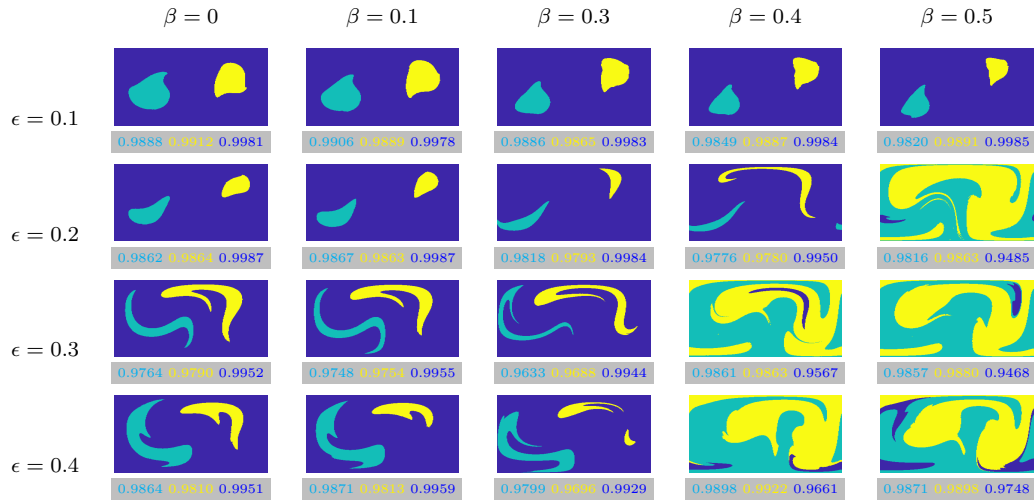


Figure 5.11.: Extraction of 3 clusters by using a k -means clustering on the leading left singular vectors of L in the double gyre system with windage for time span $\tau = 4.5$ and different parameters of ϵ and β .

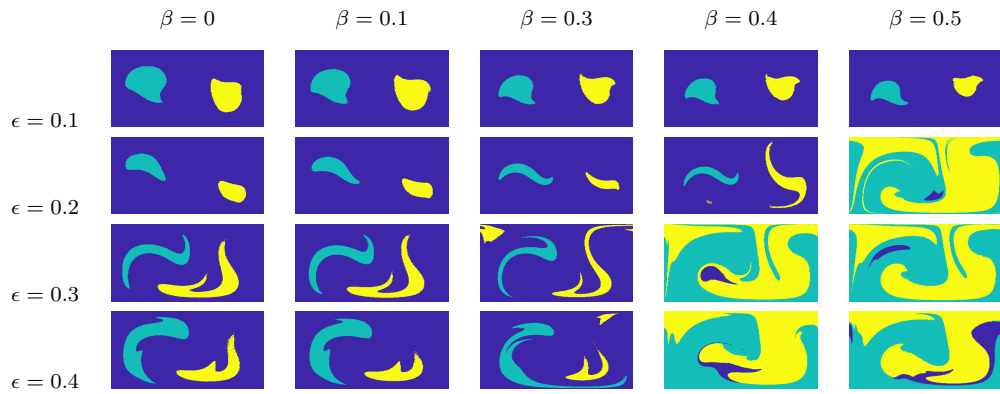


Figure 5.12.: Extraction of 3 clusters by using a k -means clustering on the leading right singular vectors of L in the double gyre system with windage for time span $\tau = 4.5$ and different parameters of ϵ and β .

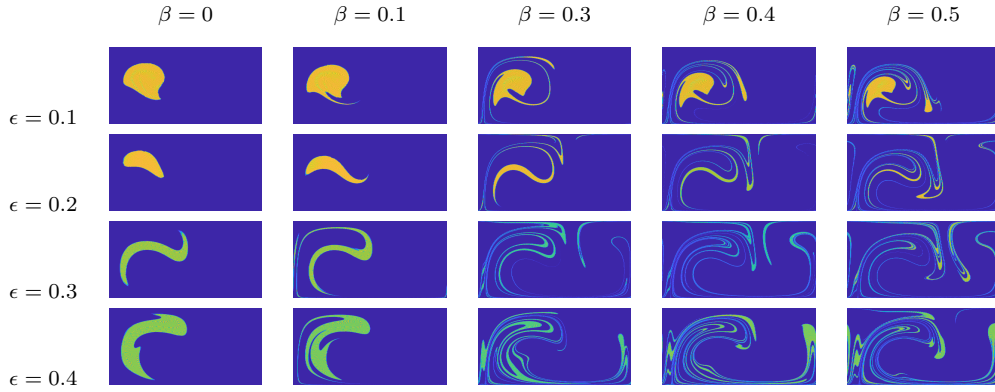


Figure 5.13.: Image of the indicator vector of the cyan colored coherent set extracted for $\beta = 0$ in the systems with windage parameter $\beta = 0, 0.1, 0.3, 0.4$.

the positions can be observed. For $\epsilon = 0.2$ the shape of the cyan and yellow set is stretched in space for wind factors $\beta = 0.3$ and $\beta = 0.4$. The size of the cyan sets becomes smaller and the size of the yellow set becomes larger for $\beta = 0.4$. For $\beta = 0.5$ the clustering result shows considerable differences. The phase space is then partitioned in two bigger clusters and one smaller cluster. For $\epsilon = 0.3$ and $\epsilon = 0.4$ this happens already for $\beta = 0.4$.

The extracted coherent pairs have all relatively high coherence ratios, that means, when we follow a mass that is supported on the coherence set at initial time over time span $\tau = 4.5$ it would resemble the extracted coherence set at final time. We now want to consider the behavior of the coherent sets extracted for the system without windage ($\beta = 0$) in the systems with windage. In Figure 5.13 we follow for each ϵ a mass that is supported on the extracted cyan coherent set for $\beta = 0$ under different wind factors (evolved by the computed transition matrices). Whereas for $\beta = 0.1$ it still shows a relatively coherent behavior, it gets more and more filamentous with increasing β and the coherence ratio of the original coherent pair sinks significantly. In Figure 5.6 (right) we show the coherence ratios for the cyan colored set extracted in the system with $\beta = 0$ in the systems with windage. The coherence ratio of the most robust coherent pair ($\epsilon = 0.1$) drops to 0.8697 under wind factor $\beta = 0.1$ and is 0.3972 under $\beta = 0.5$. The coherence ratio of the cyan set for $\epsilon = 0.2$ drops more drastically. Even under $\beta = 0.1$, where the extracted coherent set looks very similar, the coherence ratio is only 0.683.

To sum up, the existence of a regular almost-invariant set or coherent set appears not to be destroyed by smaller windage factors. However, when using estimated locations of these sets, even a smaller windage factor can lead to a significant loss of mass.

5.1.2. Mixing of two types of fluids

We consider now the double gyre flow (without windage, $\beta = 0$) and set parameter ϵ as 0.2, 0.3 and 0.4. We consider two different initial signed mass distributions v_0 . For the first, two types of fluids are placed horizontally and for the second vertically, and the fluid materials fill the whole domain. We set v_0 in that way that entries for boxes with fluid of the first color get the value 1 and entries for boxes with fluid of the second color -1. We compute the mass distributions v_k , $k = 1, \dots, 1000$. A selection of the computed mass distributions is presented in Figure 5.14.

The mixing patterns (as resulting from stretching and folding) are organized by the manifolds of the unstable fixed points and almost-invariant sets. In Figure 5.15 the $FTE(\cdot, 1)$ and $FTE(\cdot, 5)$ fields in backward time for $\epsilon = 0.2$ are shown. The ridges (high stretching factors) indicate neighborhoods of the local and global unstable manifolds of the hyperbolic trajectories. Depending on the initial distributions, the mixing patterns (Figure 5.14) are dictated by these ridges. After a few time steps we recognize the two almost-invariant sets as blue and yellow blobs for $\epsilon = 0.2$. Around 10 time steps the remaining part around these blobs is already very filamentous. Around 20 time steps the filaments can still be seen but the mass distribution becomes more and more homogeneous. The two blobs pale and becomes smaller but are still visible after 1000 time steps.

For $\epsilon = 0.3$, we observe a much faster homogenization, since there are no prominent almost-invariant sets with high coherence ratio. Already after 20 time steps the blue and yellow structures are very pale.

For $\epsilon = 0.4$, the two almost-invariant sets consist of two almost-cyclic sets that are separated in space. This behavior can be observed when using the horizontally placed initial distribution and the yellow and blue blobs change its position after each time step. The regular sets can still be observed after 500 time steps but the values inside are already close to the mean. After 1000 time steps the structures are not visible anymore.

Figure 5.16 shows the computed sample variance, relative mix-norm and mean length scale on the whole domain for the first 40 time steps. Initially, the relative mix-norm shows a much faster decay than the sample variance. Similar results for the L^2 -norm and relative mix-norm for the checkerboard flow in a non-transfer-operator-setting were obtained in [99]. The mean scale shows a fast decay for the beginning time steps but after ten time steps there can be observed no monotone decay anymore.

At initial time steps the differences between the vertically placed initial distributions are stronger than the differences between the horizontally placed initial distributions. The sample variance quantified the vertically placed for $\epsilon = 0.4$ as better mixed than the horizontally for a few time steps. In general, however, the horizontally placed initial distributions seems to have an advantage over the vertically placed initial distributions in this example system.

Both the sample variance and mix-norm quantify the mixing patterns for $\epsilon = 0.3$ as best mixed. Around 10 time steps, both the sample variance and the relative mix-norm quantify the mixing patterns for $\epsilon = 0.2$ as better mixed as

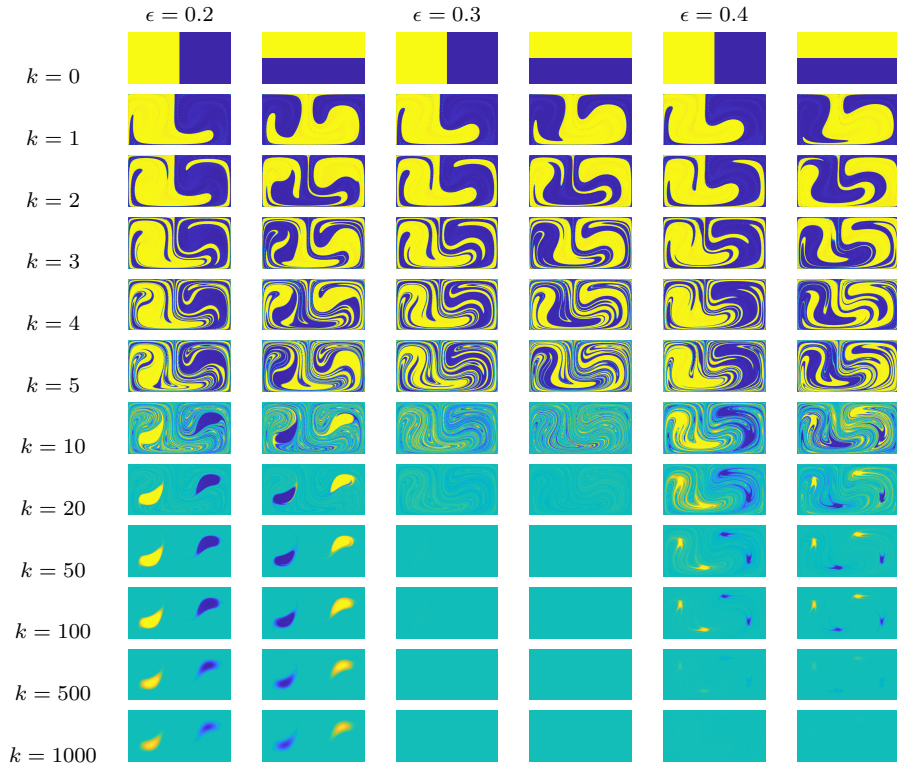


Figure 5.14.: Evolution of the mass distribution v_k (vertical and horizontal) for the closed double gyre mixer with parameters $\alpha = 0.5$ and different choices of ϵ .

for $\epsilon = 0.4$. At later time steps the patterns for $\epsilon = 0.2$ are worst mixed.

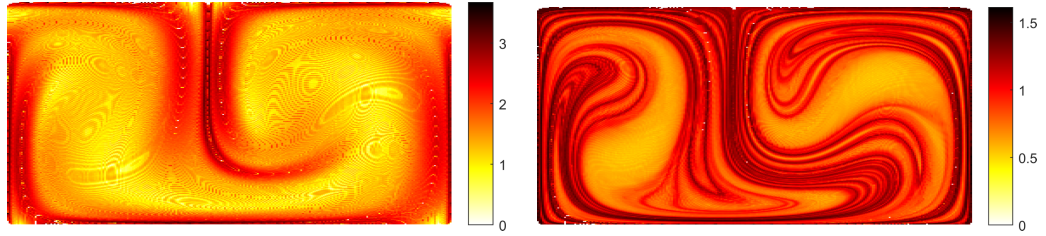


Figure 5.15.: $FTE(\cdot, 1)$ and $FTE(\cdot, 5)$ fields in backward time for $\epsilon = 0.2$

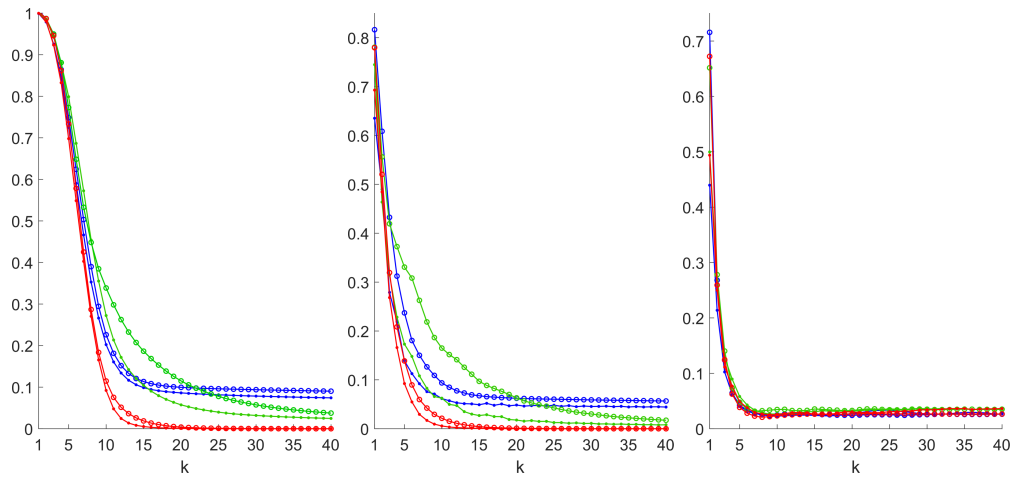


Figure 5.16.: Mixing measures applied to \mathbf{v}_k . Left: Sample variance. Middle: Relative mix-norm. Right: Mean length scale. Blue: $\epsilon = 0.2$, red: $\epsilon = 0.3$, green: $\epsilon = 0.4$. Circles: vertically placed initial distribution, dots: horizontally placed initial distribution.

5.2. Rayleigh-Bénard convection flow

This section aims to demonstrate the applicability of set-oriented framework to more complex systems as turbulent flows. Parts of the first subsection were already published in [63]. We study the coherent behavior in turbulent Rayleigh-Bénard convection (RBC). RBC can be seen as idealized model of natural thermal convection flows. In the set-up, a fluid layer is placed between two parallel solid horizontal plates with temperature difference $\Delta T = T_{\text{bottom}} - T_{\text{top}}$. The lower plate is held at a constant hot temperature T_{bottom} and the upper plate is held at a constant cool temperature T_{top} [100].

We consider the dynamics of the RBC in a two-dimensional closed box of small aspect ratio $\Gamma = L_x/H = 4$ (length/height) with Prandtl number $\text{Pr} = 10$ close to convection in water and Rayleigh number 10^6 . We consider the same two-dimensional RBC system as in [62]. The data set (obtained by a direct numerical simulation) consists of velocity and temperature fields at 512×128 grid points at times $t = 2000 t_f, 2000.1 t_f, 2000.2 t_f, \dots, 2500 t_f$, with $t_f = H/u_f$ being the free-fall time, which is taken as the convective time unit. Time averaged velocity and temperature fields exhibits a pair of counter-rotating circulation rolls, where hot fluid rises in the central region and cold fluid falls near the sidewalls. Figure 5.17 (slightly changed from [62]) shows the velocity field at an instantaneous time. The following remark provides further explanations on the RBC system.

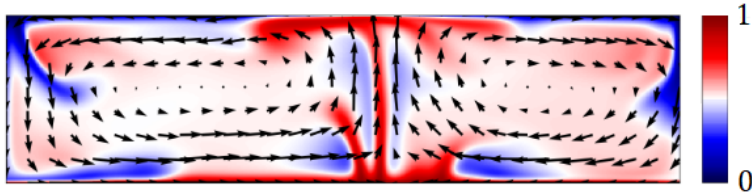


Figure 5.17.: Instantaneous velocity field of the RBC system, changed from [62]. Hot temperatures are colored in red and cool temperature are colored in blue.

Remark. Two dimensionless numbers, that govern the RBC system, are the Prandtl number (Pr) and the Rayleigh number (Ra). The Prandtl number characterizes molecular dissipation properties and is defined as $\text{Pr} = \frac{\nu}{\kappa}$, where ν is the kinematic viscosity and κ is the thermal diffusivity of the fluid. (The Prandtl number is extremely small in stellar or solar convection with $\text{Pr} \lesssim 10^{-6}$; it is $\text{Pr} \approx 0.7$ for atmospheric turbulence, and $\text{Pr} \approx 7$ for convective motion in the oceans.) The Rayleigh number measures the vigor of convective turbulence and is defined as $\text{Ra} = \frac{\alpha g \Delta T H^3}{\nu \kappa}$, where α is the isobaric expansion coefficient and the acceleration due to gravity g (pointed in $-z$ direction).

The nondimensionalized RBC equations, given in the Boussinesq approxima-

tion [100], are

$$\frac{\partial \mathbf{u}}{\partial t} + \mathbf{u} \cdot \nabla \mathbf{u} = -\nabla p + T \mathbf{e}_z + \sqrt{\frac{\text{Pr}}{\text{Ra}}} \nabla^2 \mathbf{u}, \quad (5.1)$$

$$\frac{\partial \theta}{\partial t} + \mathbf{u} \cdot \nabla \theta = u_z + \frac{1}{\sqrt{\text{Pr Ra}}} \nabla^2 \theta, \quad (5.2)$$

$$\nabla \cdot \mathbf{u} = 0, \quad (5.3)$$

where $\mathbf{u} = (u_x, u_z)$ is the velocity field, θ is the temperature fluctuation field and p is the pressure fluctuation field. The temperature fluctuations θ are deviations from the linear conductive (equilibrium) profile and related to the total temperature field S via

$$T(x, z, t) = T_{\text{bottom}} - \frac{\Delta T}{H} z + \theta(x, z, t).$$

Equations (5.1–5.3) are nondimensionalized using the height H (distance between the two plates) as the length scale, the free-fall velocity $u_f = \sqrt{\alpha g \Delta T H}$ as the velocity scale, and the temperature difference ΔT as the temperature scale. Equations (5.1–5.3) are solved for $\text{Pr} = 10$ and $\text{Ra} = 10^6$ in a two-dimensional box of aspect ratio $\Gamma = L_x/H = 4$ subject to appropriate boundary conditions. Stress-free boundary conditions for the velocity field are applied at all walls and the side walls have Neumann boundary conditions, $\partial T/\partial n = 0$. The computational details can be found in [62].

5.2.1. Extraction of organizing structures

We now use the computed velocity field \mathbf{u} of the data set to set up the transition matrix P . Therefore, we partition the domain $X = [0, 4] \times [0, 1]$ in square boxes. We consider a coarse box discretization with 2^{12} boxes and a finer box discretization with 2^{16} boxes to study the robustness of the transfer operator method regarding the number of boxes. In addition to the results in [63], we consider here also an increased number of test points for the finer box discretization to study further the influence of number of test points. We initialize 16 test points in each box on a uniform grid for both box discretizations and initialize now also 100 test points for the finer box discretization. We integrate the test points by the RK4 method (using spatial interpolation of the velocities by cubic splines) from initial time $2000 t_f$ over time span τ . As in [62] we consider the two different cases: $\tau = 20 t_f$, which is the average turnover time for a tracer for this setting, and a longer time span $\tau = 200 t_f$.

In the following, we will first compare the finite-time entropy (FTE) extracted from the transition matrix (as described in section 3.2.3) with finite time Lyapunov exponents (FTLE), and the results of a k -means clustering with the results of the sparse eigenbasis approximation (SEBA) using the finer box discretization and 100 test points per box. Afterwards, we consider the influence of the box discretization and number of test points.

Figure 5.18 shows the computed forward time FTE fields (for the fine box discretization and 100 test points per box) and FTLE fields. The FTE field for

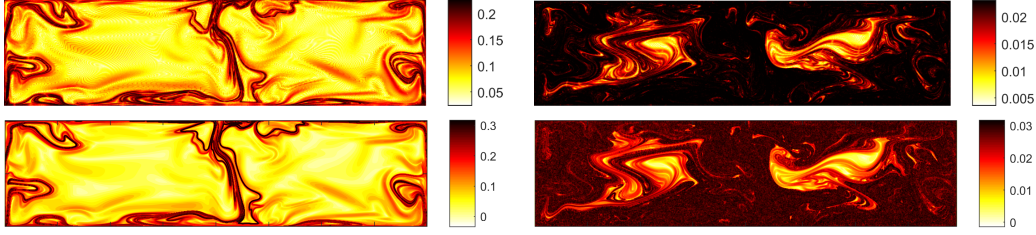


Figure 5.18.: Forward time FTE field for 2^{16} boxes (top left) and FTLE field (bottom left) computed over the short time interval $[2000, 2020]$. Forward time FTE field for 2^{16} boxes and 100 test points per box (top right) and FTLE field (bottom right) computed over the long time interval $[2000, 2200]$. Dark regions are characterized by large stretching and correspond to dominant transport barriers.

the short time span $\tau = 20 t_f$ visualizes the major transport barrier separating the two convection roles. The FTE field has large values in the box center where hot fluid rises and also at the boundaries, where cold fluid falls, and thus where the main heat transport takes place. The FTE field for the long time span $\tau = 200 t_f$ highlights extended regions of strong stretching, which fill the space apart from the gyre cores, which appear to have decreased in size considerably and have developed into more filamentary shapes. The FTE fields are very similar with the computed FTLE fields.

For the extraction of coherent sets, we compute the leading left and right singular vectors of the modified transition matrix L . Figure 5.20 shows the singular vectors for the short time span $\tau = 20 t_f$. The second singular vectors identify the left-right division induced by the major transport barrier and highlight the two different gyres. The third singular vectors distinguish the two gyre cores from the background flow. Further singular vectors as the fourth subdivide the gyre cores into smaller structures. This has also been observed in [62].

There is a spectral gap after the second singular value (Figure 5.19). However, in order to extract the apparently three dominant coherent pairs (two gyres and background) from the leading singular vectors, we apply a standard k -means algorithm to the three leading singular vectors. Figure 5.21 shows the clustering result using the three leading left singular vectors (presenting the coherent sets at initial time) and the three leading right singular vectors (presenting the coherent sets at final time). The two gyre cores are separated from the background flow, where most of the heat transport takes place.

As an alternative to the hard-clustering resulting from k -means for the initial time, we use SEBA [92] to find a sparse basis representation of the space spanned by the leading three left singular vectors. The results are shown in Figure 5.22. Two of the resulting sparse vectors are supported on each the gyre cores, and one sparse vector is supported on the background flow region. A superposition of the three vectors reveals in black a particularly incoherent (well mixing) region

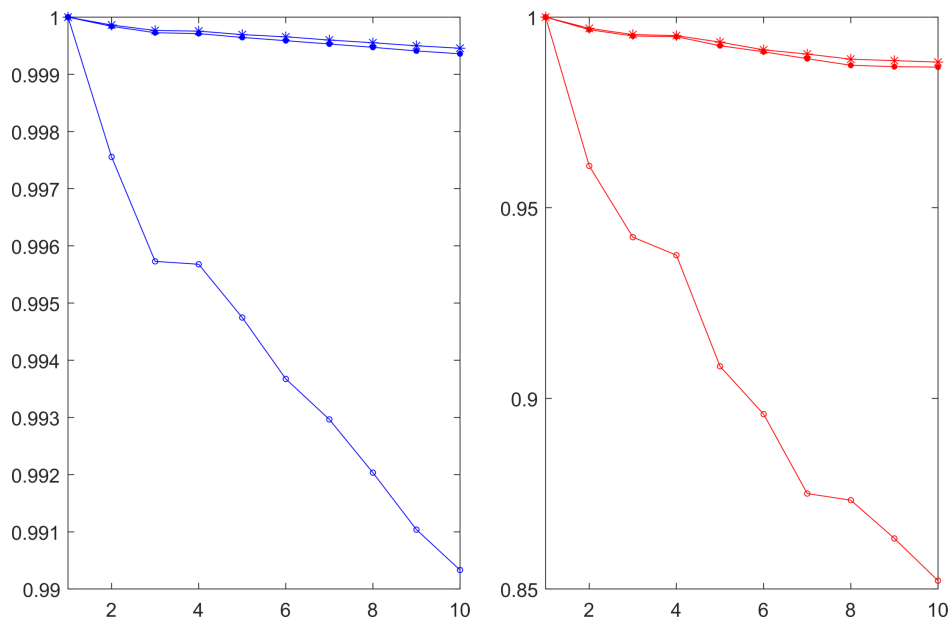


Figure 5.19.: Leading 12 singular values of the modified transition matrix calculated over the short time interval (left) and long time interval (right) for 2^{16} boxes and 100 test points per box (stars), 2^{16} boxes and 16 test points per box (filled dots) and 2^{12} boxes and 16 test points per box (circles).

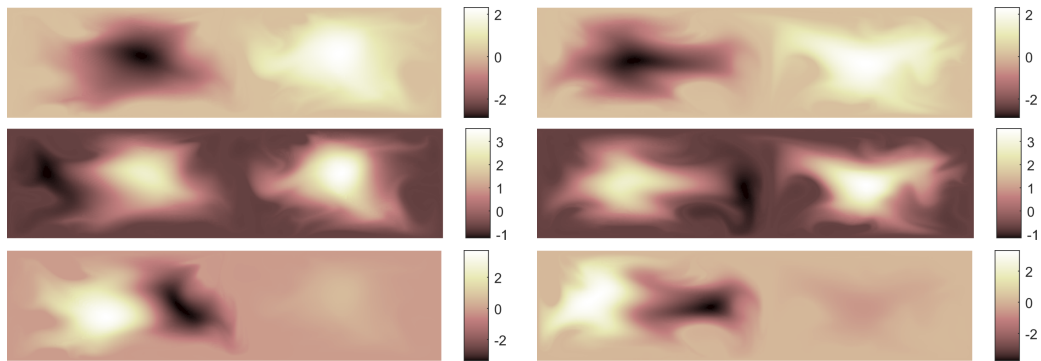


Figure 5.20.: Left singular vectors ψ_2, ψ_3, ψ_4 of the modified transition matrix L and corresponding right singular vectors $\varphi_2, \varphi_3, \varphi_4$ (right column). Here the short time interval $[2000, 2020]$, 2^{16} boxes and 100 test points per box are used for setting up the transition matrix.



Figure 5.21.: Extracted coherent sets at initial time (left) and final time (right) for the short time interval $[2000, 2020]$ via an application of the standard k -means algorithm on the first three left singular vectors respective first three right singular vectors. Here 2^{16} boxes and 100 test points per box are used.

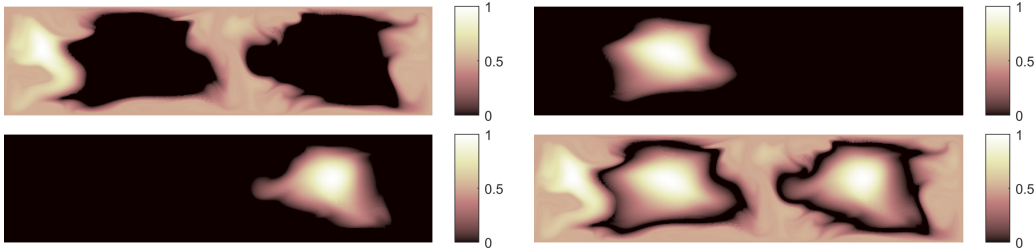


Figure 5.22.: SEBA applied to the first three left singular vectors, 2^{16} boxes and 100 test points per box, time interval $[2000, 2020]$. The upper row shows two of the output sparse vectors. Lower left shows the third output sparse vector and lower right shows the superposition of the three sparse vectors, revealing an incoherent region in black.

separating the two gyres from the background flow. We note that the results are comparable to those in [62].

Figure 5.23 shows leading singular vectors for the long time span $\tau = 200t_f$. As in the FTE and FTLE fields, we observe a shrinking and filamentation of the gyre cores in the leading left and right singular vectors. While the second singular vectors (top row) are analogous to those of the short time study, the third singular vectors (second row) appear to further subdivide the right gyre. This has also been observed in previous studies [62].

As there is a spectral gap after the fourth singular value (Figure 5.19), we use the corresponding four leading left singular vectors for postprocessing. Applying k -means (Figure 5.24) and SEBA (Figure 5.25, bottom) results in the identification of three very small gyre cores and the background flow. The SEBA result highlights here further a more coherent part of the background flow and shows again a particularly incoherent region that separates the gyres cores from the background flow.

The results for using less test points and for the coarse box coverings, are shown in Figures C.1- C.8 in appendix C. The computed singular vectors for the two different test point numbers and box coverings are very similar and highlight the same structures, indicating that the computational results are very robust.

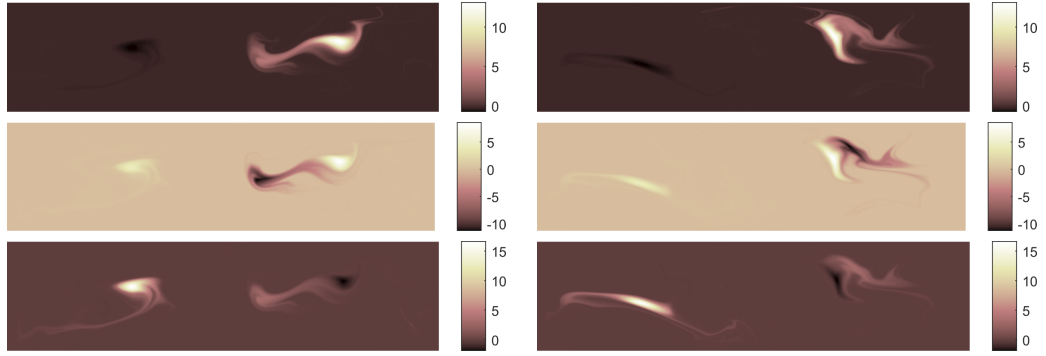


Figure 5.23.: Left singular vectors ψ_2, ψ_3, ψ_4 of the modified transition matrix L and corresponding right singular vectors $\varphi_2, \varphi_3, \varphi_4$ (right column). Here the long time interval $[2000, 2200]$ and 2^{16} boxes and 100 test points per box are used for setting up the transition matrix.



Figure 5.24.: Extracted coherent sets at initial time (left) and final time (right) for the long time interval $[2000, 2200]$ via an application of the standard k -means algorithm on the first three left singular vectors respective first three right singular vectors. Here 2^{16} boxes and 100 test points per box are used.

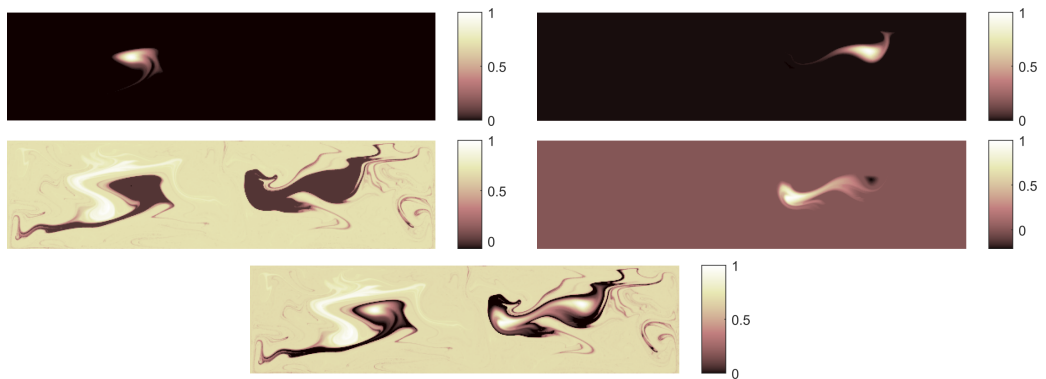


Figure 5.25.: SEBA applied to the first four left singular vectors, 2^{16} boxes and 100 test points per box, time interval $[2000, 2200]$. The first and second row show the four output sparse vectors. The third row the superposition of the four sparse vectors.

The computed FTE fields are in agreement with the FTE field for the finer box discretization and 100 test points per box. However, in particular for the long time interval, using 100 test points provides a more detailed smoother result.

Comparing the k -means results of both finer box discretizations with different number of test points, we observe that the results are very similar but the shape of the coherent sets is slightly different. (The coherence ratio is slightly improved using 100 test points.) The extracted coherent pairs for the coarse box covering highlights the same coherent sets. Comparing the SEBA results for the short time interval of both finer box discretizations with different number of test points, we observe again that the extracted coherent sets look very similar but have a slightly different shape. For the long time interval the SEBA results show more considerable differences. When one uses 16 test points, only the three gyre cores are highlighted. Using 100 test point provides a more detailed result of the background flow.

We studied the robustness of the coherent sets computations via k -means for another example system, the Bickley jet flow, in a conference paper [101], where we varied both the number of boxes and number of test points that are initialized in each box. We obtained reliable results even when both the number of boxes and the number of test points were reduced significantly. When the number of test points or boxes is decreased, the singular values decrease. The number of boxes had a larger impact on the spectrum than the number of test points. However, existing gaps in the leading singular vectors appears to be very robust, which we can also observe in Figure 5.19. When changing the number of boxes, the distances between the leading singular values appear to be scaled by a constant.

These studies of coherent behavior in a Rayleigh-Bénard convection flow can be extended to the three-dimensional case, which we did in [63].

5.2.2. Mixing of two types of fluids

We now consider two different initial distributions v_0 on the domain of the RBC flow, where two types of fluids are placed horizontally and vertically. We set v_0 in that way that entries for boxes with fluid of the first color get the value 1 and entries for boxes with fluid of the second color get the value -1 . As in the previous subsection, we use the computed transition matrices for the short ($\tau = 20 t_f$) and long ($\tau = 200 t_f$) time interval. Figure 5.26 shows the evolution of two mass distributions by the respective transition matrix using the finer box discretization and 100 test points per box. In Figure 5.27 the respective FTE fields in backward time are shown, whose ridges coincide with separating lines in the mixing patterns.

After the short time span, the vertically placed two types of colors reveal the major transport barrier between the two gyres. For the horizontally placed colors, we observe that the blue fluid from the bottom has risen to the top and the yellow fluid has been transported from the top to the bottom.

As expected, there is less transport and mixing from left to right: After the long time interval, the vertically initialized colors lead to two larger blobs of blue and yellow. The horizontally placed colors show a better mixing result after this

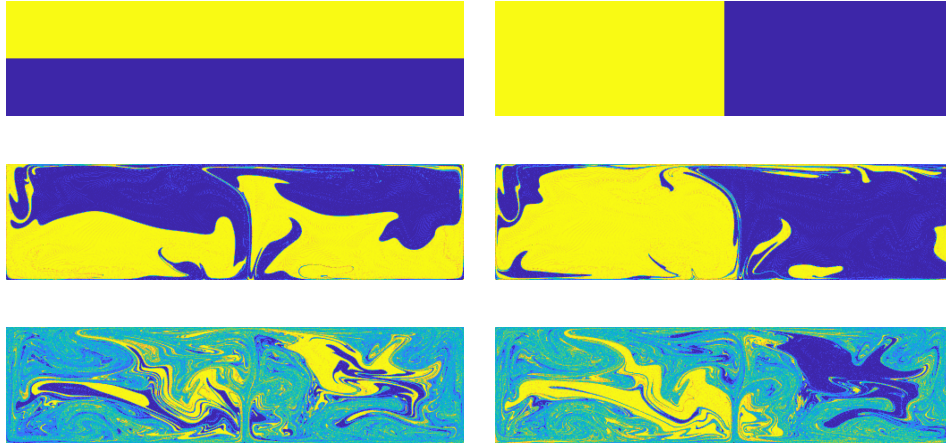


Figure 5.26.: Evolution of two signed mass distributions in the RBC system.

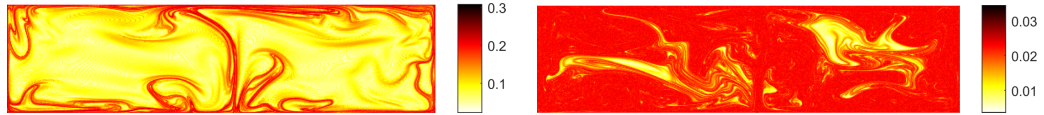


Figure 5.27.: FTE fields in backward time computed for the short time interval $[2000, 2020]$ and long time interval $[2000, 2200]$.

time span by sight. Here we observe more filaments of the other color in the less mixed region. This is with in agreement with the mixing measures sample variance, mix-norm and mean length scale (see Table C.1 in the appendix C).

Resulting mixing patterns for the finer box discretization and less test points and the coarser box discretization are shown in Figure C.9 in the appendix C. When using only 16 test points per box, the mixing patterns show a less smooth coloring. After the short time interval the sample variance is even higher than 1, since due to numerical inaccuracies many entries of the mass distributions have absolute values higher 1. The mix-norm appears here to be the most robust mixing measure when changing the number of test points and boxes. This is in agreement with the results in [68], where we have studied the influence of the discretization more systematically in a parameter study in an open system.

Chapter 6.

Set-oriented description of transport in open systems

In this chapter, we consider the transport and mixing in open flows. In particular, we consider the dynamics of a flow map $S : X \rightarrow X$ that is defined on an infinite strip $X \subset \mathbb{R}^2$, where X can be divided into three regions: a background flow transports particles from an unbounded unmixed region X_1 into an unbounded mixed region X_3 after passing a bounded mixing region X_2 (Figure 6.1).

In Section 6.1, we give a formal set-oriented description of the transport in these types of open systems. In Section 6.2, we formally consider the transport in an double-open system, where additionally new mass constantly flows into the system. In Section 6.3, we describe the organizing structures that can be detected in these open systems.

Parts of this chapter were already published in [68].

6.1. Conditional transfer operator

Consider an infinite strip $X \subset \mathbb{R}^2$. We assume that the underlying velocity field on X divides the domain into three regions: an unbounded unmixed region X_1 , a bounded mixing region X_2 and unbounded mixed region X_3 . A background flow transports particles from X_1 into the mixing region X_2 and from X_2 finally into X_3 . (Figure 6.1).

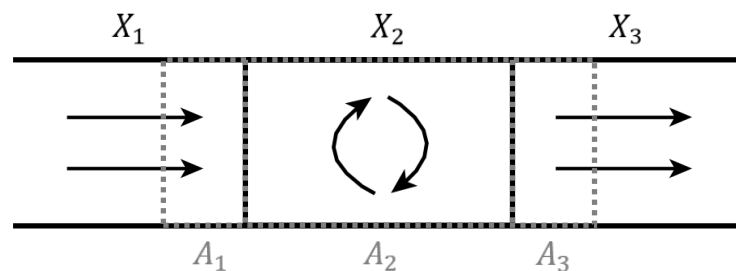


Figure 6.1.: Schematic representation of the dynamics on an infinite strip X that is divided into an unmixed region X_1 , a mixing region X_2 and an mixed region X_3 .

Let flow map $S : X \rightarrow X$ describe the transport of a single particle on X from time t_0 to $t_0 + \tau$.

We want to describe the mass evolution on an open subsystem with domain A , where A contains an inlet flow region $A_1 \subset X_1$ and an outlet flow region $A_3 \subset X_3$ as well as the mixing region $A_2 = X_2$. We define our compact, connected domain $A = \overline{A_1 \cup A_2 \cup A_3}$ in the following way. Particles in the unmixed region $A_1 \subset X_1$ enter the mixing region A_2 in one time step τ . In most examples, we then choose the set $A_3 \subset X_3$ to be of the same size as A_1 such that the particles in A_3 leave the domain of the open system in one time step.

Let $S_A : A \rightarrow X$ be the restriction of S on $A \subset X$ and let ℓ_A be normalized Lebesgue measure on A , that is, $\ell_A(B) = \frac{\ell(B)}{\ell(A)}$ for all $B \in \mathcal{B}(A)$. We can formally write $S_A : (A, \mathcal{B}(A), \ell_A) \rightarrow (X, \mathcal{B}(X), \ell_A)$. By construction A is not invariant under the action of the flow map, that is, $S_A(A) \not\subset A$ and $S_A^{-1}(A) \not\subset A$, as some mass leaves A under iteration of S_A and S_A^{-1} .

Analogously to the closed case, we can define a conditional transfer operator (cf. [35, 36, 81]):

$$\mathcal{P} : L^1(A) \rightarrow L^1(A),$$

via

$$\int_B \mathcal{P} f d\ell_A = \int_{S^{-1}B} f d\ell_A \quad \text{for all } B \in \mathcal{B}(A).$$

Due to the leakage out of A , we have $\|\mathcal{P}\mathbb{1}_A\| < 1$.

The numerical approximation of \mathcal{P} in terms of a transition matrix P can be derived in a similar manner as in the closed case. Let now the set A be partitioned into n sets B_i , $i = 1, \dots, n$, where $B_i \cap B_j = \emptyset$ for all $i \neq j$ and form the matrix

$$P_{ij} = \frac{\ell_A(B_i \cap S_A^{-1}(B_j))}{\ell_A(B_i)} = \frac{\ell_A(B_i \cap S^{-1}(B_j))}{\ell_A(B_i)} = \frac{\ell(B_i \cap S^{-1}(B_j))}{\ell(B_i)}. \quad (6.1)$$

The evolution of a (signed) density can be again represented by the discrete push-forward of a vector $\mathbf{v}_0 \in \mathbb{R}^n$ via $\mathbf{v}_1 = \mathbf{v}_0 P$.

Unlike in the closed case, P is no longer row-stochastic but row-substochastic as there is constant outflow of mass.

We can extend P to a stochastic matrix \bar{P} on state space $B = \{B_i, i = 1, \dots, n, n+1, \dots, N\}$ by adding $N - n$ absorbing states that model states that are not in the domain A in X_3 . Since we are not really interested in states outside of the domain A , we model them as finite absorbing states.

Under the assumption that all particles can (eventually) leave A and reach an absorbing state, the matrix \bar{P} can be considered as the transition matrix of an absorbing Markov chain and the states in $\mathcal{B}_t = \{B_i, i = 1, \dots, n\}$ are the transient states. Hence, the transition matrix P can be interpreted as the restriction of a transition matrix of an absorbing Markov chain to finite transient states.

Remark. As for the closed systems, nonautonomous time-periodic velocity fields with period τ or autonomous velocity fields will lead to a time-homogeneous Markov chain when calculating the transition matrices for a series of time intervals with length τ .

6.2. Transport in double-open systems

We now extend the open system to a double-open system with constant inflow and outflow of mass. Therefore, we describe the evolution of a mass distribution in the open system by a flux through a Markov chain (cf. [65]).

In the transfer operator framework, the evolution of the density f over A under S with additional constant inflow can be described by an affine operator: $L^1(A) \rightarrow L^1(A)$, defined by

$$\mathcal{P}f + \varsigma,$$

where \mathcal{P} is the conditional Perron-Frobenius operator and density ς describes the new mass that is released into the system after time step τ .

We now consider the transition matrix obtained from a finite-rank approximation of the conditional transfer operator. Let $\mathcal{B}_t = \{B_i, i = 1, \dots, n\}$ be a partition of A . Let the $n \times n$ transition matrix P contain the transition probabilities between the states for a discrete time step of length τ . Then P is substochastic and describes the mass evolution on a system with outflow, just like the transition matrix of the open system $S_A : A \rightarrow X$ introduced in Section 6.1.

Since A is a subset of an infinite strip X , we now also want to take into account new mass that comes into our domain A . We model the constant source via the mass distribution σ over \mathcal{B}_t that is injected to the system at every time step τ . A state B_i is called *source state* if $\sigma_i \neq 0$. In our set-up, we model boxes that are on A_1 as source states.

Now let \mathbf{v}_0 denote the box-discretized initial mass distribution on A . The mass distribution \mathbf{v}_1 after a time step of length τ is given by

$$\mathbf{v}_1 = \mathbf{v}_0 P + \sigma.$$

In the following, we assume, that the underlying velocity field on the infinite strip X is time-periodic with time-period τ (or autonomous) and a constant amount of mass enters the domain A of the open system over time. When we fix the length of all further time steps $k \in \mathbb{N}$ as time period of the velocity field, we obtain a time-homogeneous Markov chain with P as transition matrix restricted to the states in A .

Let \mathbf{v}_k denote the mass distribution after $k \in \mathbb{N}_0$ time steps of length τ . The mass distribution \mathbf{v}_k after k time step of length τ is given by

$$\mathbf{v}_k = \mathbf{v}_{k-1} P + \sigma$$

or – starting with the initial distribution \mathbf{v}_0 – by

$$\mathbf{v}_k = \mathbf{v}_0 P^k + \sigma(P^{k-1} + P^{k-2} + \dots + I).$$

Under the assumption, that all states in A are transient, $|\lambda_i| < 1$ for each eigenvalue λ_i of P . Then, the term $\mathbf{v}_0 P^k$ tends to 0 and the geometric series of matrices converges. Hence the mass distribution converges to the product of the source distribution and the fundamental matrix:

$$\mathbf{v}_{\text{inv}} := \lim_{k \rightarrow \infty} \mathbf{v}_k = \sigma(I - P)^{-1}.$$

The invariant mass distribution \mathbf{v}_{inv} satisfies

$$\mathbf{v}_{\text{inv}} = \mathbf{v}_{\text{inv}}P + \boldsymbol{\sigma}$$

and is therefore a fixed point of an affine transformation and thus solves the linear equation $(I - P)\mathbf{v}_{\text{inv}} = \boldsymbol{\sigma}$. The invariant mass distribution depends on both the transition matrix and the source distribution. The leading eigenvalue λ_1 of P controls the exponential rate at which \mathbf{v}_k approaches the invariant mass distribution and the difference $\mathbf{v}_k - \mathbf{v}_{\text{inv}}$ is approximately in the direction of the corresponding left eigenvector [65].

Remark. We have focused above on the case of a time-homogeneous Markov chain and a constant source. Further, one can consider the following cases:

1. Time-homogeneous Markov chain and a time-periodic source: In this case, the asymptotic mass distribution oscillates with the same period as the source between different asymptotic values (see in [65] for the details).
2. Time-homogeneous Markov chain and time-dependent source: Let $\boldsymbol{\sigma}(k)$ denote the source for time $k \in \mathbb{N}_0$. The mass distribution \mathbf{v}_k is then given by

$$\mathbf{v}_{k+1} = \mathbf{v}_kP + \boldsymbol{\sigma}(k).$$

In general, there is no asymptotic value for the mass distribution. Under the assumption of transience, very early source distributions will eventually lose their influence on the mass distribution.

3. Time-periodic Markov chain and a constant source: In this case, the asymptotic mass distribution oscillates similarly as in (1.) with the same period as the time-period of the Markov chain between different asymptotic values.

Let us first derive the values for Markov chain with time-period 2, that is, the transition matrix is given as P_0 for all even times and as P_1 for all odd times. Let the initial distribution be $\mathbf{v}_0 = 0$. The mass distributions at the following times are then $\mathbf{v}_1 = \boldsymbol{\sigma}$, $\mathbf{v}_2 = \boldsymbol{\sigma}P_1 + \boldsymbol{\sigma}$, $\mathbf{v}_3 = \boldsymbol{\sigma}P_1P_0 + \boldsymbol{\sigma}P_0 + \boldsymbol{\sigma}$, $\mathbf{v}_4 = \boldsymbol{\sigma}P_1P_0P_1 + \boldsymbol{\sigma}P_0P_1 + \boldsymbol{\sigma}P_1 + \boldsymbol{\sigma}$, and so on.

For the even times the mass distribution converges to

$$\begin{aligned} \mathbf{v}_{\text{even}} &= \boldsymbol{\sigma}(I + P_1 + P_0P_1 + P_1P_0P_1 + P_0P_1P_0P_1 + P_1P_0P_1P_0P_1 + \dots) \\ &= \boldsymbol{\sigma}(I + P_0P_1 + (P_0P_1)^2 + \dots) + \boldsymbol{\sigma}P_1(I + P_0P_1 + (P_0P_1)^2 + \dots) \\ &= (\boldsymbol{\sigma} + \boldsymbol{\sigma}P_1)(1 - P_0P_1)^{-1} \end{aligned}$$

and for the odd times to

$$\begin{aligned} \mathbf{v}_{\text{odd}} &= \boldsymbol{\sigma}(I + P_0 + P_1P_0 + P_0P_1P_0 + P_1P_0P_1P_0 + P_0P_1P_0P_1P_0 + \dots) \\ &= (\boldsymbol{\sigma} + \boldsymbol{\sigma}P_0)(1 - P_1P_0)^{-1}. \end{aligned}$$

under the assumption of transience.

When now the Markov chain has time-period r with transition matrices P_0, P_1, \dots, P_{r-1} , the asymptotic mass distribution oscillates between the values

$$\mathbf{v}_{[i]} = (\boldsymbol{\sigma} + \boldsymbol{\sigma}P_{\pi^i(1)}P_{\pi^i(2)} \cdots P_{\pi^i(r-1)} + \boldsymbol{\sigma}P_{\pi^i(2)} \cdots P_{\pi^i(r-1)} + \cdots \boldsymbol{\sigma}P_{\pi^i(r-1)}) \cdot (1 - P_{\pi^i(0)}P_{\pi^i(1)} \cdots P_{\pi^i(r-1)})^{-1}, \quad i = 1, 2, \dots, r,$$

where $\pi^i(x) = x + i \bmod r$.

4. Time-dependent Markov chain and constant source: Let $P(k)$ denote the transition matrix for time $k \in \mathbb{N}_0$. The mass distribution \mathbf{v}_k is given by

$$\mathbf{v}_{k+1} = \mathbf{v}_k P(k) + \boldsymbol{\sigma}.$$

As in (2.) there is in general no asymptotic mass distribution and the mass distribution can only be considered at finite times.

5. To complete this list, one could consider a combination of a time-periodic Markov-chain and a time-periodic source and the combination of a time-dependent Markov chain and a time-dependent source.

6.3. Organizing structures

A *chaotic saddle* (or *nonattracting chaotic invariant set*) $C \subset A$ is an invariant set of the open system $S_A : A \rightarrow X$ (that is, $S_A(C) = C$) that contains a dense chaotic orbit. Trajectories in C thus never escape the mixing region. The *stable manifold* S_C contains trapped trajectories that converge towards the chaotic saddle in forward time. The *unstable manifold* U_C contains trajectories that converge to the chaotic saddle in backward time. It follows that S_C is forward invariant ($S_A(S_C) \subset S_C$) and U_C is a backward invariant set ($S_A^{-1}(U_C) \subset U_C$).

While the chaotic saddle and its manifolds have Lebesgue measure zero, they still have a profound impact on the finite-time mixing properties of the flow. In particular, particles near the stable manifold of the chaotic saddle stay longer in the system and follow the unstable manifold on their way out. Therefore the geometry and fractal dimension of these structures has been studied and related to the mixing properties of the flow [7, 38, 40, 102].

Open flow systems can also contain islands of positive Lebesgue measure (invariant sets that contain stable orbits) in the mixing region, where material is trapped forever and no material from outside of these islands gets inside. Further, one can consider almost-invariant sets and coherent sets, as defined for closed systems in Section 3.2.

We refer to the chaotic saddle, its manifolds, and to islands collectively as invariant phase-space structures. Here, we focus on the extraction of invariant phase-space structures or almost-invariant sets.

Numerical extraction of organizing structures from the transition matrix P .

The invariant phase-space structures that organize mixing will be extracted directly from the $n \times n$ transition matrix P , defined in Section 6.1. Recall that the region of interest $A \subset X$ is discretized by boxes $\{B_1, \dots, B_n\}$, and P_{ij} gives the conditional probability that a randomly selected point in B_i has its image in B_j . In the general case there is more than one communicating class (P is reducible). Assume, without loss of generality, that P is in the canonical form (see equation (2.4)), that is, P has the form of a block-lower-triangular matrix, where the blocks P_1, \dots, P_r describe the transition probabilities restricted to the (transient) communicating classes C_1, \dots, C_r of the Markov chain. In Section 2.5.3 we have described the spectrum and the set of nonnegative eigenvectors (and their meaning) of a substochastic transition matrix P .

We now relate the phase-space structures of interest, which are approximately represented by unions of boxes, to states and classes in the Markov chain defined in terms of P . It is clear that those sets of boxes in the discretization of the domain A that correspond to self-communicating classes can trap particles (by definition there is a nonzero probability to stay in the respective set of boxes) and thus play a crucial role in mixing. In particular, they can either reveal a chaotic saddle or an (almost-)invariant set with positive Lebesgue measure. In practice, the self-communicating classes of P can be found by graph-based approaches such as Tarjan's algorithm [90].

In the following, we describe an alternative approach based on the spectrum of P . The set of particles that stay in A for all times can be computed as $A_\infty = \bigcap_{k \in \mathbb{N}} S_A^k(A)$, which is a backward-invariant set [13]. In the open flow literature [7, 38, 40, 102], A_∞ corresponds to the unstable manifold when A contains a chaotic saddle. Now let $\mathbf{w}_0 = \frac{1}{n} \mathbf{1}$ and consider $\mathbf{w}_{k+1} = \mathbf{w}_k P$, where \mathbf{w}_k is normalized at each step. Then it is intuitively clear that the limiting vector (that is, \mathbf{w}_∞ , which could also be obtained in terms of an eigenvector of P) is supported on A_∞ . Similarly, when P^T is considered, the limiting vector is supported on the stable manifold.

We now make this intuitive notion more precise using Theorem 2.5.2. With P sorted into blocks P_1, \dots, P_r as above, let λ_i denote the eigenvalue of P_i with largest real part – the *Frobenius-Perron eigenvalue*. The eigenvalue λ_i is real and nonnegative. A class is called a *maximal class* if $\lambda_j < \lambda_i$ for all $j \neq i$ such that C_j is accessible from C_i . There exists a nonnegative real left λ_i -eigenvector \mathbf{w} of the substochastic transition matrix P if and only if C_i is a maximal class, where the support of \mathbf{w} corresponds to states that are accessible from the respective class. A nonnegative left λ_i -eigenvector \mathbf{w} is a linear combination of eigenvectors with this property corresponding to maximal classes with the same eigenvalue. The nonnegative left λ_i -eigenvectors \mathbf{w} correspond to quasi-stationary distributions, that is, \mathbf{w} is invariant under time evolution conditioned on absorption not yet having taken place.

An analogous result holds for nonnegative right λ_i -eigenvectors $\hat{\mathbf{w}}$ of P (see Corollary 2.5.3). Here the respective classes are maximal classes of P^T and are reachable by the states in the support of the right eigenvector.

A single self-communicating class, or several self-communicating classes that

are not reachable from each other, correspond to maximal classes of P and P^T . When such class C_i with simple Frobenius-Perron eigenvalue λ_i includes a chaotic saddle, states in the support of its left nonnegative eigenvector can be reached by C_i , and states in the support of its right nonnegative eigenvector can reach C_i . In this case, we can use the states in the support of the left (right) eigenvector to approximate a neighborhood of the unstable (stable) manifold of the chaotic saddle. The intersection of the two invariant manifolds corresponds to a neighborhood of the chaotic saddle.

In general, not all self-communicating classes are maximal (see Example 2.5.5), and one obtains signed leading eigenvectors for the respective non-maximal classes or even eigenvectors with zero entries for states that are accessible from (or can reach) the respective non-maximal class. When now a non-maximal class C_i of P (or P^T) includes a chaotic saddle, states in the support of its left signed eigenvector can be reached by C_i (or the states in the support of the its right signed eigenvector can reach C_i). In the degenerate case, where the eigenvector shows not all states that can be reached by (or can reach) C_i , these states can be found by graph-based algorithms as depth-first-search.

(Almost-)invariant sets will also be identified as self-communicating classes or as intersections of the support of corresponding left and right eigenvector.

Alternatively, the location of a stable manifold or an (almost-)invariant set can be detected by high expected residence times (see Section 2.5.4). These can be calculated by means of the fundamental matrix $(I - P)^{-1}$. The expected number of time steps a particle is in the domain A , when starting in a given state B_i , is

$$E(T | B_i) = \sum_{j=1}^n (I - P)^{-1}_{ij}.$$

An unstable manifold can be detected by high expected residence times for the backward-time dynamics. To compute these, we use the backward-time matrix \tilde{P} , where \tilde{P} is P^T with normalized rows.

Chapter 7.

Transport and mixing studies in open systems

In an open system, where the fluid stays in a mixing region only for a finite time-span and most fluid material leaves the domain relatively quickly, the outgoing fluid is only partially mixed. So unlike in closed systems, which can be systems that are mixing in the ergodic theoretical sense, this will not lead to perfect homogenization.

This chapter presents three open example systems.

The first two sample systems we consider, the open double gyre flow (in Section 7.1) and the open lid-driven-cavity flow (in Section 7.2), are defined on a domain $X \subset \mathbb{R}^2$ as explained in Section 6.1, consisting of an unbounded unmixed region X_1 , a bounded mixing region X_2 and an unbounded mixed region X_3 (Figure 6.1). As the velocity field on X is assumed to be divergence-free, it can be derived from a stream function $\Psi : X \times \mathbb{R} \rightarrow \mathbb{R}$, with

$$\Psi(x, y, t) = \Psi_b(x, y) + \Psi_m(x, y, t).$$

Here Ψ_b is the stream function of the stationary background flow, which shifts fluid through the mixing region and acts on all of X , and Ψ_m is the stream function of the mixer, which acts only on X_2 . The mixer is time-periodic: $\Psi_m(x, y, t) = \Psi_m(x, y, t + \tau)$, where $\tau > 0$ is the period. For a smooth superposition of the two stream functions Ψ_b and Ψ_m , a standard bump function supported on X_2 can be used, but computationally this has turned out to be unnecessary (see [68]). The velocity field $\mathbf{u} = (u_1, u_2)$ on X is then obtained from

$$u_1 = \frac{\partial \Psi}{\partial y}, \quad u_2 = -\frac{\partial \Psi}{\partial x},$$

and has the form

$$\mathbf{u}(x, y, t) = \begin{cases} \mathbf{u}_b(x, y), & \text{for } (x, y) \in X_1 \cup X_3 \\ \mathbf{u}_b(x, y) + \mathbf{u}_m(x, y, t), & \text{for } (x, y) \in X_2 \end{cases}$$

where \mathbf{u}_b is the stationary background velocity field and \mathbf{u}_m is the velocity field of the time-periodic mixer. We model the background flow in our examples as a constant homogeneous flow (translational flow), but other flow profiles such as parabolic flows are possible as well.

When we now send constantly fluid of two different colors through the mixing region with an underlying time-periodic velocity field, a periodic pattern is

formed in the mixed region (Figure 7.1). In Section 6.1 we described the evolution on a bounded subdomain A and in Section 6.2 we additionally considered constant inflow of mass. Here we use as subdomain A a connected set that contains an inlet region $A_1 \subset X_1$, the mixing region $A_2 = X_2$ and an outlet region $A_3 \subset X_3$. The inlet region contains all fluid mass that will enter the mixing region in one time step of length τ . By using signed mass distributions we can now study the mixing processes for two types of fluids on the domain A . We are particularly interested in mixing patterns that arise on the outlet region A_3 , when the two types of fluids have passed the mixing region. The outlet region is chosen as the minimal subset, we need to describe the periodic mixing pattern. We study the mixing patterns and apply the mixing measures defined in Section 4.2 on the limit distributions in the outlet region.

For both example systems we extract first the organizing structures. We study how the manifolds of chaotic saddles and almost-invariant sets organize the mixing processes. For the first example system, we examine in parameter-studies how the mixing quality can be quantified from the underlying structures.

In Section 7.3 we consider as third example system a 2D model of a magnetic mixing valve [69], which shows a parabolic flow profile. Two fluids have to pass an obstacle. Behind the obstacle a mixing region is generated. We aim here to extract the organizing structures of the system with our transfer operator approach.

7.1. The double gyre mixer

For our first sample system we use the periodically perturbed double gyre flow (see Section 5.1) as mixer with stream function

$$\Psi_m = -\alpha \sin(f(x, t)\pi) \sin(\pi y),$$

where $f(x, t) = \epsilon \sin(\omega t)x^2 + (1 - 2\epsilon \sin(\omega t))x$.

For the background flow, we choose the constant velocity field

$$\Psi_b = \beta y, \quad \mathbf{u}_b = \begin{pmatrix} \beta \\ 0 \end{pmatrix}, \quad \text{with } \beta > 0.$$

The velocity field on X has the form

$$\mathbf{u}(x, y, t) = \mathbf{u}_b(x, y) + \mathbf{u}_m(x, y, t)\mathbb{1}_{[0,2]}(x),$$

where $\mathbf{u}_m(x, y, t)$ is derived from the stream function Ψ_m . The velocity field on the mixing region matches the velocity field of the double gyre with windage with wind factor β in Section 5.1. Here, however, the mixing region has no periodic boundaries and the fluid will leave this region after some time.

We choose the inlet region $A_1 = [-\beta, 0) \times [0, 1]$, which ensures that all mass is carried into the mixing region A_2 within a unit time step, the period of the mixer. For the outlet region, we choose $A_3 = (2, 2 + \beta] \times [0, 1]$ (Figure 7.1).

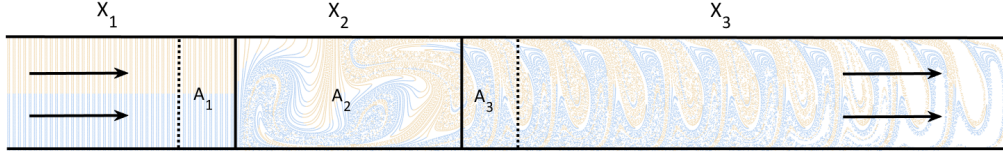


Figure 7.1.: Setup of the double gyre mixer.

Evolution of the mass distribution in the double-open system. For setting up the finite state Markov chain, we divide the domain $A = [-\beta, 2 + \beta] \times [0, 1]$ in 49,152 square boxes of side length 0.0078 and initialize 100 test particles on a regular grid in each box. To form the transition matrix restricted to non-absorbing states, we integrate the test particles with the classical Runge-Kutta method with step size $h = 0.01$ from $t = 0$ to $t = 1$, which corresponds to one period of the periodic mixer dynamics. The boxes in A_1 correspond to the source states.

In Figure 7.2 the first steps of a signed density evolution \mathbf{v}_k , $k = 1, \dots, 12$, on the set A are illustrated, for parameters $\alpha = 0.5$, $\epsilon = 0.4$ and set $\beta = 0.5$ for the inflow velocity. Here we set the initial mass distribution \mathbf{v}_0 as the zero vector, so that no fluid is in the mixer at the beginning. The invariant mass distribution is independent of the initial mass distribution, since it leaves the system eventually. As a constant source we consider a signed mass distribution describing the two different types (or colors) of fluid. Boxes with particles of the first type get the value 1 and boxes with the second type get the value -1 .

With \mathbf{v}_0 being identically zero, the fluids to be mixed are introduced as horizontal stripes into the inlet by adding $\boldsymbol{\sigma}$, resulting in $\mathbf{v}_1 = \boldsymbol{\sigma}$. In the next iteration, the inlet contents are mapped into the mixing region and get mixed by $\mathbf{v}_1 P$. Additionally, new fluid is introduced into the inlet, resulting in $\mathbf{v}_2 = \mathbf{v}_1 P + \boldsymbol{\sigma}$. This is repeated several times. For $k \geq 4$, mixed fluid can be found in the outlet region. For $k \geq 8$ the mixing pattern in the outlet seems to stabilize, indicating that \mathbf{v}_k quickly converges to the invariant distribution \mathbf{v}_{inv} . In Subsection 7.1.2, we therefore focus on the invariant distribution \mathbf{v}_{inv} and study how well the two fluids are mixed in the outlet region.

7.1.1. Organizing structures

In this subsection, we first study the organizing structures in more detail for two choices of parameter ϵ and then extract the organizing structures in an expanded parameter study for ϵ .

Extraction of organizing structures. First, we fix again the parameters $\alpha = 0.5$, $\epsilon = 0.4$ and $\beta = 0.5$. In Figure 7.3 we follow a set of particles in the unbounded domain X for 8 time steps. We observe that some particles (colored in red) stay longer in the mixing region. They reveal the unstable manifolds of two chaotic saddles (see e.g. in Figure 7.3, bottom plot at time $t = 8$). Instead of following

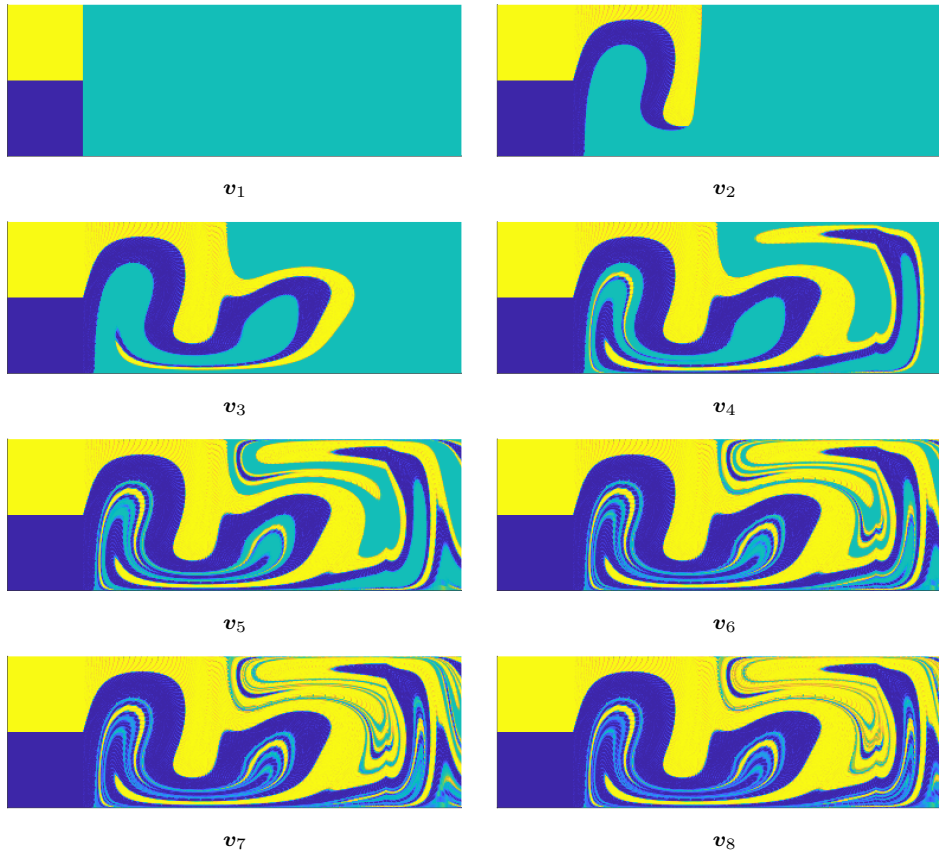


Figure 7.2.: Evolution of the mass distribution v_k for the double gyre mixer with parameters $\alpha = 0.5$, $\epsilon = 0.4$ and $\beta = 0.5$.

particles, we now use the transition matrix P to extract the organizing structures of the system. By Tarjan's algorithm, we find two self-communicating classes (shown in Figure 7.5(a)), which both approximate a chaotic saddle. Neither self-communicating class is accessible from the other, and hence both of them are a maximal class of P and P^T .

The transition matrix P has the leading real eigenvalues $\lambda_1 = 0.5817$ and $\lambda_2 = 0.5775$. In Figure 7.6 the nonnegative left and right eigenvectors for λ_1 and λ_2 are shown. The support of the leading first and the support of the second left eigenvector approximate each an unstable manifold of one of the two chaotic saddles. The result matches the observed structures in Figure 7.3.

We can now follow the particles that have stayed longer in the system backward in time. At time $t = 0$ they lie close to the stable manifolds. The supports of the leading first and second right eigenvectors approximate the stable manifolds of the two chaotic saddles. The saddles themselves are approximated by the intersections of the different supports (dark blue and orange).

The expected residence time for a particle to stay in the domain A of the mixer,

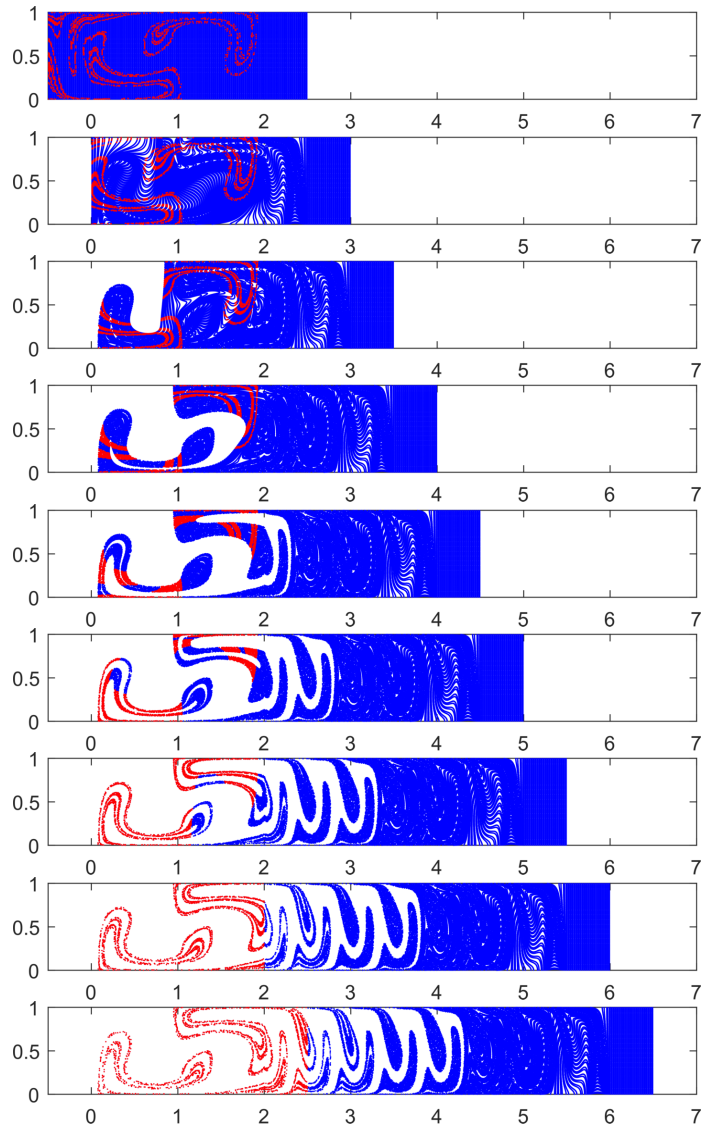


Figure 7.3.: Evolution of a set of particles for the double gyre mixer on the unbounded domain X with system parameters $\alpha = 0.5$, $\epsilon = 0.4$ and $\beta = 0.5$. Position of the particles after 0, 1, 2, 3, 4, 5, 6, 7, 8 time steps. Particles that stay longer in the mixing region (red) reveal the stable and unstable manifolds.

given that the particle started in a particular box, can be extracted easily from the transition matrix. The expected residence times in forward and backward time are shown in Figure 7.8. Particles that start in boxes near the stable manifold stay longer in the mixing region. Accordingly, we see that regions of high expected residence times in forward time correspond to regions with high values in the leading right eigenvectors of the transition matrix P . Similarly, particles close

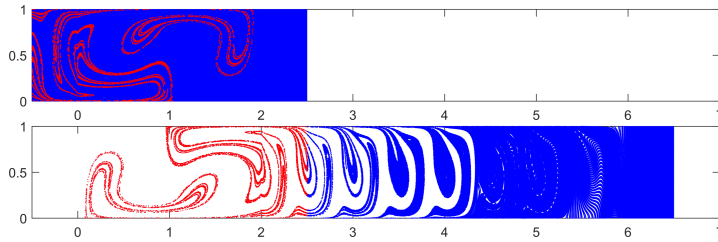


Figure 7.4.: Evolution of a set of particles for the double gyre mixer on the unbounded domain X with system parameters $\alpha = 0.5$, $\epsilon = 0.35$ and $\beta = 0.5$. Position of the particles after 0 and 8 time steps. Particles that stay longer in the mixing region (red) reveal the stable and unstable manifolds.

to the unstable manifold stay longer in the mixing region when we follow them backward in time. Regions of high expected residence times in backward time correspond to regions with high values in the leading left eigenvectors of the transition matrix P .

We now change the parameter ϵ to 0.35. First, we follow again a set of particles in the unbounded domain X for eight time steps and observe certain particles that stay longer in the mixing region (Figure 7.4). Again, we find two self-communicating classes (shown in Figure 7.5(b)), which look quite similar to the self-communicating classes for $\epsilon = 0.4$. But here the self-communicating class in the upper right of the phase space (colored in orange) is accessible from the other self-communicating class in the lower left of the phase space (colored in blue). The respective Frobenius-Perron eigenvalues are $\lambda_1 = 0.5553$ (corresponding to the blue colored self-communicating class) and $\lambda_2 = 0.5519$ (corresponding to the orange colored self-communicating class). Hence, both self-communicating classes are maximal classes of P but only the blue colored is a maximal class of P^T . In Figure 7.7 the left and right eigenvectors for λ_1 and λ_2 are shown. There are two nonnegative left eigenvectors, since both classes are maximal. Some entries of \mathbf{w}_1 corresponding to states that can be reached from the blue self-communicating have relatively low values, these are the states that cannot be reached from the orange self-communicating class. By considering the support of the eigenvector we see the states that can be reached from the respective self-communicating class more clearly. There is a nonnegative right eigenvector $\hat{\mathbf{w}}_1$ with respect to λ_1 . The right eigenvector $\hat{\mathbf{w}}_2$ with respect to λ_2 is signed. Entries for states that can reach the orange class by passing the blue class have a positive sign, entries for states that can reach the orange class not by passing the blue class have a negative sign and a relatively small absolute value. The support of the signed vector shows the states that can reach the orange self-communicating class more clearly. As before, the supports of the eigenvectors match the observed structures in Figure 7.4 and the intersections of the supports of the eigenvectors show again the self-communicating classes.



Figure 7.5.: Self-communicating classes of P for the double gyre mixer with system parameters $\alpha = 0.5$, $\epsilon = 0.4$, and $\beta = 0.5$ (a) and with system parameters $\alpha = 0.5$, $\epsilon = 0.35$, and $\beta = 0.5$ (b). There are two self-communicating classes: Boxes that belong to the first self-communicating class are colored in blue and boxes that belong to the second second are colored in orange.

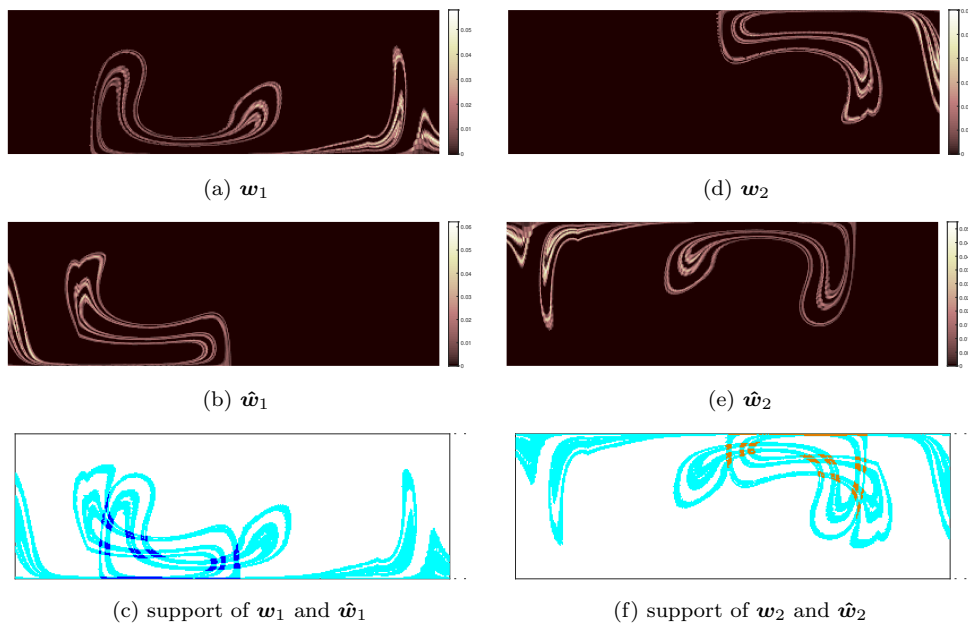


Figure 7.6.: Double gyre mixer with system parameters $\alpha = 0.5$, $\epsilon = 0.4$, and $\beta = 0.5$. First left eigenvector \mathbf{w}_1 (a), first right eigenvector $\hat{\mathbf{w}}_1$ (b), second left eigenvector \mathbf{w}_2 (d) and second right eigenvector $\hat{\mathbf{w}}_2$ (e) of P . The support of these left and right eigenvectors (c), (f), where entries $< 10^{-12}$ are treated as zero. The intersection (dark blue, orange) approximates each a chaotic saddle.

Parameter study ϵ . We now fix again the parameters $\alpha = 0.5$ and $\beta = 0.5$, and analyze the evolution of the organizing structures and spectrum with changing system parameter ϵ . We vary ϵ from 0 to 2.5.

In Figure 7.9 we show the number of self-communicating classes. For most

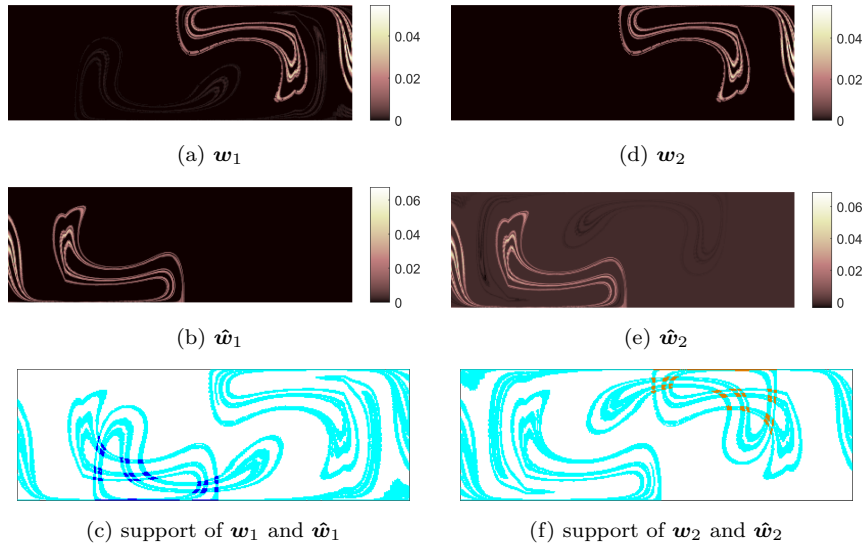


Figure 7.7.: Double gyre mixer with system parameters $\alpha = 0.5$, $\epsilon = 0.35$, and $\beta = 0.5$. First left eigenvector \mathbf{w}_1 (a), first right eigenvector $\hat{\mathbf{w}}_1$ (b), second left eigenvector \mathbf{w}_2 (d) and second right (signed) eigenvector $\hat{\mathbf{w}}_2$ (e) of P . The support of these left and right eigenvectors (c), (f), where entries $< 10^{-12}$ are treated as zero. The intersection (dark blue, orange) approximates each a chaotic saddle.

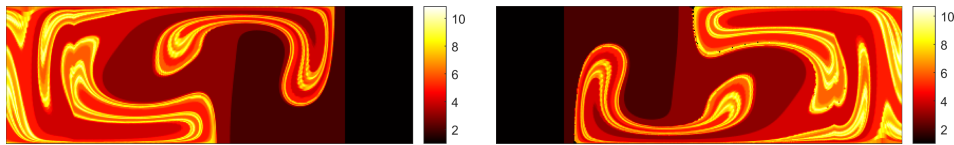


Figure 7.8.: Double gyre mixer with system parameters $\alpha = 0.5$, $\epsilon = 0.4$ and $\beta = 0.5$. Expected residence times $E(T|\cdot)$ in forward (left) and backward time (right).

choices of ϵ we find exactly two self-communicating classes. For ϵ between 1.1 and 1.275 and for $\epsilon \geq 2$ there are no self-communicating classes. Directly before the self-communicating classes disappear they separate in three (for $\epsilon = 1.075$) and five self-communicating classes (for $\epsilon = 1.975$).

The real parts of the first and second eigenvalues and a selection of extracted self-communicating classes are presented in Figure 7.10. In general, there is no correlation to the leading eigenvalues in the closed double gyre systems with wind factor 0 or wind factor 0.5 (see Appendix B). In case there are self-communicating classes, the eigenvalues are real and represent the Frobenius-Perron eigenvalues corresponding to one of the extracted self-communicating classes. Here, for all ϵ the first and second eigenvalues are relatively similar. In case there are no

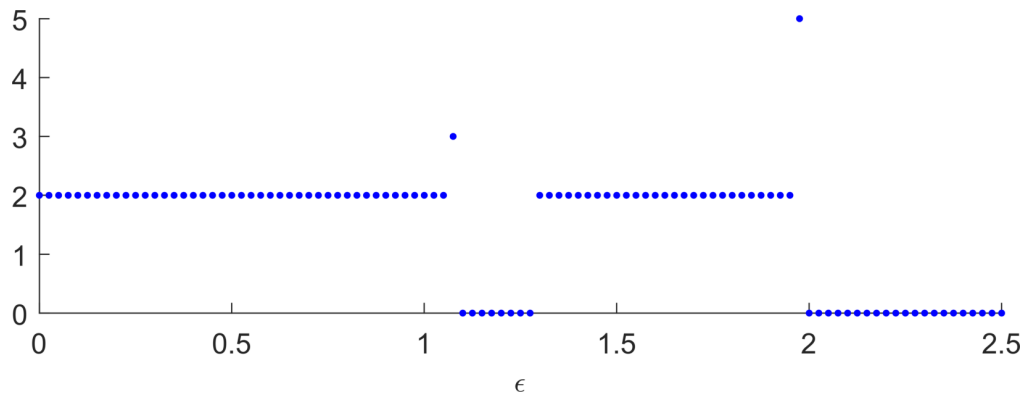


Figure 7.9.: Number of self-communicating classes in the double gyre mixer with different choices of ϵ .

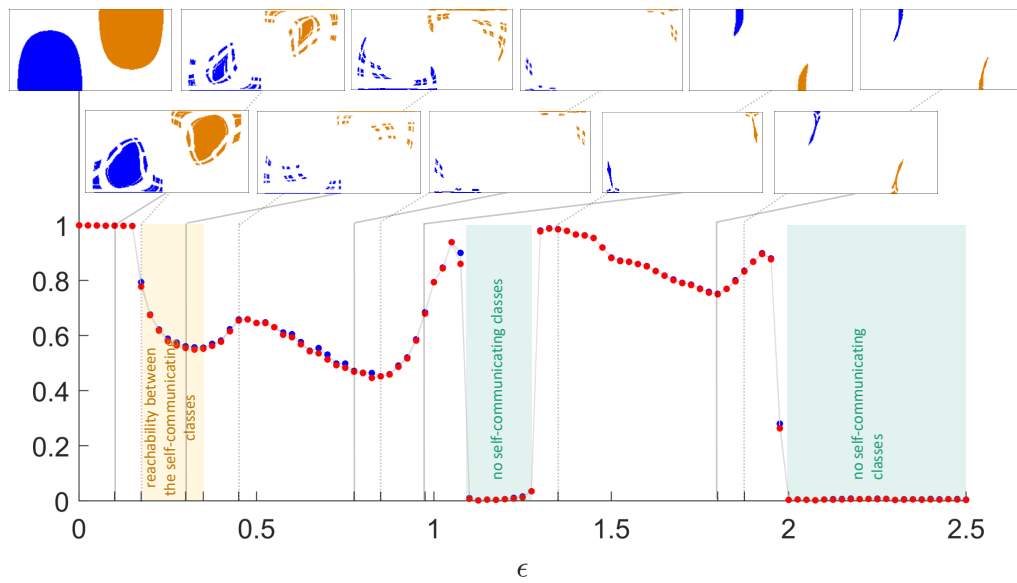


Figure 7.10.: The real parts of the first and second eigenvalues of the transition matrix P for the double gyre mixer with different choices of ϵ ; and a selection of extracted self-communicating classes.

self-communicating classes, in theory all eigenvalues are 0 and we see here only small numerical deviations.

For $\epsilon = 0$, the two self-communicating classes are regular almost-invariant sets with eigenvalues close to 1. For growing ϵ two chaotic saddles evolve. The regular part of the extracted structures becomes smaller until we do not see any noticeable regular part anymore. For ϵ between 0.175 and 0.35, one of the two self-communicating classes is accessible from the other.

In Figure B.2 in the appendix, we show rough approximations of the box-counting dimensions for each of the two self-communicating classes. The eigenvalues are at the beginning still very close to 1, the computed box-counting dimension decreases there faster.

We show the expected residence times for a selection of ϵ in Figure 7.11. We use there the same choices of ϵ as for the selection of self-communicating classes in Figure 7.10, and show furthermore the residence times for $\epsilon = 0.1$, where there are no self-communicating classes. We observe relatively high residence times in the regular structures. In these cases, we show the expected residence times also for a cutted color axis in Figure B.3 in the appendix to reveal further regions with relatively high expected residence times and parts of the domain that can reach the self-communicating classes. The mean expected residence time for boxes in the inlet region is nearly constant around 6 for all ϵ . When there are no self-communicating classes, there are no high expected residence times, since no particle are hold back for longer times; and thus the standard deviation of the expected residence times is low. The corresponding residence time statistics as the means and standard deviations for all different values of ϵ are shown in Figure B.4 in the appendix.

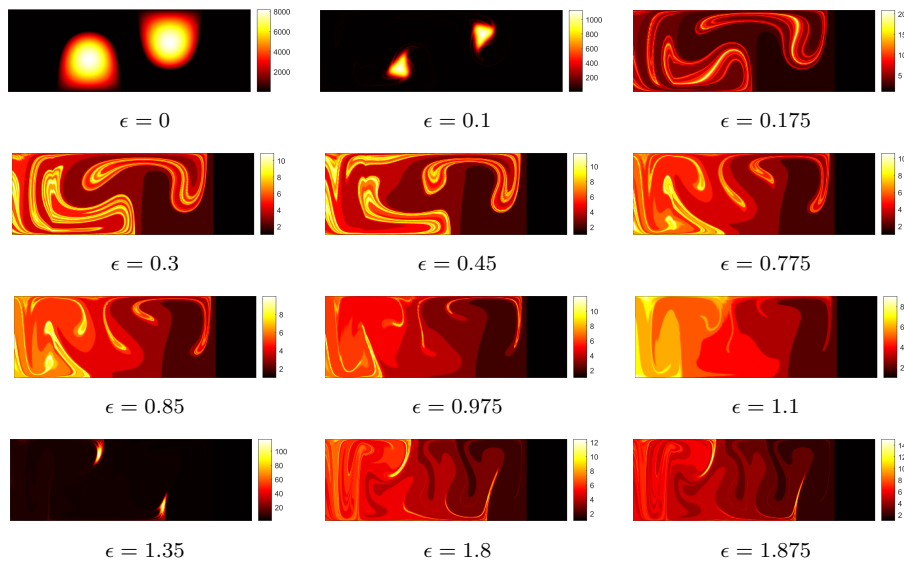


Figure 7.11.: Expected residence times for different choices of ϵ .

7.1.2. Mixing of two types of fluids

In this subsection, we consider the mixing of two types of fluids in the open double gyre mixer. First we quantify the mixing patterns in the parameter study for ϵ from the previous subsection. Then we consider the problem of finding the optimal source (for fixed parameters) and aim to use a structure-based mixing measure.

Parameter study ϵ . As a constant source we now consider a signed mass distribution describing the two different colors of fluid. Boxes in the upper half of A_1 with particles of the first color get the value 1 and boxes in the lower half of A_1 with the second color -1 . We fix again $\alpha = 0.5$ and $\beta = 0.5$ and vary ϵ from 0 to 2.5 (as in Subsection 7.1.1). For each setting, we compute the invariant mass distribution \mathbf{v}_{inv} .

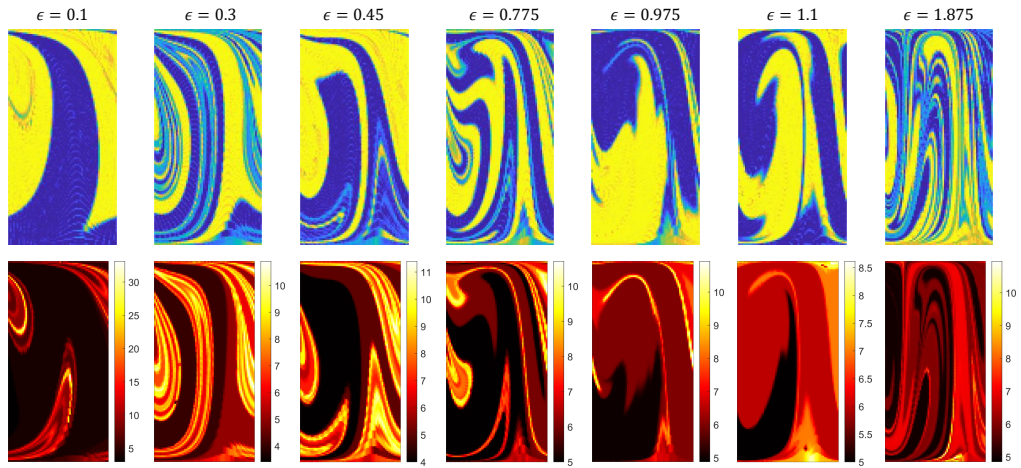


Figure 7.12.: \mathbf{v}_{inv} (top) and $E(T|\cdot)$ in backward time, shown in A_3 , for the double gyre mixer for different choices of ϵ . $\alpha = 0.5$ and $\beta = 0.5$ are fixed.

In Figure 7.12 we show the resulting mixing patterns restricted to the outlet region A_3 for different choices of ϵ in the top row. In the bottom row are the respective expected residence times fields in backward time. Similarly as the FTE fields in backward time in the closed setting, the expected residence times fields in backward time show a correspondence to the resulting mixing patterns in the open setting. The mixing patterns of two types of fluids are dictated by the unstable manifolds of the two chaotic saddles. In regions of high values in the expected residence times field in backward time (and so neighborhoods of the unstable manifolds of the two chaotic saddles), the fluid material stayed a longer time in the mixing region and had a chance to be much more stretched and folded. In these regions there is a potential for thinner filaments of blue and yellow. Of course, the mixing patterns also depend on the source distribution in the inlet region A_1 , what we will discuss in the next section.

The different measures of mixing applied to \mathbf{v}_{inv} restricted to A_3 and examples of some invariant mass distributions are shown in Figure 7.13. The mixing quality shows an oscillatory behavior instead of a monotonic dependence on ϵ . The different mixing measures quantify this behavior similarly but there are some deviations in the ranking. The two prominent local minima are at $\epsilon = 0.275$ and $\epsilon = 0.675$ for the sample variance and at $\epsilon = 0.3$ and $\epsilon = 0.775$ for the relative mix-norm. The graph of mean length scale using a bin width tolerance of $\delta = 0.0051$ shows similarities to the graph of the sample variance. If one uses a larger bin width tolerance of $\delta = 0.0095$, more box pairs are in the neighborhood $N(h)$ for the given distance h . The graph of the computed mean length scale then mimics the relative mix-norm.

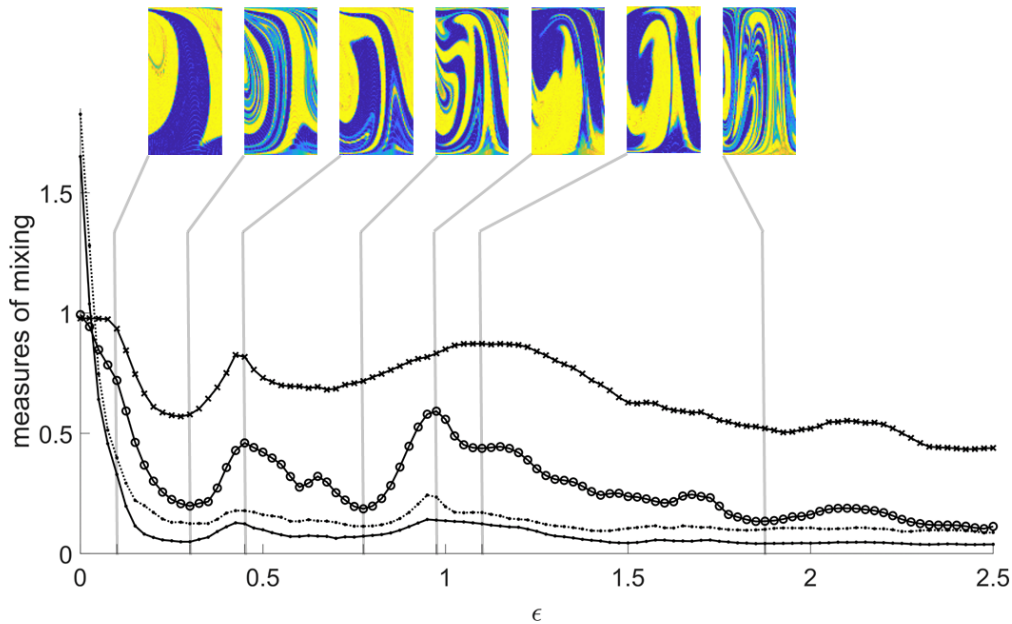


Figure 7.13.: Different measures of mixing applied to \mathbf{v}_{inv} restricted to A_3 for the double gyre mixer for different choices of ϵ . $\alpha = 0.5$ and $\beta = 0.5$ are fixed. Crosses: sample variance, circles: relative mix-norm, dots: mean length scale using $\delta = 0.0095$ (dashed line) and $\delta = 0.0051$ (solid line).

Optimal source and structure-based mixing measures. We elaborate on the question, how we can determine the mixing quality for different source distributions. Instead of looking at the resulting mixing patterns and apply mixing measures, we want to use only the underlying organizing structures to propose the mixing quality. This study is meant as a first step to develop spectral mixing measures for two types of fluids.

We fix the parameter $\epsilon = 0.45$. In this setting, we have two chaotic saddles. The leading two real nonnegative right eigenvectors $\hat{\mathbf{w}}_1$ and $\hat{\mathbf{w}}_2$ correspond each

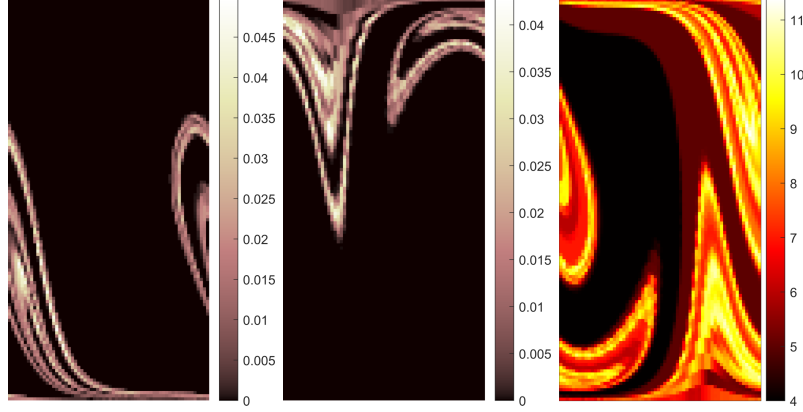


Figure 7.14.: Right eigenvectors \hat{w}_1 (left) and \hat{w}_2 (middle) restricted to the inlet region and the residence times field in backward time restricted to the outlet region (right).

to a neighborhood of a stable manifold of one of the chaotic saddles (in the sense, that the corresponding self-communicating class can be reached by states of the support of the eigenvector). Figure 7.14 shows \hat{w}_1 and \hat{w}_2 restricted to the inlet region.

We consider source distributions $\sigma(\alpha)$, where a line through the midpoint of the inlet separates the two types of fluids. The parameter α denotes the degree between this separating line and the horizontal line. We vary $\alpha = 0, 0.1, \dots, 3.1$. These source distributions are comparable in their unmixed state. Nevertheless, some of them might have a natural advantage, which is not considered here. A selection of source distributions and resulting invariant mass distributions on the outlet region are presented in Figure 7.15. When we compare the mixing patterns to the respective residence times field in backward time (see Figure 7.14, right), we see that the potential for mixing is fulfilled the most for $\alpha = 1.8$.

Fluid patches in the neighborhood of the stable manifolds are transported to a neighborhood of the chaotic saddles, where they experience repeated stretching and folding before they flow out along the unstable manifolds. The two self-communicating classes are of similar size. We assume that the amount of negative and positive mass that flows from the support states of the leading right eigenvectors into the two self-communicating classes should be equal to obtain good mixing. Therefore, we consider $|(\hat{w}_1 + \hat{w}_2)^T \sigma(\alpha)| + |(\hat{w}_1 - \hat{w}_2)^T \sigma(\alpha)|$ as a heuristic spectral mixing measure (for two colors and two chaotic saddles), which is small when the magnitude of both $\hat{w}_1^T \sigma(\alpha)$ and $\hat{w}_2^T \sigma(\alpha)$ and the magnitude of the differences are small.

We compute the relative mix-norm (all normalized by the mix-norm of unmixed horizontal stripes, since the absolute mixing quality should be compared) and sample variance as mixing measures of the invariant mass distributions in the outlet region, shown in Figure 7.16 (left). Both the sample variance and the relative mix-norm quantify the patterns for growing α similarly. Figure 7.16 (right) shows the heuristic spectral mixing measure. Compared to the applied

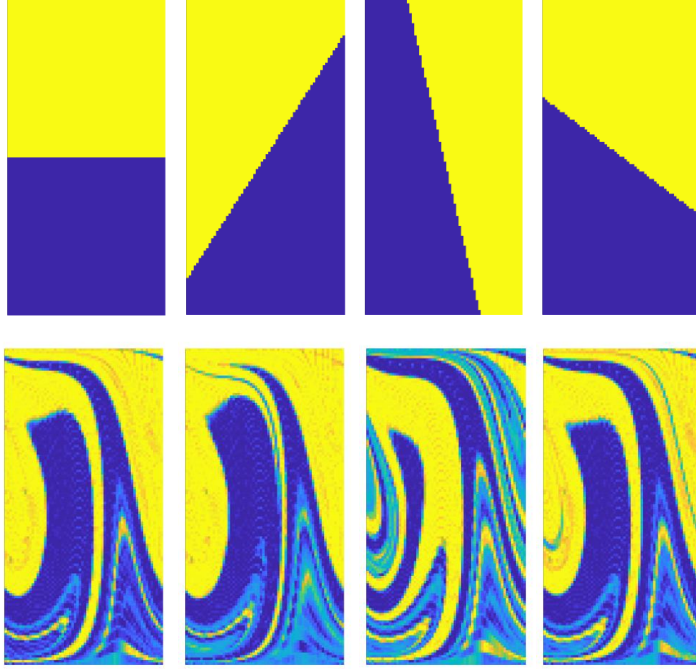


Figure 7.15.: Source distributions for $\alpha = 0, 1, 1.8, 2.5$ and the respective invariant mass distribution on the outlet region.

mixing measures, this heuristic measure appears to be a good indicator for the mixing quality as well.

7.2. The lid-driven cavity mixer.

As a second and more realistic example, we choose the lid-driven cavity flow as mixer [67]. This system has a piecewise-steady velocity field, where the flow pattern switches between two states every $\tau/2$ unit of time, where τ is the period. Its stream function for the period $t \in [k\tau, (k+1)\tau)$ is

$$\Psi_m(x, y, t) = \begin{cases} -U_1 g_1(x, y) + U_2 g_2(x, y) & \text{for } k\tau \leq t < (k + \frac{1}{2})\tau \\ U_1 g_1(x, y) + U_2 g_2(x, y) & \text{for } (k + \frac{1}{2})\tau \leq t < (k + 1)\tau \end{cases}$$

on the domain $[0, a] \times [-b, b]$, where for $\kappa = 1, 2$

$$g_\kappa(x, y) = C_\kappa f_\kappa(y) \sin\left(\frac{\kappa\pi x}{a}\right),$$

with

$$f_\kappa(y) = \frac{2\pi y}{a} \cosh\left(\frac{\kappa\pi b}{a}\right) \sinh\left(\frac{\kappa\pi y}{a}\right) - \frac{2\pi b}{a} \sinh\left(\frac{\kappa\pi b}{a}\right) \cosh\left(\frac{\kappa\pi y}{a}\right)$$

and

$$C_\kappa = \frac{a^2}{2\kappa\pi^2 b} \left[\frac{a}{2\kappa\pi b} \sinh\left(\frac{2\kappa\pi b}{a}\right) + 1 \right]^{-1}.$$

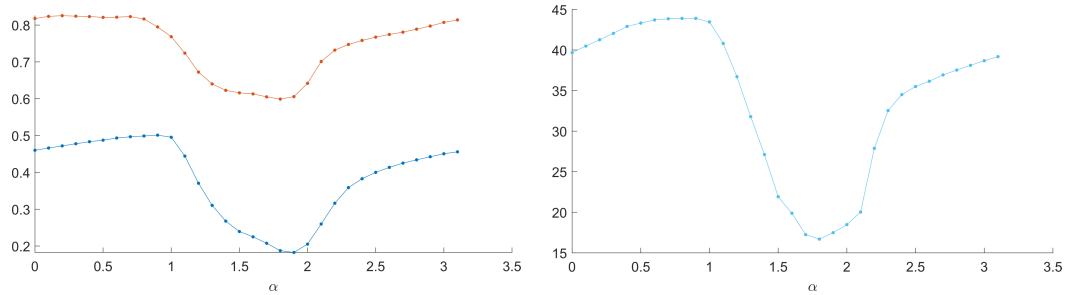


Figure 7.16.: Left: sample variance (red) and relative mix-norm (blue). Right:
 $|(\hat{\boldsymbol{w}}_1 + \hat{\boldsymbol{w}}_2)^T \boldsymbol{\sigma}(\alpha)| + |(\hat{\boldsymbol{w}}_1 - \hat{\boldsymbol{w}}_2)^T \boldsymbol{\sigma}(\alpha)|$.

The ratio U_2/U_1 regulates the streamline pattern of the flow.

We fix parameters $\tau = 1$, $a = 6$ and $b = 1$. The streamlines \boldsymbol{u}_m on the mixing region $X_2 = A_2 = [0, 6] \times [-1, 1]$ with $U_1 = 9$ and $U_2 = 8$ for time instances $t = 0$ and $t = 0.5$ are shown in Figure 7.17. For the background flow, we choose here $\Psi_b = \beta y$, with $\beta = 1$. We divide the domain $A = [-1, 7] \times [-1, 1]$ in 2^{16} square boxes of side length 0.0156. The boxes in $A_1 = [-1, 0] \times [-1, 1]$ correspond to the source states. We initialize 100 test particles on a regular grid in each box and integrate with the classical Runge-Kutta method with step size $h = 0.01$ from $t = 0$ to 1.

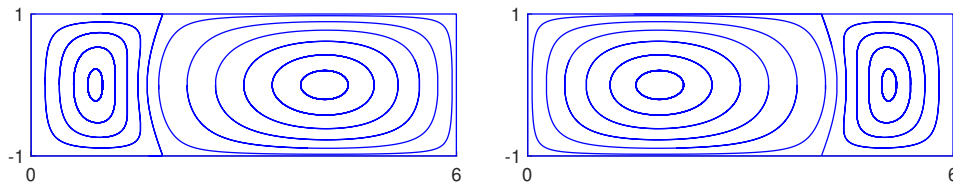


Figure 7.17.: Streamlines of the lid-driven cavity flow with $U_1 = 9$ and $U_2 = 8$ at $t = 0$ (left) and $t = 0.5$ (right).

Evolution of the mass distribution. We set the initial mass distribution \boldsymbol{v}_0 to 0, and fix the parameters $U_1 = 9$ and $U_2 = 8$ and $\beta = 1$. In Figure 7.18 the first steps of the density evolution \boldsymbol{v}_k , $k = 1, \dots, 8$, on the set A are illustrated. At each iteration the source distribution $\boldsymbol{\sigma}$ is added, which introduces the fluids to be mixed as horizontal stripes into the inlet.

7.2.1. Organizing structures.

We fix again the parameters $U_1 = 9$ and $U_2 = 8$ and $\beta = 1$. By Tarjan's algorithm, we find one self-communicating class. The transition matrix P has the leading real eigenvalue $\lambda_1 = 0.7709$. In Figure 7.19 the left and right eigenvectors for λ_1 are shown. The intersection of the support of these eigenvectors (dark blue) reveals the neighborhood of the chaotic saddle of the system. The structure fills

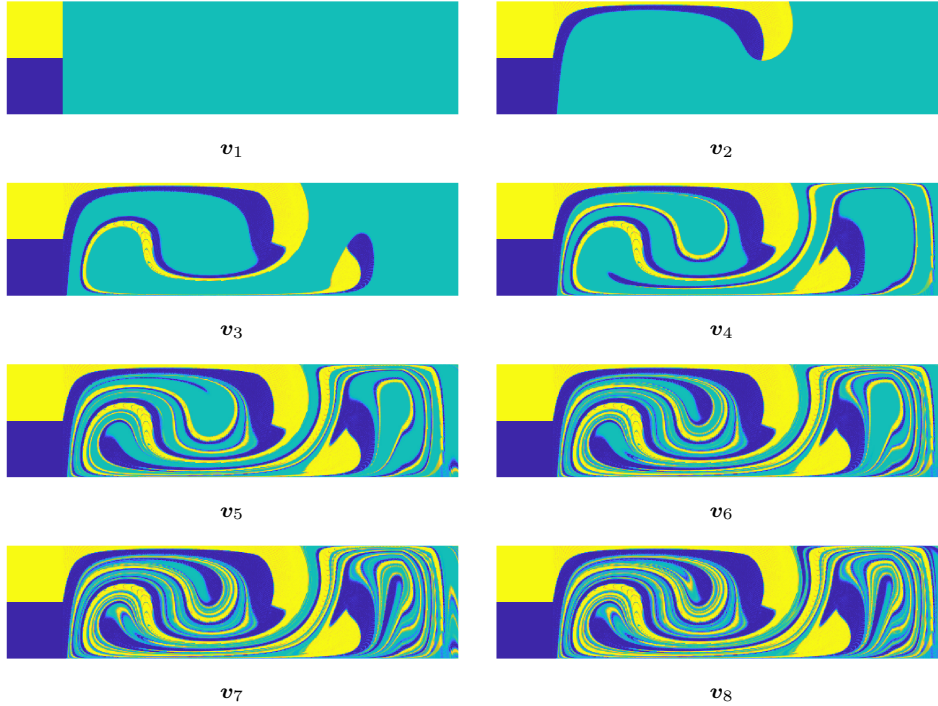


Figure 7.18.: Evolution of the mass distribution v_k , $k = 1, 2, 3, \dots, 12$, for the lid-driven cavity mixer with system parameters $U_1 = 9$, $U_2 = 8$ and $\beta = 1$.

relatively large parts of the mixing region and the stable manifold fills the inlet region extensively.

7.2.2. Mixing of two types of fluids

As a constant source we now consider a signed mass distribution, where boxes in the upper half of A_1 with particles of the first color get the value 1 and boxes in the lower half of A_1 with the second color -1 .

We fix $U_1 = 9$ and vary the parameter U_2 . We consider $U_2 = 6, 6.25, \dots, 12$. Examples of invariant mass distributions restricted to A_3 and the different measures of mixing are shown in Figure 7.20. For this range of parameters the mixing patterns are all relatively well mixed, only for $U_2 \approx 9$ one observes patterns that are slightly less mixed. The graphs of the sample variance and the relative mix-norm show at $U_2 \approx 9$ a difference in the quantification of the mixing quality. The relative mix-norm has one local maximum at $U_2 = 9$ whereas the sample variance has two local maxima at $U_2 = 8.75$ and $U_2 = 9.5$.

The graph of the mean length scale using a bin width tolerance $\delta = 0.0094$ shows also two local maxima, at $U_2 = 8.75$ and $U_2 = 9.25$. If one uses the larger bin width tolerance $\delta = 0.0163$, as in the graph of the relative mix-norm, the graph of the computed mean length scale then has one local maximum at $U_2 = 9$.

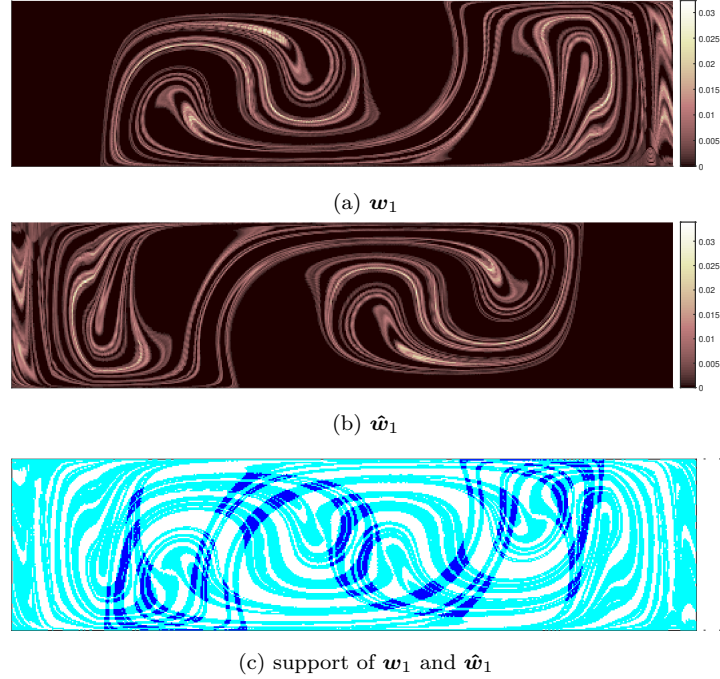


Figure 7.19.: Lid-driven cavity mixer with system parameters $U_1 = 9$, $U_2 = 8$ and $\beta = 1$. First left eigenvector \mathbf{w}_1 (a), first right eigenvector $\hat{\mathbf{w}}_1$ (b) and the support of these eigenvectors, where entries $< 10^{-3}$ are treated as zero. The intersection (dark blue) approximates the chaotic saddle.

7.3. A channel with an obstacle

We now want to consider the action of a magnetic mixing valve. The fluids in this mixing device have similar properties to water and the Reynolds number is in a range of $380 < \text{Re} < 560$. The flow simulations on a simplified 2D domain were derived by the use of the software ANSYS in [69]. The given velocity data is available for 200 time slices (from 0.025 s to 5 s) for a 291×3001 grid. The domain and the velocity field at first time slice $t = 1$ is shown in Figure 7.21. In this example system, the inflow region is separated further into two channels. The two separated channels terminate at an obstacle and join into a common channel. Behind the obstacle a mixing region is generated.

In the velocity data we observe a time periodic behavior with time period 161.

We divide the domain $[-0.08, 0.22] \times [-0.02, 0.02]$ in 2^{16} boxes and initialize 100 test particles on a regular grid in each box. To form the transition matrix restricted to non-absorbing states, we discard boxes where the center point has a velocity close to 0 ($< 10^{-4}$) obtaining $n = 45981$ boxes. We use a simple nearest-neighbor interpolation to obtain the underlying velocity field. We integrate the test particles with the MATLAB function ode45 from time slice $t = 1$ to time

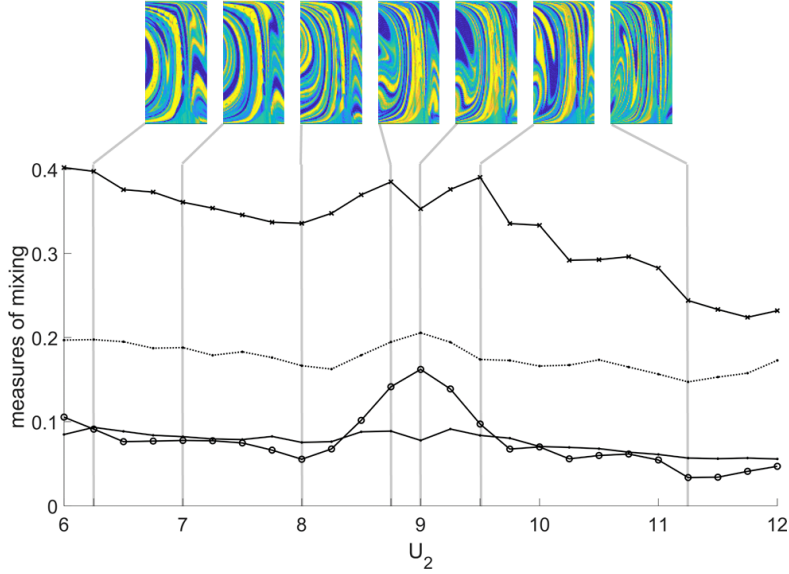


Figure 7.20.: Different measures of mixing applied to \mathbf{v}_{inv} restricted to A_3 for the lid-driven cavity mixer for different choices of U_2 . $U_1 = 9$ and $\beta = 1$ are fixed. Crosses: sample variance; dots: mean length scale using $\delta = 0.0163$ (dashed line) and $\delta = 0.0094$ (solid line); circles: relative mix-norm.

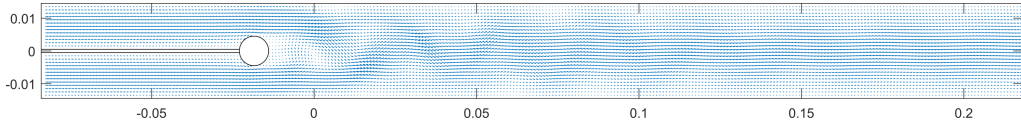


Figure 7.21.: Simplified 2D domain of the mixing valve with indicated velocity field for the first time slice.

slice $t = 161$ and form the substochastic transition matrix P . The evolution of a signed density described by the computed transition matrix is shown in Figure 7.22. At initial time $t = 1$ we fill a subdomain including the inlet region and a part of mixing region with two types of fluids. The initial distribution is here not chosen as a realistic initial distribution for the two fluids that are to be mixed but should demonstrate the ensuing action of the mixing valve modeled by the transition matrix. After one time step of length $\tau = 160$ much of the fluid material that started in the inlet region has already passed the obstacle.

We extract ten self-communicating classes from the time-homogeneous P positioned around the obstacle (Figure 7.23). Nine of the self-communicating classes are relatively small (between 2 and 5 boxes). The largest self-communicating class consisting of 202 boxes and corresponding to the 7-th largest eigenvalue $\lambda_7 = 0.6183$ is positioned behind the obstacle.

In Figure 7.24 we show the right eigenvectors for the first, second, third and

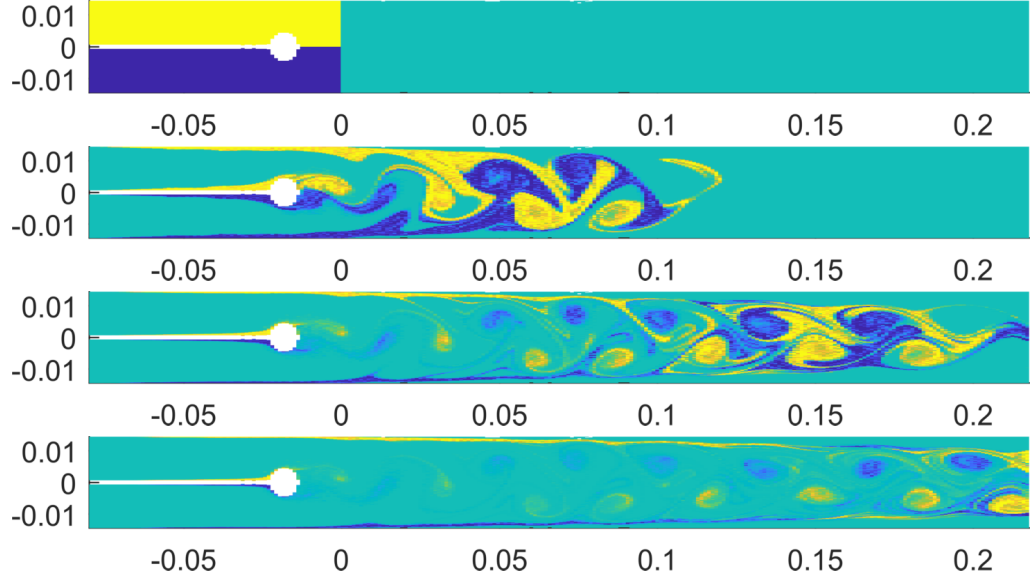


Figure 7.22.: Evolution of a signed mass distribution in the mixing valve.

seventh eigenvalues ($\lambda_1 = 0.8686$, $\lambda_2 = 0.8606$, the following eigenvalues come in pairs, $\lambda_3 = \lambda_4 = 0.8$ and $\lambda_5 = \lambda_6 = 0.7826$). The respective right eigenvectors for the leading eigenvalues show nonzero entries on the boundaries of the channels, where the particles move relatively slowly due to the parabolic flow profile. The eigenvector of the seventh eigenvalue show a more complicated structure.

Figure 7.25 presents the respective left eigenvectors of the first, second, third and seventh largest eigenvalues. They reveal a generated vortex street.

Here, we have not modeled the transport with constant inflow. Since after one time step of length $\tau = 160$ there is already empty space in the mixing region behind the fluid that has passed the obstacle, we would have to partition the chosen time interval τ in shorter time intervals to model the evolution with a source distribution (we only want to use boxes on the left-hand side of the obstacle as source states). This would result to a periodic series of different transition matrices (as in Remark 6.2, third case). Further, we have used here a relatively coarse box-discretization for this size of the domain. However, the actual mixing region is relatively short. To obtain finer approximations of the observed structures by the right eigenvectors, one could consider a smaller subdomain. Also, the shape of boxes are not optimal for the circular obstacle. We come back to this system by using a trajectory-based approach, which is free of a box-discretization, in the next chapter.

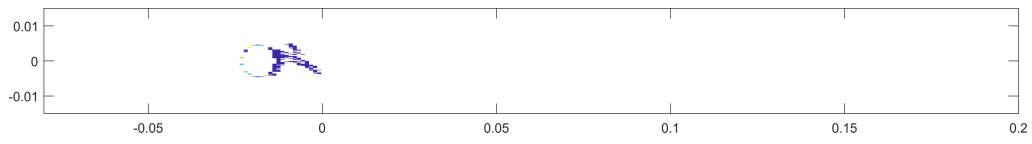


Figure 7.23.: Extracted self-communicating classes in the mixing valve.

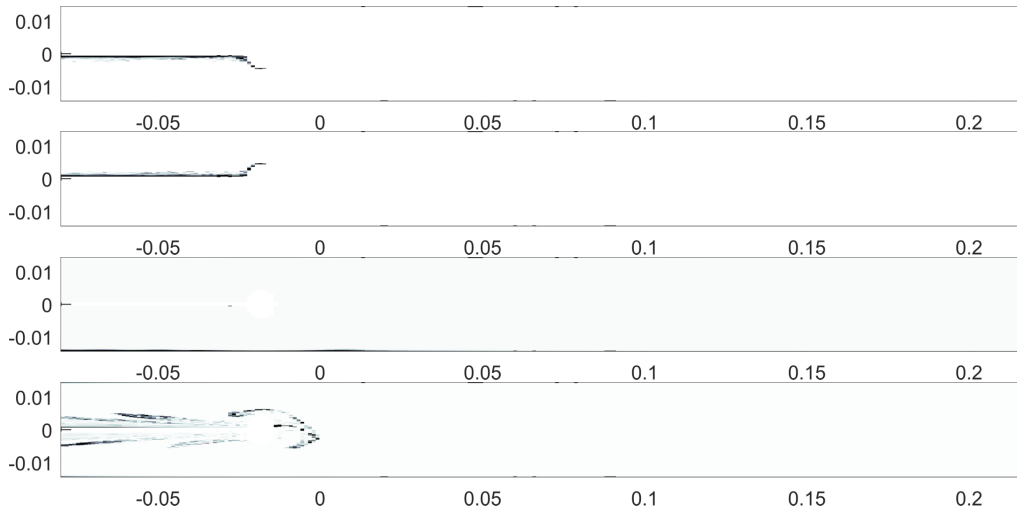


Figure 7.24.: Right eigenvectors corresponding to $\lambda_1, \lambda_2, \lambda_3$ and λ_7 .

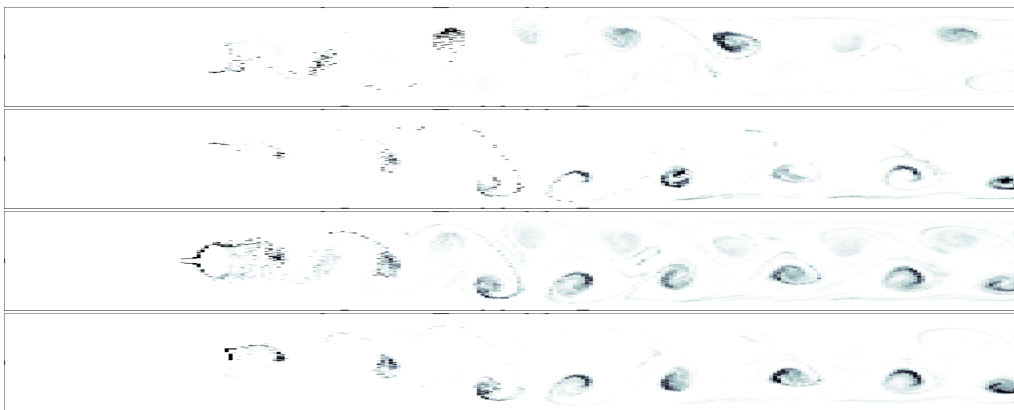


Figure 7.25.: Left eigenvectors corresponding to $\lambda_1, \lambda_2, \lambda_3$ and λ_7

Chapter 8.

Trajectory-oriented description of transport and mixing

In this chapter, we aim to use a data-based approach using diffusion maps to the trajectory space to describe transport and mixing in closed and (double) open systems.

In practice, one might be faced with the problem to have only very sparse trajectory data on the domain of interest. Especially in real world data, the underlying velocity field is often not known. The gaining of large amounts of trajectories may be associated with high costs or may not be feasible, for example when using ocean drifters or other methods to track particles in fluids. Further, in some applications one is interested to extract the macroscopic coherent structures of a certain scale.

Relatively recent trajectory-oriented methods or Lagrangian methods has been developed that cluster on the trajectory data by using graph or network based tools, for example [29, 31, 33]. Banish and Koltai [34] extended the method of diffusion maps [103–105] to sparse trajectory data to estimate finite-time coherent sets.

In Section 8.1 we describe the theory and numerics and in Section 8.2 we come back to three example systems.

8.1. Theory and numerics

Assume, we observe m trajectories $\{\mathbf{x}^i(t)\}, i = 1, \dots, m$ evaluated at T time slices $t \in I_t$ within a finite time step of length τ on a domain A .

The idea of spacetime diffusion maps [34] is to obtain information of the global dynamics (here in form of coherent sets) by using only local information in form of distances of neighboring particles. This is done by introducing a diffusion process on the trajectory data. We follow [34] to construct the so-called *spacetime diffusion map transition matrix*.

Spacetime diffusion map transition matrix. Consider the rotation-invariant kernel

$$k_{\epsilon_0}(\mathbf{x}, \mathbf{y}) = c_r \exp\left(-\frac{\|\mathbf{x} - \mathbf{y}\|_2^2}{\epsilon_0}\right) 1_{\|\mathbf{x} - \mathbf{y}\|_2^2 \leq r},$$

where ϵ_0 is a scaling parameter, r the cutoff radius and c_r scaling parameter.

For each time slice $t \in I_t$, we compute the forward-backward diffusion matrix $B(t)$ with entries [34]:

$$B_{ij}(t) = b_{\epsilon_0,t}(\mathbf{x}^i(t), \mathbf{x}^j(t)),$$

where

$$b_{\epsilon_0,t}(\mathbf{x}, \mathbf{y}) := \frac{1}{d_{\epsilon_0,t}(\mathbf{x})} \sum_{k=1}^m \frac{k_{\epsilon_0}(\mathbf{x}, \mathbf{x}^k(t))k_{\epsilon_0}(\mathbf{x}^k(t), \mathbf{y})}{k_{\epsilon_0,t}(\mathbf{x}^k(t))^2}, \quad d_{\epsilon_0,t}(\mathbf{x}) := \sum_{k=1}^m \frac{k_{\epsilon_0}(\mathbf{x}, \mathbf{x}^k(t))}{k_{\epsilon_0,t}(\mathbf{x}^k(t))}$$

$$k_{\epsilon_0,t}(\mathbf{x}(t)^i) := \sum_j k_{\epsilon_0}(\mathbf{x}^i(t), \mathbf{x}^j(t)).$$

The entries $B_{ij}(t)$ are high if the distance of positions of the i -th and j -th trajectory at time slice t is small. That is, diffusion happens between trajectories that are close.

The *spacetime diffusion map transition matrix* Q for time span τ is given as average of the forward-backward diffusion matrices [34]:

$$Q_{ij} = \frac{1}{T} \sum_{t \in I_t} B_{ij}(t).$$

The matrix Q is stochastic, close to symmetric and can be interpreted as transition matrix of a Markov chain on trajectories.

Banisch and Koltai [34] showed further a link to the transfer operator framework: When the number of trajectories goes to infinity, Q converges to a time-averaged forward-backward transfer operator. Hence Q can be seen as data-based version of this operator.

Open systems and double open systems. When A is the domain of an open system, in general, not all observed trajectories are on A for the whole time span. If we consider a double open system, at every time slice trajectories can enter or leave A . When the positions of particles is only given on A we have incomplete trajectory data.

As mentioned in [34], the construction of Q works also for incomplete trajectory data. A natural way to deal with incomplete trajectories is to assign the distance of a particle to others to ∞ at a time slice t when the particle position at that time slice is not known (or the particle is not in the domain A). The corresponding transition probabilities for that trajectory to others at that time slice are then zero. The distance of such a particle to itself at that time slice is assigned to 0, or respectively the transition probability to itself at that time slice to 1.

If instead the distance of such a particle to itself at that time slice is assigned also to ∞ , the resulting matrix would be substochastic. We denote this matrix in the following by Q_s .

Extraction of organizing structures. In the trajectory-based framework almost-invariant sets and coherent sets can be understood as tight bundles of trajectories. Particles will be together in a coherent set when they are close for a long time.

The information of these coherent structures is coded in the spacetime diffusion map transition matrix Q , since the entries of Q corresponding to two trajectories that are close for all time slices will have a relatively high value. They can be extracted by a hard or soft clustering method on the dominant eigenvectors of Q [34].

Note that the eigenvectors of Q and also the clustering results provides information in space and time, since each entry correspond to a trajectory. That is, one can follow the clusters for the chosen time slices over the given time span τ .

In the applications of Chapter 7 we have extracted chaotic saddles and their manifolds in open systems with a transfer operator method. We should be able to extract these organizing structures also with the trajectory-based method. Some trajectories (starting near the stable manifolds) are staying in the system for a longer time. Choosing an appropriate long time span, we expect to extract them as coherent sets, where the positions of the clusters at the initial time slice reveal the stable manifolds and the positions of the clusters at the final time slice reveal the unstable manifolds.

Modeling and quantification of mixing. In this paragraph, we extend the trajectory-based approach using spacetime diffusion map transition matrices to model mixing of two types of fluids and consider mixing measures that we can use to quantify resulting mixing patterns.

Let us consider again m trajectories $\{\mathbf{x}^i(t)\}, i = 1, \dots, m$, evaluated at T time slices $t \in I_t = \{t_0 = t_{0,1}, t_{0,2} \dots, t_{0,T} = t_1\}$ within a time step of length $\tau = t_1 - t_0$ on a domain A . We interpret fluid particles as small packages of fluid transported along their trajectories. When we now initialize two types of fluid materials, we label a particle that belongs to the first type by 1, and a particle that belongs to the second type by -1. In other word, we initialize a signed mass distribution or $m \times 1$ color vector \mathbf{z}_0 at time $t = t_0$, where $z_{0,i} = 1$, if the i -th particle belongs to the first type, and $z_{0,i} = -1$ if the i -th particle belongs to the second type. Particles that are at any time step $t \in I_t$ very close together are assumed to exchange small parts of their packages of fluid via diffusion. Let Q be the spacetime diffusion map transition matrix for time span τ , constructed as described in Section 8.1. The coevolved color vector after time span τ is modeled as $\mathbf{z}_1 = Q\mathbf{z}_0$.

Remark. When we want to study the evolution of a color vector on A over a series of time intervals $[t_0, t_1], [t_1, t_2], \dots, [t_k, t_{k+1}]$, we can construct a family of transition matrices $\{Q(i)\}_{i=0, \dots, k}$, where $Q(i)$ is the transition matrix with respect to the time interval $[t_i, t_{i+1}]$ with T_i time slices. Note that when we construct each $Q(i)$ only for the trajectories that are in A at some time slice of the time interval $[t_i, t_{i+1}]$, the size of the matrices and the indices for the trajectories can change. Then, after each time interval the color vector \mathbf{z}_i needs to be updated before processing by deleting indices of trajectories that are not in A in the next time interval and adding new indices with (source) color values for trajectories that enter A in the next time interval. Denote this updated color vector by \mathbf{z}'_i . The color vector at time $t = t_{i+1}$ is then given as $\mathbf{z}_{i+1} = Q(i)\mathbf{z}'_i$. We obtain then

a series of color vectors $\mathbf{z}_0 = \mathbf{z}'_0, \mathbf{z}_1, \mathbf{z}'_1, \mathbf{z}_2, \mathbf{z}'_2, \dots, \mathbf{z}_{k-1}, \mathbf{z}'_{k-1}, \mathbf{z}_k$. For our example systems we know prior to the construction how many trajectories we will observe. In that case, we can create one initial color vector \mathbf{z}_0 for all trajectories.

We now want to quantify the degree of mixedness of trajectories at a given time. Let m particles be distributed on domain A with additional color information \mathbf{z} , where \mathbf{z} was calculated by $Q = \frac{1}{T} \sum_{t \in I_t} B(t)$ using time slices $t \in I_t = \{t_0 = t_{0,1}, t_{0,2}, \dots, t_{0,T} = t_1\}$.

As first simple mixing measure one can use the sample variance of the color vector

$$\frac{1}{m-1} \sum_{i=1}^m (z_i - \bar{z})^2,$$

where $\bar{z} = \frac{1}{m} \sum_{i=1}^m z_i$.

As second mixing measure we can again consider the mix-norm by using information on the position of the particles and interpolation in space.

Further, we want to use a mixing measure that uses besides \mathbf{z} only information that are saved in the network $B(t_1)$, the forward-backward diffusion matrix for the last time slice. Here, we try a mixing measure that is based on the mean length scale. Let $\tilde{\mathbf{z}}$ denote the indicator vector of \mathbf{z} . We calculate the inverse of the averaged squared differences of the indicator variable of neighbored pairs of particles in the network $B(t_1)$

$$\frac{1}{N} \sum_{(i,j):B(t_1)_{ij}>0} (\tilde{z}_i - \tilde{z}_j)^2,$$

where N is the number of neighbored pairs (i, j) .

8.2. Example systems

In this section, we present three example systems. As first example system serves again the (closed) double gyre flow to test the mixing measures. As second example system we consider the (double open) double gyre mixer, where we extract the underlying organizing structures. As third example system we consider again the channel with an obstacle, where we consider the transport of two types of fluids and extract the underlying organizing structures.

8.2.1. Double gyre flow

We consider again the closed double gyre flow (see Section 5.1). We set parameter ϵ as 0.2. We initialize 20301 particles on a grid. We set \mathbf{z}_0 in that way that particles with fluid on the left half of the domain get the value 1 and particles on the right of the domain -1.

We obtain the trajectory data by the classical Runge Kutta method for a time span $\tau = 20$. We split the time interval $[0, 20]$ into 20 time intervals of length 1: $[0, 1], [1, 2], \dots, [19, 20]$. For each time interval $[i, i + 1], i = 0, 1, \dots, 19$, we compute $Q(i)$, using 11 time slices of the trajectory data (with $\epsilon_0 = 0.0005$).

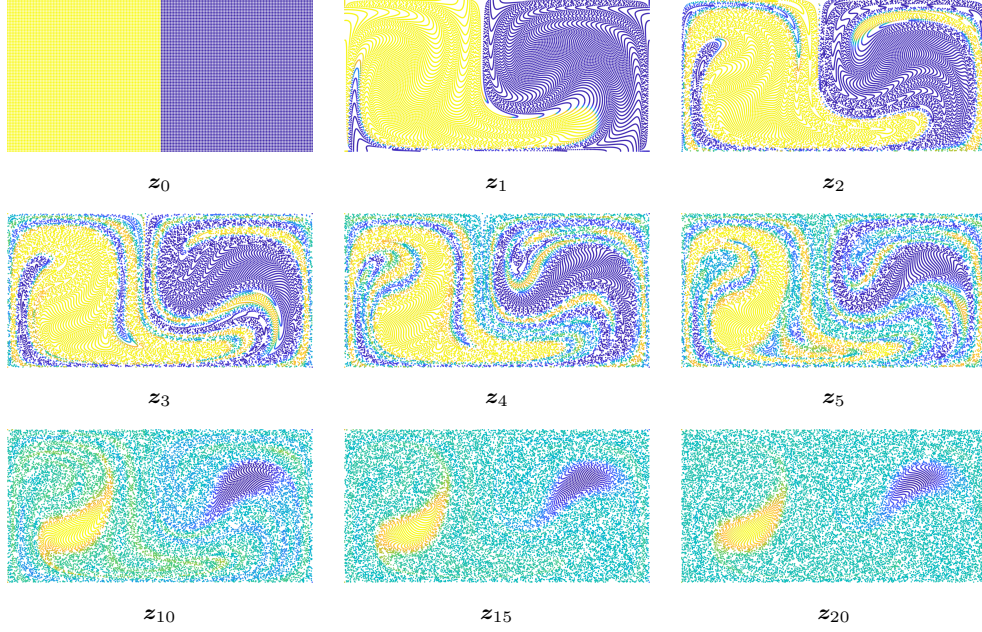


Figure 8.1.: Particles plotted with coevolved color vector z_k (vertical) in the closed double gyre system with parameters $\alpha = 0.5$, $\epsilon = 0.2$ at different times k .

We compute the color vector for the particles at time $t = i$ by $z_{i+1} = Q(i)z_i$. A selection of the computed color vectors z_1, \dots, z_{20} is presented in Figure 8.1. We compute the sample variance, mix-norm and mean scale based measure (Figure 8.2). The applied mixing measures on the color vectors computed by $Q(i)$ show similarly behavior as the mixing measures applied to v_k computed with the transfer operator method (Section 5.1.2).

8.2.2. Double gyre mixer

We consider again the double open double gyre mixer and set parameters $\alpha = 0.5$, $\epsilon = 0.4$ and $\beta = 0.5$ (see Section 7.1). We initialize particles on a grid on X with grid length 0.0136 such that constantly particles enter and leave the domain $A \subset X$ for a short time span $\tau = 1$ and a longer time span $\tau = 5$. The short time span was used in the transfer operator approach to compute the transition matrix P . The longer time span is still lower than the mean expected residence time when starting in the inlet region $A_1 = [-0.5, 0] \times [0, 1]$, which is around 6. We integrate with the classical Runge Kutta method and delete afterwards the positions of particle that are not in $A = [-0.5, 2.5] \times [0, 1]$, so that only the trajectory data on A is available. Over the time span $\tau = 1$ we observe 19,092 trajectories in A and for $\tau = 5$ we have 29,896 trajectories.

For each time span we compute the substochastic spacetime diffusion map transition matrix Q_s with diffusion map parameter $\epsilon_0 = 0.001$ and cutoff radius $r = 2\epsilon_0$. We will use the leading eigenvectors of Q_s to extract the organizing

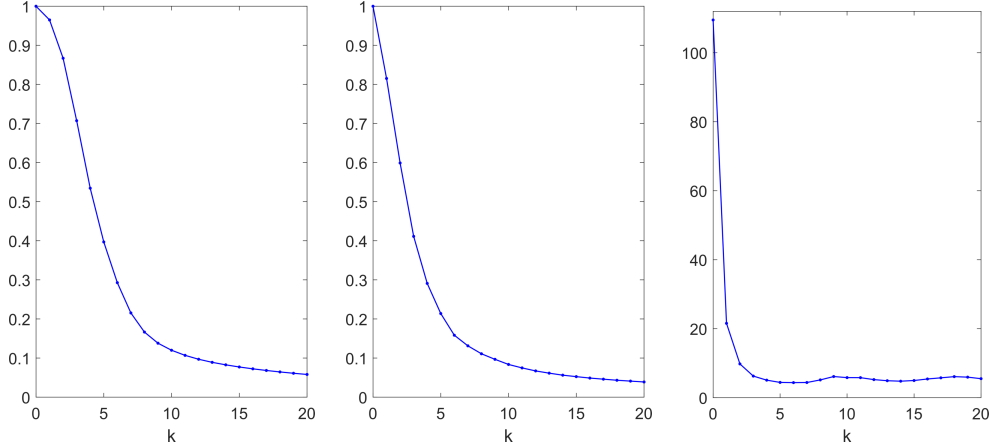


Figure 8.2.: Mixing Measures applied to the color vectors z_k (vertical) for the closed double gyre mixer with parameters $\alpha = 0.5$, $\epsilon = 0.2$. Sample variance (left). Relative mix-norm (middle). Mean length scale based measure (right).

structures. First we use k -means clustering on the eigenvectors to obtain a hard partition into k coherent sets. And then, we use SEBA, where the entries of each output vector denote the likelihood that the underlying particle belongs to a specific coherent set.

Let us first consider the short time span $\tau = 1$. We observe larger gaps after the leading second, fourth and sixth eigenvalue and a relatively large gap after the 12th eigenvalue of Q_s (Figure 8.3(left)). In Figure 8.4 are the results of the k -means clustering and in Figure 8.5 are the results of SEBA using $k = 2, 4, 6$ and 12 clusters.

The k -means algorithm produces a partition of the trajectory data in $k = 2, 4, 6$ and 12 sets respectively. Smaller clusters can be found in the mixing region as well in the inlet region when choosing a higher number of clusters. Particles that are in the inlet region at the final time slice (and also particles that start on the left side of the domain) and particles that start in the outlet region $A_3 = [2, 2.5] \times [0, 1]$ are packed in one cluster.

Shapes of these sets show an agreement with the shapes of the SEBA results. The SEBA algorithm highlights particles that are with high likelihood in a coherent set and also those that show an incoherent behavior. Not all but many of the coherent particles we extract with SEBA are placed around the locations of the stable manifolds of the chaotic saddles at $t = 0$. However, the stable manifolds are widely stretched in space. The time span $\tau = 1$ is too short to extract a manifold as one coherent set. Instead one gets sets of particles that are more lumpy.

We further observe, that the results of k -means and SEBA change, when only particles are followed that are in A at $t = 0$ and no new particles come into the system. Then, particles that start on the left hand side of A , are more likely in a coherent set (Figure 8.6).

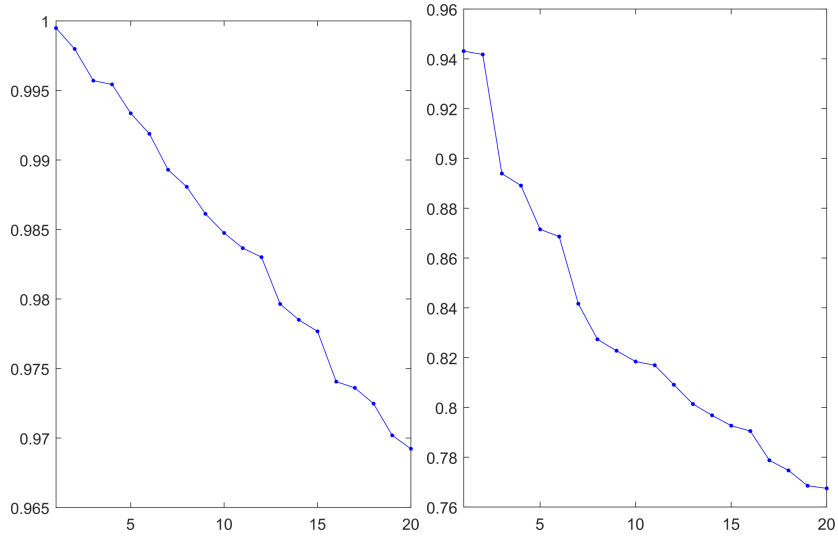


Figure 8.3.: Leading eigenvalues of Q_s for $\tau = 1$ (left) and $\tau = 5$ (right).

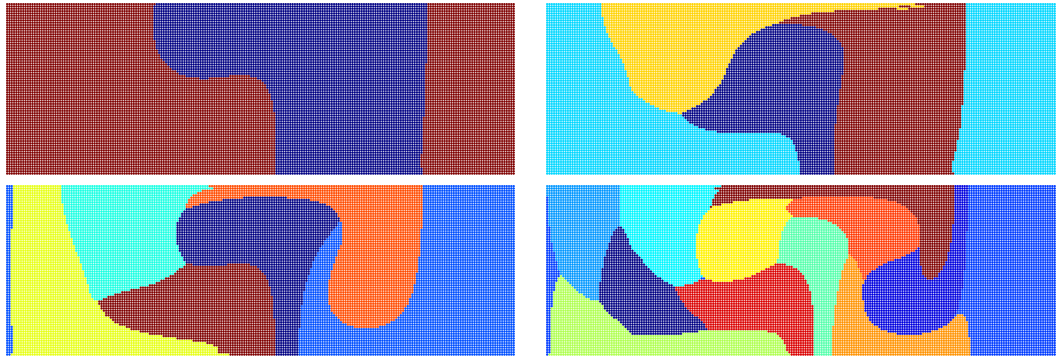


Figure 8.4.: Result of a k -means clustering for $\tau = 1$ on the first two (top left), four (top right), 6 (bottom left) and 12 eigenvectors (bottom right) of Q_s , shown at time slice $t = 0$.

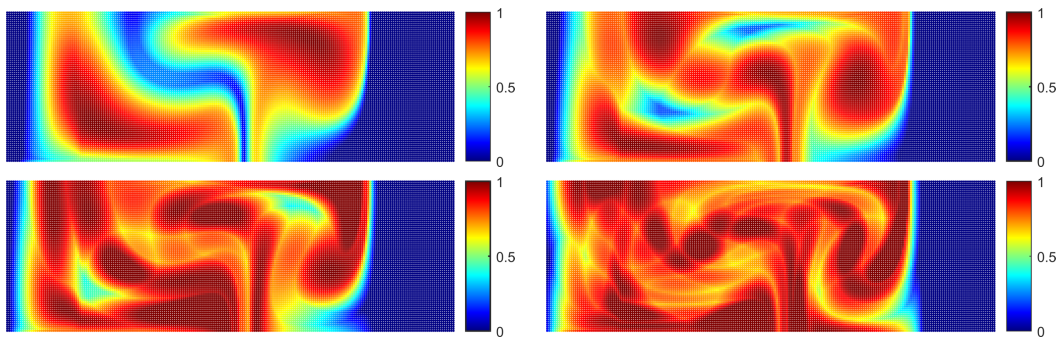


Figure 8.5.: $\tau = 1$: Superpositions of the output vectors obtained by SEBA using two (top left), four (top right), 6 (bottom left) and 12 eigenvectors (bottom right) Q_s , shown at time slice $t = 0$.

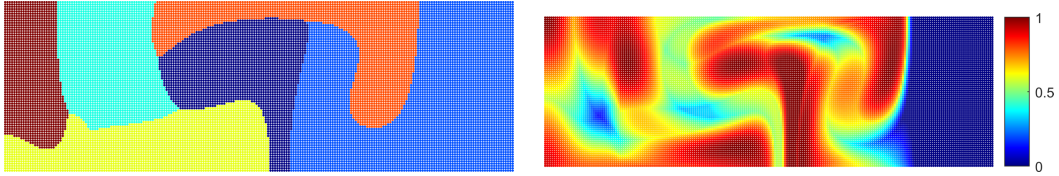


Figure 8.6.: $\tau = 1$: Result of a k -means clustering and superposition of the output vectors obtained by SEBA using six eigenvectors of Q , when no new particles enter A , shown at time slice $t = 0$.

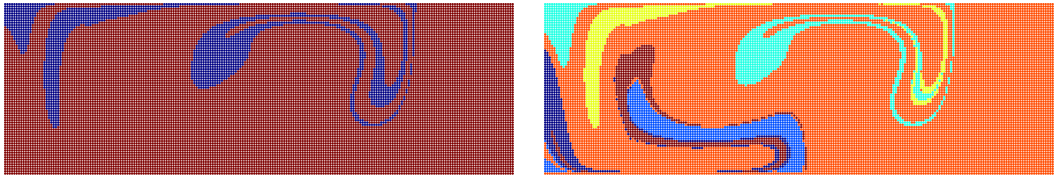


Figure 8.7.: $\tau = 5$. Results of a k -means clustering on the first two (left) and on the first six eigenvectors (right) of Q_s , shown at time slice $t = 0$.
Bottom row:

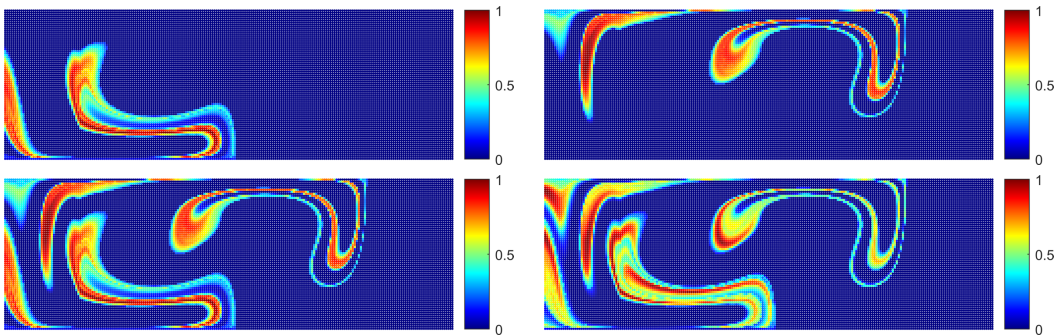


Figure 8.8.: $\tau = 5$. Top row: Output sparse vectors obtained by SEBA using the first two eigenvectors of Q_s , shown at timeslice $t = 0$. Bottom row: Superpositions of the output vectors obtained by SEBA using two (left) and six eigenvectors (right) of Q_s , shown at timeslice $t = 0$.

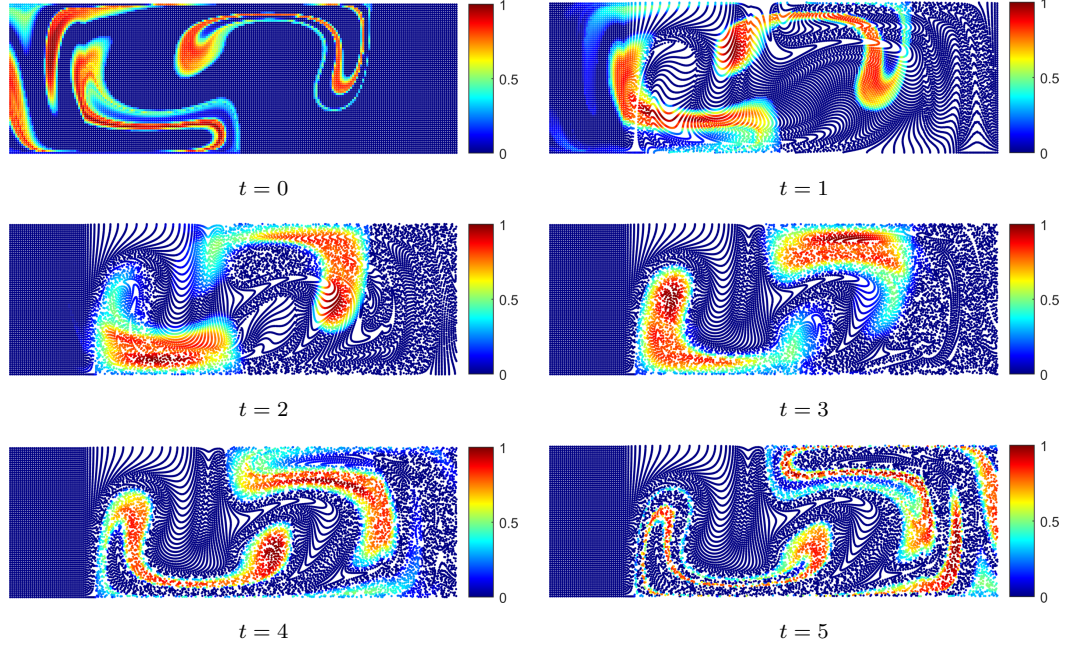


Figure 8.9.: $\tau = 5$. Left: Superposition of two vectors obtained by SEBA, shown at different time slices.

Let us now consider time span $\tau = 5$. We observe the largest gap after the leading second eigenvalue of Q_s (Figure 8.3, right). Further, there is a relative large gap after the sixth eigenvalue.

In Figure 8.7 are the results of the k -means clustering to the leading two eigenvectors and to the leading four eigenvectors of Q_s . All eigenvectors highlight particles near the stable manifolds of both chaotic saddles. Using $k = 2$ clusters, the k -means algorithm shows a coarse approximation of one of the two stable manifolds. Using $k = 6$ clusters, both manifolds – consisting of two and three regions – are separated from the background.

We apply SEBA to the leading two eigenvectors of Q_s . SEBA separates the particles near the stable manifolds into two coherent sets such that each coherent set represents an approximation of a stable manifold of one of the two chaotic saddles (Figure 8.8, top row). The result is in agreement with the extracted stable manifolds of the two chaotic saddles by the eigenvectors of the transition matrix (Section 7.1). Figure 8.9 shows the superposition of the output vectors using two eigenvectors (bottom left) and further using six eigenvectors (bottom right). In the last case there are three coherent regions highlighted instead of two for each manifold.

Note, that the eigenvectors of Q_s as well as the clustering results are spacetime. In Figure 8.9 we show the superposition of the output sparse vectors obtained by SEBA using the leading two eigenvectors of Q_s for different times.

Only few particles that are in the inlet region $A_1 = [-0.5, 0]$ at $t = 1$ belong to a coherent set. When calculating 6 SEBA vectors, more particles that are

at $t = 1$ in A_1 belong to a coherent sets with high likelihood. But even when calculating many SEBA vectors, only few particles that are in A_1 at $t = 2$ belong to a coherent set, since the method searches for coherent sets over the time span τ .

At the final time slice the coherent particles reveal the unstable manifolds of the chaotic saddles.

8.2.3. Channel with an obstacle

We consider again the model of the magnetic mixing valve (see Section 7.3).

We want to model the coevolution of a color vector by spacetime diffusion map transition matrices over five time intervals of equal size (over the given 200 time slices).

First we initialize particles on an equally sized grid with grid length 0.0005 on subdomain $[-0.08, 0] \times [-0.0135, 0.0135]$, such that some particles are already in the mixing region. To obtain the trajectories we integrate with the MATLAB function `ode45`. We construct spacetime diffusion map transition matrices $Q(i)$, $i = 1, 2, 3, 4, 5$, using 11 time slices with diffusion parameter $\epsilon = 0.00001$ and cutoff radius $r = 2\epsilon_0$, where we omit diffusion between trajectories in upper half and lower half of the inlet region since we have two separated inlets.

As color vector z_0 , we set entries of v_0 corresponding to particles in the lower half of the domain to -1 and the remaining entries to 1. In Figure 8.10 we see the evolution of the color vector for five time instances from the initial to final time of the given data set. The given time span of the data is too short that particles that start on the subdomain leave the domain A . Note that we have assumed a periodic velocity field for the evolution by the transfer operator approach in Section 7.3. There, v_1 shows the signed mass distribution at time slice 161. Here, z_5 is the color vector at the final time slice 200.

Now we want to introduce new trajectories into the system at each time slice that is considered for the construction of the transition matrices $Q(i)$. Therefore, we consider at each of these time slices the grid in the inlet regions and initialize new particles at grid points that have no particles in a certain neighborhood. We integrate the particles from the given time slice to the final time and set positions at earlier time slices to NaN. All in all we consider now 20750 trajectories.

We construct one color vector z_0 for all trajectories. Entries of z_0 that correspond to particles that are the lower half for the first time slice that they are in A are set to -1 and else to 1.

We construct $Q(i)$ and also $Q_s(i)$, $i = 1, 2, 3, 4, 5$, where $Q(i)$ or $Q_s(i)$ corresponds to the i -th time interval. With the chosen ϵ the sparsity of the computed matrices lies between 94% and 97%. $Q(i)$ has ones to the diagonal for trajectories that are not inside the domain for the given time interval. Otherwise these particles would loose their initial color to zero. Another possibility would be to use a source color vector and construct the entries of Q only for particles that are in the domain within the given time interval and setting entries corresponding to the others to 0.

In Figure 8.11 we show the evolution of the color vector using Q . The use of

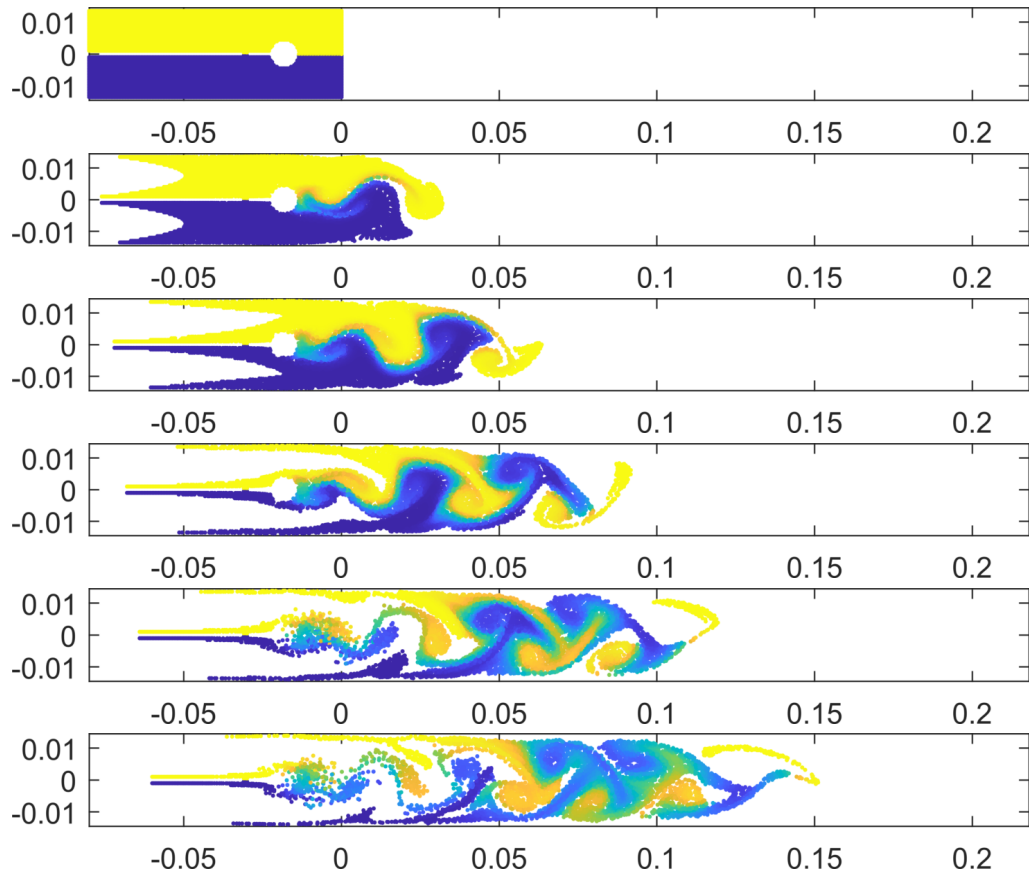


Figure 8.10.: Particles with coevolved color vector by $Q(i)$ in the channel with an obstacle.

the substochastic matrices Q_s would lead to a color loss, shown in Figure 8.12. (A slight color loss would also happen, when we would add ones to the diagonal entries of trajectories that have not yet entered the system.)

We now want to extract organizing structures of the dynamics from the matrices $Q(i)$. Here one could now consider each interval alone or one could try to combine the transition matrices to a single one, what we intend to do here. The product or average matrix are thinkable options for this. By our construction of $Q(i)$ there are many isolated trajectories (trajectories that are not in the domain in the given time interval) corresponding to an diagonal entry 1 (and hence multiple eigenvalue 1). To extract coherent structures we set these diagonal entries to 0. One could also consider the submatrix restricted to entries that correspond to non-isolated trajectories. In Figure 8.13 we present the dominant spectrum of $Q(i)$ and of the average matrix \bar{Q} , as well as the dominant spectrum of $Q_s(i)$ and of the corresponding average matrix \bar{Q}_s .

To extract coherent structures, we now use the SEBA algorithm on the leading 10 eigenvectors of the averaged matrix \bar{Q} . Figure 8.14 shows the output sparse

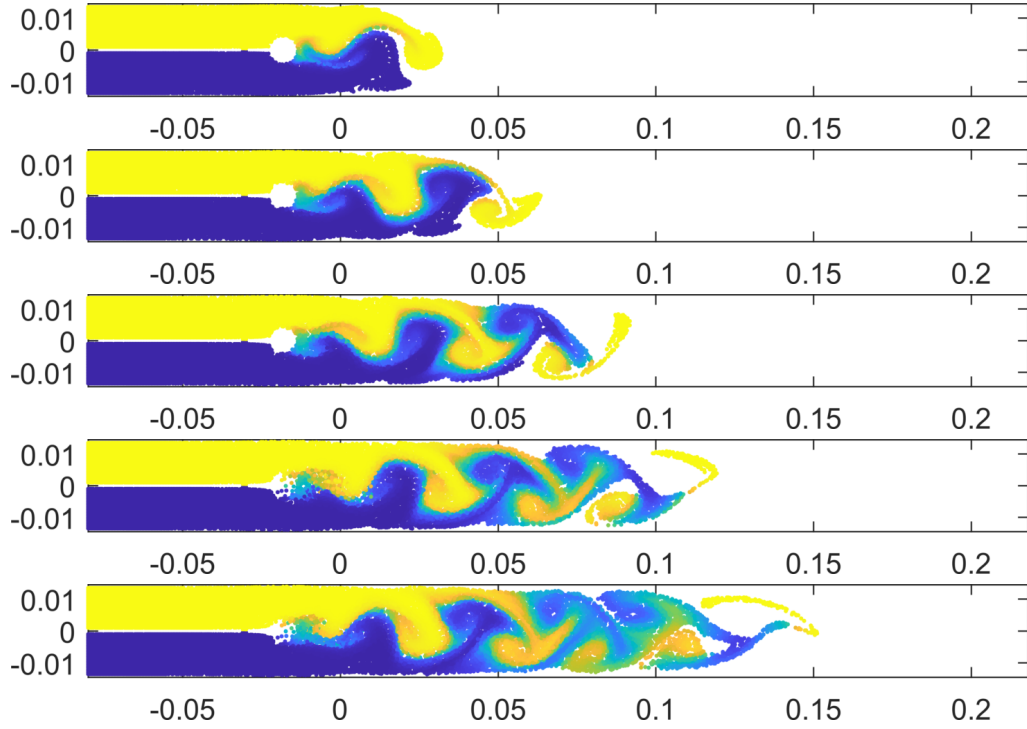


Figure 8.11.: Particles with coevolved color vector by $Q(i)$ in the mixing valve. Here new particles enter the system.

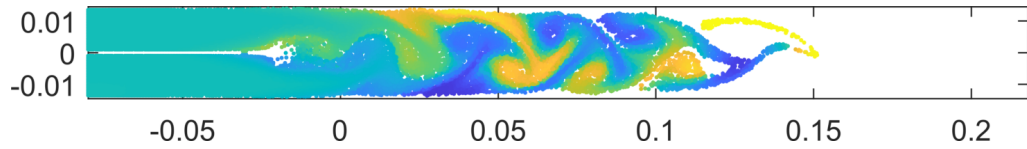


Figure 8.12.: Color vector z_5 computed by using $Q_s(i)$ in the mixing valve.

vectors at the initial time slice and in Figure 8.15 are shown these vectors at the final time slice. The second output vector (top right in Figure 8.14 and second row in Figure 8.15) shows a similar structure as we found in Section 7.3 by the seventh eigenvector of the transition matrix P corresponding to the largest self-communicating class. Using instead 11 eigenvectors would lead to a further partition of this structure in a lower and upper cluster at initial time. At final time these vector highlights the region around the obstacle as well as some gyre cores. The other output vectors highlight further coherent structures, some of these correspond to the generated vortices and some to the outer boundaries of vortices. The superposition of the output vectors at the final time slice is shown in Figure 8.16.

Figure 8.17 shows the superposition of the vectors obtained by SEBA using \overline{Q}_s instead of \overline{Q} at the final time slice. Here, similar structures are highlighted

but some regions show a lower likelihood to belong to a cluster. Particles that are in the inner inlet region at final time are not assigned to a coherent set.

Since we have used here the averaged matrix \overline{Q} , the extracted structures can be interpreted as averaged coherent sets.

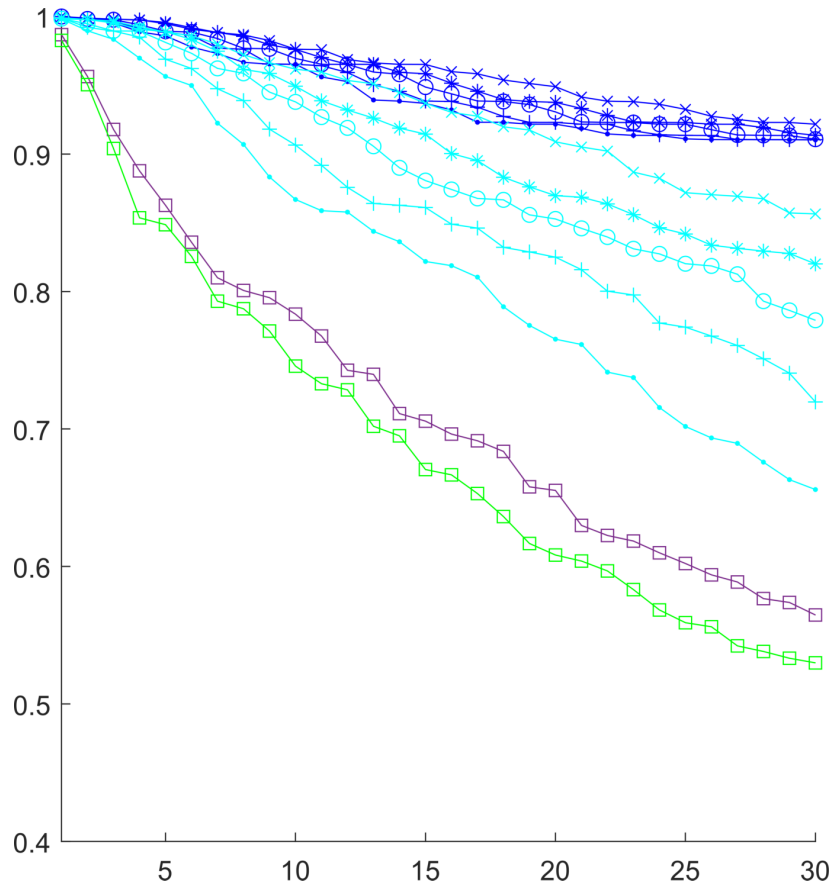


Figure 8.13.: Leading 30 eigenvalues of $Q(i)$ (blue) $Q_s(i)$ (cyan), for $i = 1$ (dots), 2 (plus signs), 3 (circles), 4 (asterisks), 5 (crosses), and their corresponding average matrices \overline{Q} (purple) and \overline{Q}_s (green).

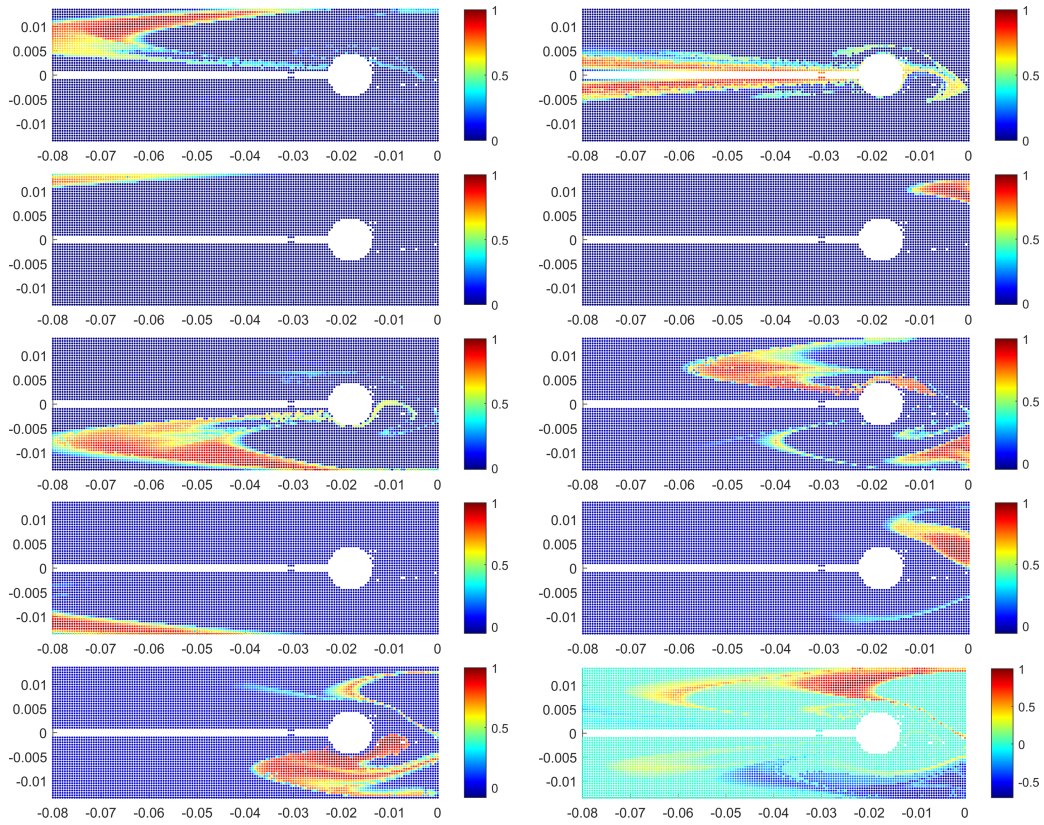


Figure 8.14.: Output sparse vectors obtained by SEBA using \bar{Q} , shown at the initial time slice.

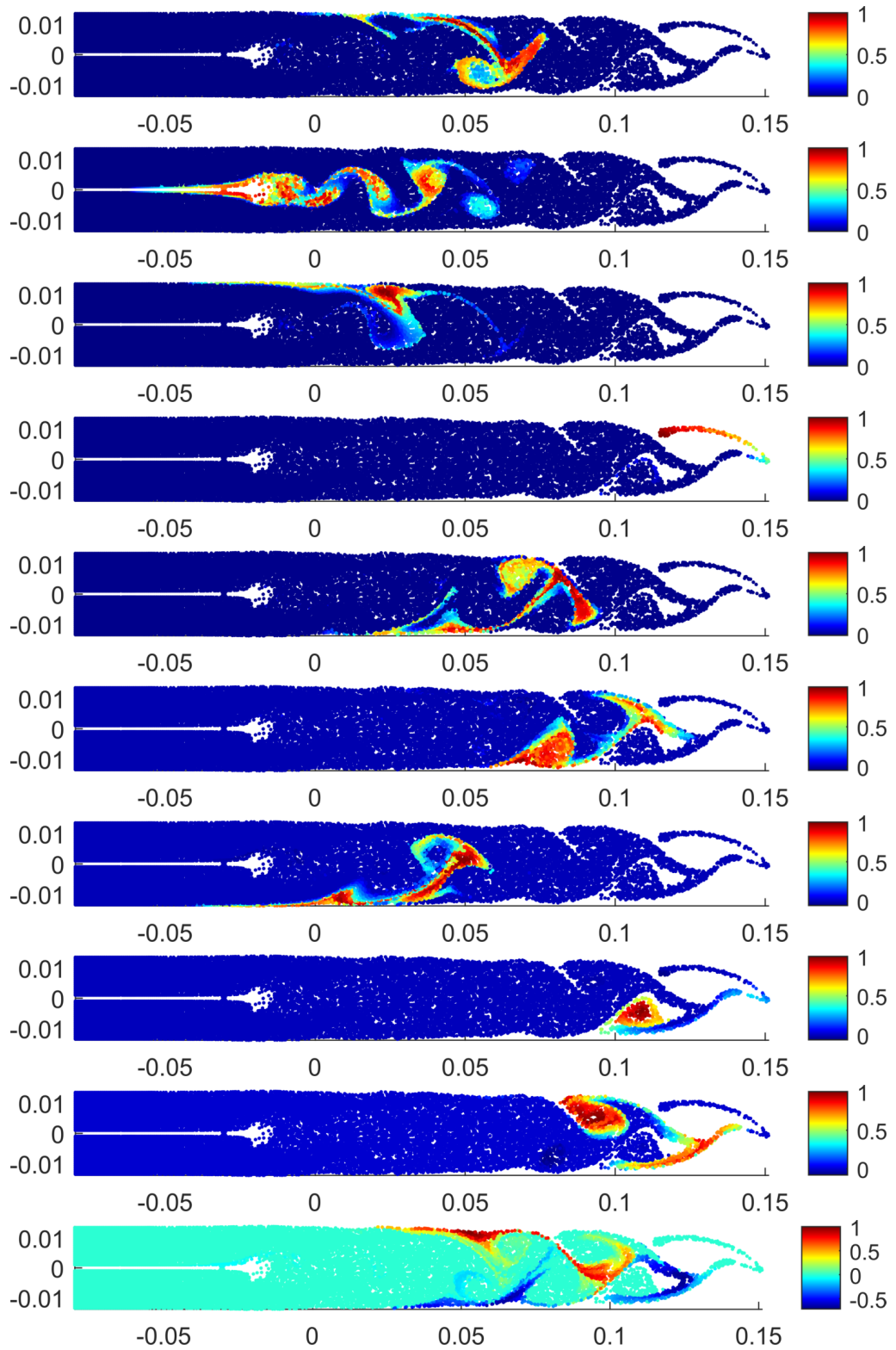


Figure 8.15.: Output sparse vectors obtained by SEBA applied to the first 10 eigenvectors of \bar{Q} , shown at the final time slice.

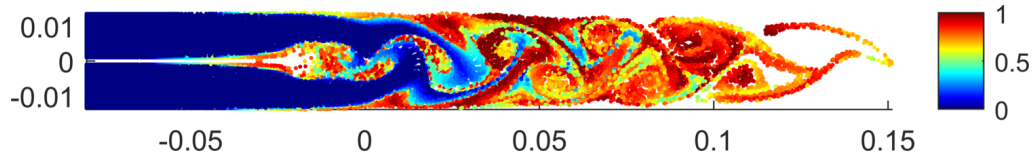


Figure 8.16.: Superposition of the vectors obtained by SEBA using \bar{Q} , shown at the final time slice.

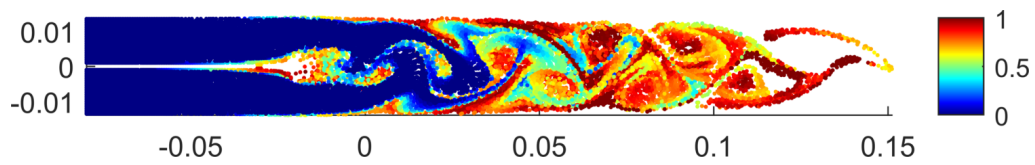


Figure 8.17.: Superposition of the vectors obtained by SEBA using \bar{Q}_s , shown at the final time slice.

Chapter 9.

Conclusion

In this thesis, we first considered transport and mixing in closed systems, and then in (double) open systems within a set-oriented transfer operator approach. In the mixing studies, we focused on the mixing of two types of fluids. Finally, we extended a recent trajectory-based approach.

Within the transfer operator approach, we considered the influence of a constant perturbation (wind) on coherent structures in the closed double gyre flow on a periodic domain. We observed a change in position, shape and size using only one wind direction. For small wind factors and some structures, these changes might be relatively small. Depending on the specific application, it can be crucial to take into account plausible wind factors.

We applied the numerical transfer operator framework for analyzing coherent behavior in nonautonomous systems to a (closed) two-dimensional Rayleigh-Bénard convection system. We reliably identified the gyre cores and the results compared well with those using trajectory-based methods in [62]. Whereas the dominant features can be extracted also when using less boxes and test points for the approximation of the transfer operator, the results of the FTE fields and the SEBA algorithm show more details of the dynamics in the background flow when more test points are used. In [63] we applied the transfer operator approach also to a RBC system in a three dimensional setting, and demonstrated thus the applicability to more complex systems. However, in turbulent systems coherent sets will exist only for a relatively short time span and the standard transfer operator approach will not be able to find any coherent sets when the time span is too long. Recent approaches as evolutionary clustering [106] and a novel inflated dynamic Laplacian operator construction [107] aim to overcome these issues.

The main contribution is the work on (double) open flows. We proposed a transfer operator framework to model and study the transport and mixing in specific open flows that can be seen as idealized open flow mixers.

We described the mixing of two types of fluids in both closed and open systems within the transfer operator framework. We computed finite-time mixing patterns for the closed double gyre flow and the RBC system, and invariant mixing patterns for different parameters the two double open systems, the double gyre mixer and the more realistic lid-driven cavity mixer. For the quantification of finite-time mixing of two different fluids in the closed systems and quantification of the invariant mixing patterns in the outlet region of double open systems, we applied several frequently used mixing measures, such as sample variance, mean

length scale, and a multiscale mix-norm.

The sample variance and mix-norm give consistent results. However, the mix-norm appears to be most robust with respect to numerical parameters (such as number of boxes and test particles). The computation of the mix-norm assumes a periodic domain of a torus. The quantification of mixing based on a mix-norm on arbitrary domains was recently considered in [108]. The use of the mean length scale showed problems to identify differences in the mixing patterns for the closed double gyre system at later times. An improvement of this mixing measure could be the use of concentration data instead of the box-discrete indicator variables. Also, as indicated in the open double gyre example, an increasing of the bin width can lead to a multi-scale mixing measure. The semivariogram can further be used to analyze mixing patterns in specific directions such as horizontal or vertical directions, which was not done here.

When considering mixing patterns of two different fluids in open systems after finite time the question arises, how one should deal with or quantify empty space in mixing patterns. With the transfer operator approach we can detect empty space in the patterns by following both fluids separately. It can then be considered how space-filling the two fluids are or how the two fluids are mixed on this structure.

In open systems, the chaotic saddle and its manifolds are known to organize the mixing processes. We demonstrated that the leading left and right eigenvectors or the self-communicating classes of the transition matrix can be used to approximate these structures. However, a direct relation between spectral properties of the substochastic transition matrix and the mixing properties of two fluids observed is not obvious, as there is no information of the source distribution in the transition matrix P . (Further, we cannot deduce the mixing quality in the double open system from the dominant spectrum of the corresponding closed system (see Appendix B). Hence, one has to study the open system.) The mixing patterns depend both on the underlying dynamics encoded in the transition matrix P and on the source distribution σ . In a parameter study, we studied the influence of the source distribution and give a first idea of a spectral mixing measure that takes two types of fluids into account. A next step would be to study if this heuristic mixing measure is reliable if the underlying stable manifolds change.

With regard to optimal mixing, it would be also interesting to extend recent transfer-operator based results on optimal initial tracer patterns in closed flows [60] to open flows and to combine the open-flow transfer operator framework with optimization schemes to maximize mixing, such as in [57].

With the channel with an obstacle we considered an example system with a realistic flow profile. This system also illustrates some restrictions/issues of the transfer operator approach, that is, it can be computational expensive to obtain an approximation of the transfer operator for a fine box-discretization for large domains. Also, the box-discretization itself becomes more challenging for domains that are not rectangular. Further, to model the transport in the double open channel, we had to extend the inlet region or we had to model the transport with a series of transition matrices (see Remark 6.2, 3. case).

In our examples, we restricted to periodic velocity fields (or assumed periodicity in the channel with an obstacle). For aperiodic flows, the mixing patterns restricted to the outlet region would be time-dependent (see Remark 6.2, 4. case) and could be studied using the different mixing measures. An extension of the transfer operator approach would be the extraction of the finite-time organizing structures within these specific open systems.

We considered here instead a trajectory-based approach, developed by [34], that is promising for the study of mixing processes in aperiodic open flow mixers, since it uses no information about the velocity fields.

We have modeled the mixing of two types of fluids using the diffusion map transition matrix. The results of the applied mixing measures to mixing patterns in periodic-forced double gyre flow within this approach are in agreement with the results within the transfer operator approach. Using an appropriate time-span, we could extract coherent sets in the double gyre mixer that revealed the stable and unstable manifolds of the chaotic saddles. In the channel with an obstacle we assumed no periodic velocity field and extracted a similar underlying structure as with the transfer operator approach together with further coherent sets.

We have defined coherent sets for fixed time intervals. However, in these open flow mixers, many trajectories leave the system soon and many trajectories enter the system at later times. These particles have in our construction a relatively low chance to be part of a coherent set. For the channel with an obstacle we aimed to extract time-averaged coherent sets. A further ansatz could be to use other weightings for these trajectories in the diffusion map transition matrix. It would be interesting to consider the approaches of using an evolutionary clustering or to allow coherent sets to arise and to die [106, 107].

In this thesis, we restricted our computational studies to two-dimensional example settings. The extension of both the transfer operator and trajectory-oriented approach to the three-dimensional setting is straightforward.

Appendix A.

SEBA

In both the transfer operator approach (Chapter 3) and the trajectory-based approach (Chapter 8), it is frequently the case that multiple almost-invariant sets or coherent sets are encoded in several dominant approximate eigenvectors or singular vectors.

In order to disentangle individual features, the SEBA (Sparse EigenBasis Approximation) algorithm [92] seeks a rotation of the vectors so that the rotated vectors span the same subspace and each rotated vector contains an individual feature.

In more detail, if each eigenvector or singular vector v_i , $i = 1, \dots, k$ is a column vector in \mathbb{R}^n and $V := [v_1|v_2|\dots|v_k]$ is an $n \times k$ array, we wish to find a sparse array $S = [s_1|s_2|\dots|s_k]$ for which $\text{span}\{s_1, s_2, \dots, s_k\} \approx \text{span}\{v_1, v_2, \dots, v_k\}$. Sparsity implies a small total feature support in each vector.

SEBA finds a locally optimal $k \times k$ rotation matrix R with $V \approx SR$ small and S sparse. See [92] for a precise description of the algorithm and further details.

When we have obtained s_1, \dots, s_k by SEBA, we interpret the j -th entry of s_i , $s_{i,j}$, as likelihood that (the box B_j or trajectory x^j) belongs to cluster i , when $s_{i,j} > 0$. When we combine the information in a superposition vector, an entry of this vector provides an indication of cluster membership certainty.

Appendix B.

Double gyre systems

Comparison of the different double gyre systems. We compute the transition matrices for the closed double gyre system without windage (denoted as \overline{P}_c), the double gyre system with windage parameter $\beta = 0.5$ on the periodic domain (denoted as \overline{P}_p) and the open double gyre system (denoted as P_o) on the domain $[0, 2] \times [0, 1]$ partitioned in 2^{16} boxes for time span $\tau = 1$ and different choices of ϵ .

In Figure B.1 are shown the leading second and third eigenvalues of \overline{P}_c and the real part of the second and third largest eigenvalues (sorted by real part) of \overline{P}_p . The first eigenvalues are 1, since the transition matrices are stochastic. Further are shown the real part of first and second largest eigenvalues of P_o (there are only small complex eigenvalues when there are no self-communicating classes).

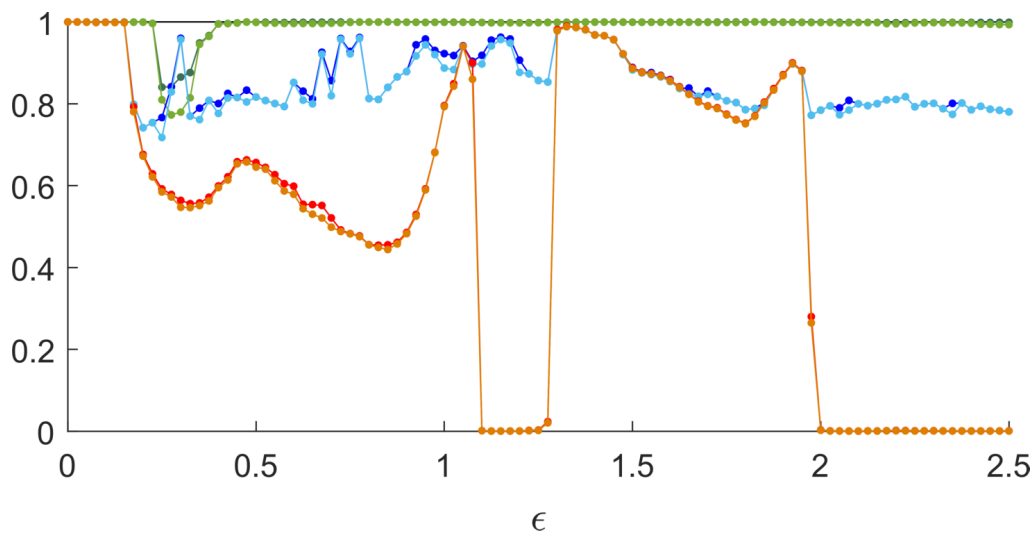


Figure B.1.: Comparison of the dominant eigenvalues in the different double gyre systems. Leading second (dark green) and third (green) largest eigenvalues of \overline{P}_c , real part of the second (dark blue) and third (blue) largest eigenvalues of \overline{P}_p , and real part of first (red) and second (orange) largest eigenvalues of P_o .

For small ϵ all shown eigenvalues are close to 1. For the closed system, only in a region around $\epsilon = 0.3$ the eigenvalues are noticeably lower. It becomes clear that

it is not enough to consider the leading eigenvalues of \overline{P}_c to know how windage (as in the system on the periodic domain or the open system) would effect the system.

Only for a few regions of ϵ the dominant eigenvalues of \overline{P}_p and P_o are in agreement, indicating similar dominant structures. In general the (real part of the) eigenvalues of \overline{P}_p are larger. Some of this eigenvalues are complex with nonzero imaginary part, indicating almost-cyclic structures that dominates the dynamics. But for some ϵ they are also real, indicating an almost-invariant structure that exist because of the periodic domain.

Box-counting dimension. A fractal dimension, the so-called *box-counting dimension*, of a structure U is defined by

$$D = \lim_{\delta \rightarrow 0} \frac{\log N_\delta(U)}{\log \frac{1}{\delta}},$$

where $N_\delta(U)$ is the smallest number of boxes of a diameter δ which can cover U . A one-dimensional curve has box-counting dimension 1 and a surface has box-counting dimension 2. For a chaotic saddle and its stable and unstable manifolds the box-counting dimensions are in generally not an integer, and it holds $1 < D \leq 2$ (see in [7,37] for a review on the box-counting dimension in the context of open flow mixing).

In a set-oriented framework, Siegmund and Taraba [109] used the subdivision algorithm [13] to approximate the box-counting dimension of attractors. Because of the transience in our open setting and the non-attractiveness of our phase-space structures, we can not use this subdivision algorithm to obtain approximations of the structures. However, based on these ideas we compute coarse approximations of the box-counting dimension of structures as chaotic saddles, their manifolds or almost-invariant sets.

Therefore, we use the already computed boxes in the supports of the leading eigenvectors or self-communicating classes of P as covering of a structure U . Since we use GAIO [87] for our computations, we also have a covering of the structure U using squared boxes with side length twice the size. We approximate the box-counting dimension of U by

$$\hat{D} = \frac{\log N_r - \log N_{2r}}{\log 2},$$

where N_r denote the number of boxes in the covering of the structure U using squared boxes with radius r and N_{2r} denote the number of the boxes in the covering of U using squared boxes with radius $2r$.

Figure B.2 presents the approximated box-counting dimensions for the extracted self-communicating classes in the double gyre system for different ϵ .

An idea to obtain stepwise finer approximations could be to subdivide the boxes in the support of leading left and right eigenvectors and calculate again the transition matrix only on these boxes.

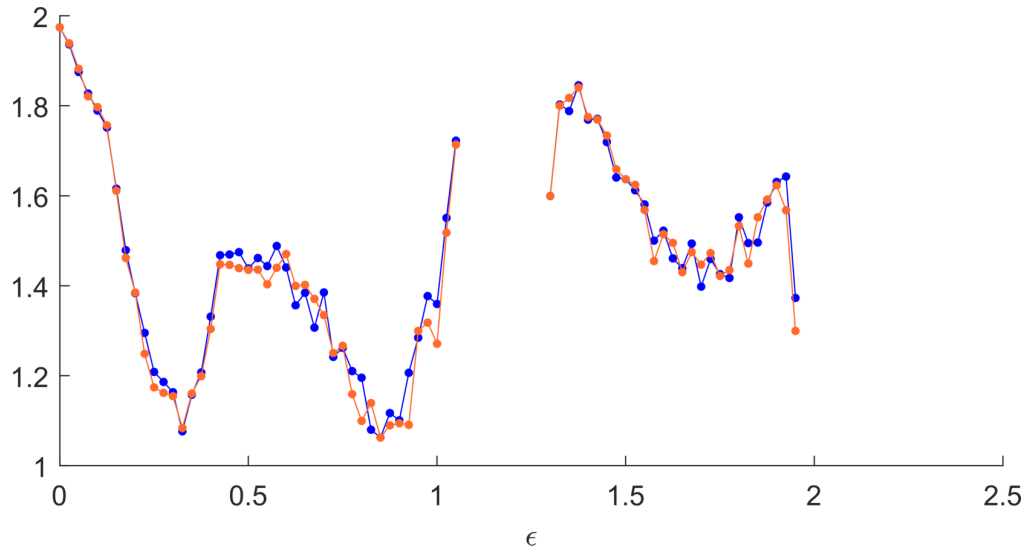


Figure B.2.: Rough approximations of the box-counting dimensions of the extracted self-communicating class on the left of the mixing region (blue) and of the self-communicating class on the right of the mixing region (orange) in the double gyre mixer with different choices of ϵ .

Expected residence times.

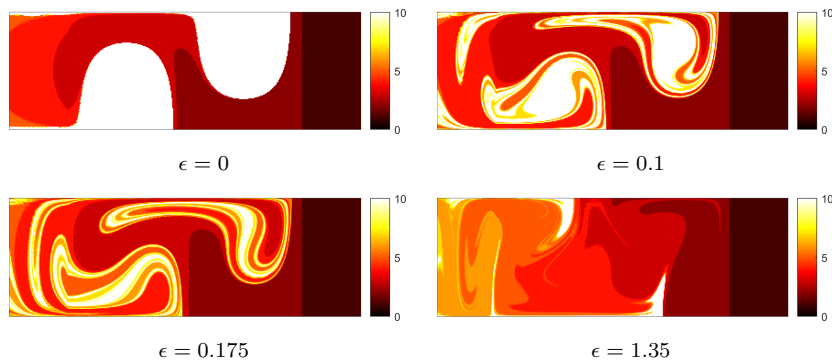


Figure B.3.: Expected residence times (smaller than 10) for different choices of ϵ . Expected residence times higher than 10 are shown in white.

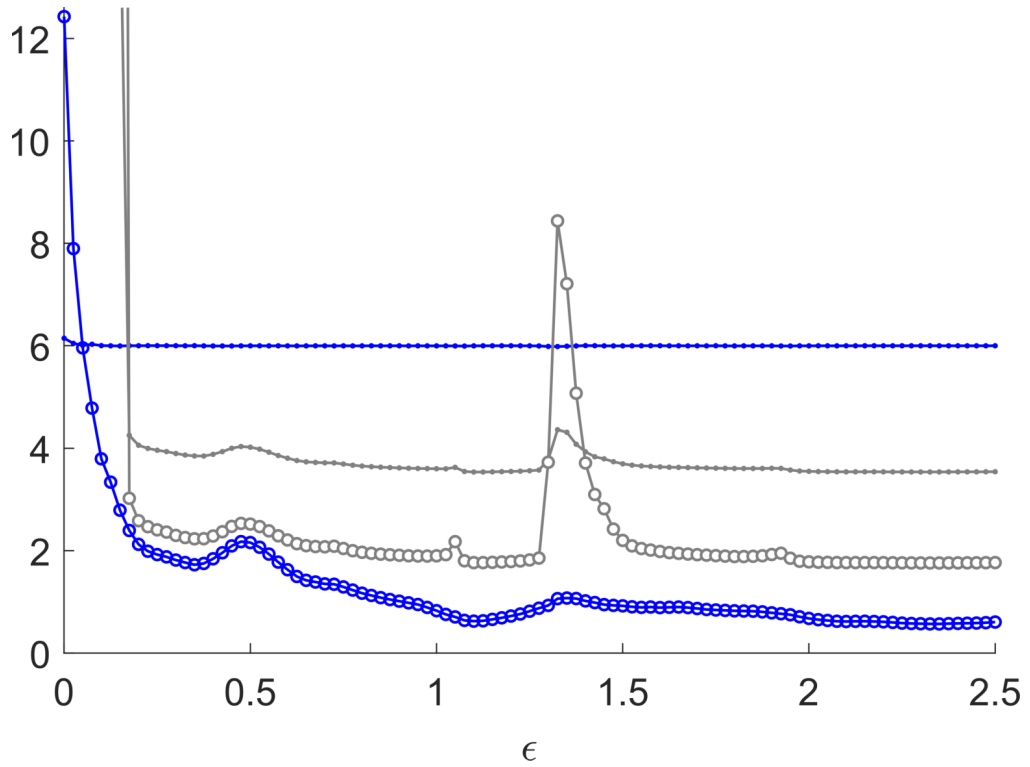


Figure B.4.: Means (dots) and standard deviations (circles) of the expected residence times in the double gyre mixer with different choices of ϵ . Blue are the statistics for boxes in the inlet region and gray are the statistics for all boxes. The y-axis is cutted at 12. For small ϵ , the statistics for all boxes are much higher, since there are relatively large almost-invariant sets.

Appendix C.

RBC

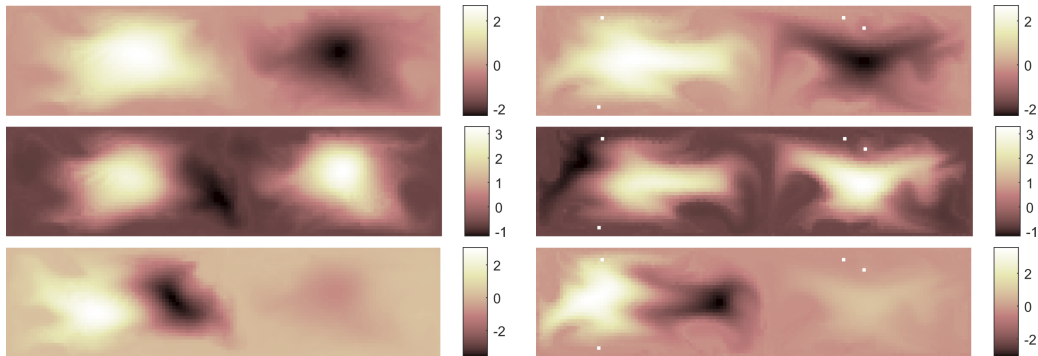


Figure C.1.: Left singular vectors ψ_2, ψ_3, ψ_4 of the modified transition matrix L and corresponding right singular vectors $\varphi_2, \varphi_3, \varphi_4$ (right column). Here the short time interval $[2000, 2020]$ and 2^{12} boxes are used for setting up \bar{P} .

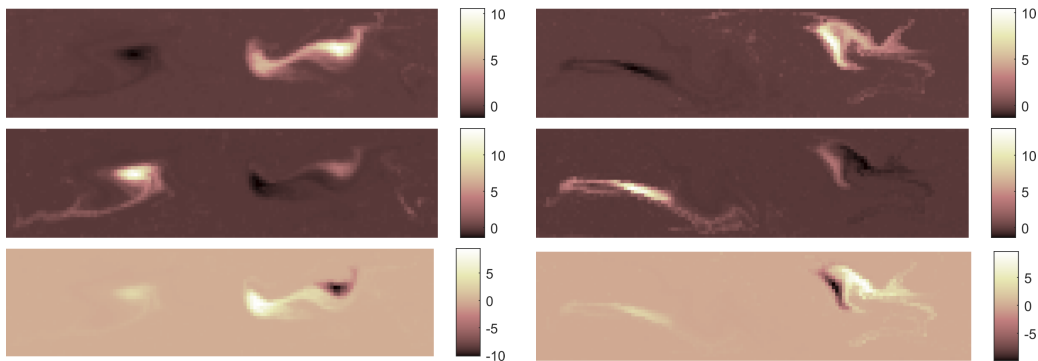


Figure C.2.: Left singular vectors ψ_2, ψ_3, ψ_4 of the modified transition matrix L and corresponding right singular vectors $\varphi_2, \varphi_3, \varphi_4$ (right column). Here the long time interval $[2000, 2200]$ and 2^{12} boxes are used for setting up \bar{P} .

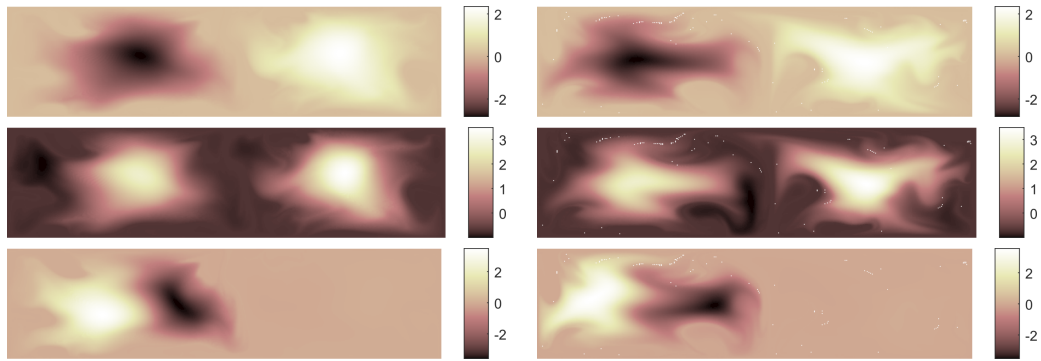


Figure C.3.: Left singular vectors ψ_2, ψ_3, ψ_4 of the modified transition matrix L and corresponding right singular vectors $\varphi_2, \varphi_3, \varphi_4$ (right column). Here the short time interval $[2000, 2020]$, 2^{16} boxes and 16 test points per box are used for setting up \bar{P} .

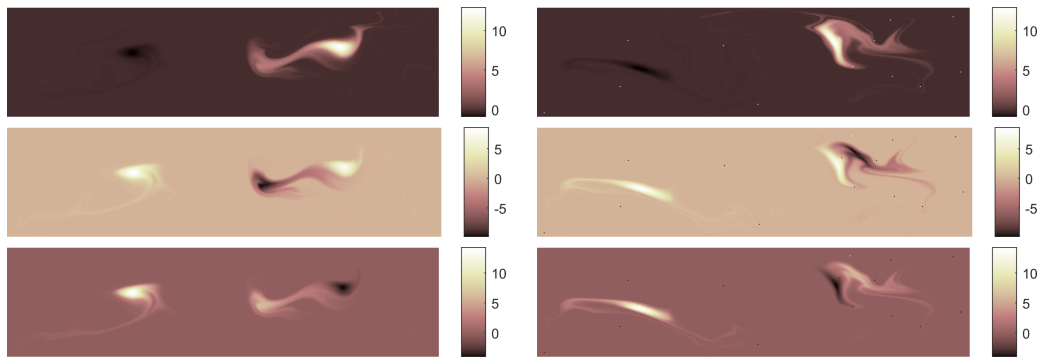


Figure C.4.: Left singular vectors ψ_2, ψ_3, ψ_4 of the modified transition matrix L and corresponding right singular vectors $\varphi_2, \varphi_3, \varphi_4$ (right column). Here the long time interval $[2000, 2200]$, 2^{16} boxes and 16 test points per box are used for setting up \bar{P} .

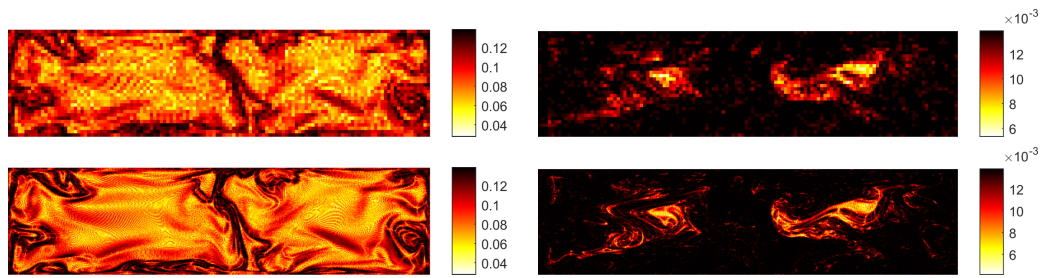


Figure C.5.: Forward time FTE fields computed over the short time interval [2000, 2020] (left column) and the long time interval [2000, 2200] (right column). The first row show these using 2^{12} boxes and the second rows show these using 2^{16} boxes and 16 test points per box.



Figure C.6.: Extracted coherent sets at initial time (left column) and final time (right column) via an application of the standard k -means algorithm. The first two rows show these for the short time interval and long time interval using 2^{12} boxes. The last two rows show these using 2^{16} boxes and 16 test points per box.

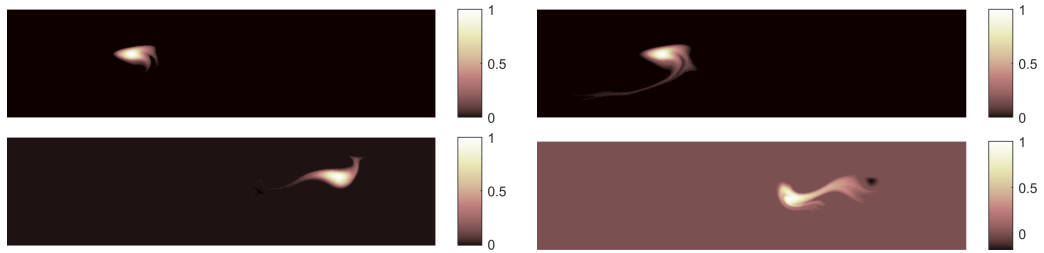


Figure C.7.: Output sparse vectors obtained by SEBA applied to the first four left singular vectors, 2^{16} boxes and 16 test points per box, time interval $[2000, 2200]$.

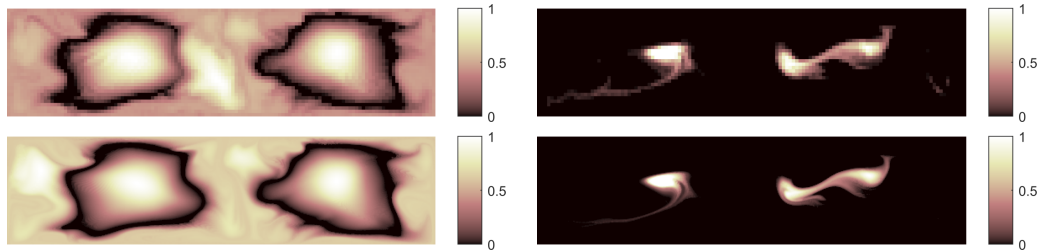


Figure C.8.: Superpositions of the output sparse vectors obtained by SEBA applied to the first three left singular vectors for time interval $[2000, 2020]$ (left column) and to the first four left singular vectors for time interval $[2000, 2200]$ (right column). The first row show these using 2^{12} boxes and the second row show these using 2^{16} boxes and 16 test points per box.

Table C.1.: Sample variance s^2 , mix-norm ϕ^2 (relative mixnorm ϕ_{rel}^2) and mean length scale \hat{L} in the RBC system after $\tau = 20 t_f, 200 t_f$.

# boxes, test points	\mathbf{v}_0	s^2	$\phi^2(\phi_{\text{rel}}^2)$	\hat{L}
$2^{12}, 16$	horizontal	1.0428, 0.2897	0.0854 (0.6372), 0.0066 (0.0491)	0.4523, 0.0769
	vertical	0.9717, 0.3649	0.0972 (0.7246), 0.0199 (0.1481)	0.4218, 0.0892
$2^{16}, 16$	horizontal	1.1358, 0.3989	0.0873 (0.6507), 0.0065 (0.0484)	0.2450, 0.0221
	vertical	1.0533, 0.4299	0.0986 (0.7357), 0.0197 (0.1472)	0.2047, 0.0236
$2^{16}, 100$	horizontal	0.9745, 0.2787	0.0870 (0.6488), 0.0063 (0.0468)	0.2904, 0.0283
	vertical	0.9519, 0.3102	0.0986 (0.7351), 0.0196 (0.1465)	0.2435, 0.0297

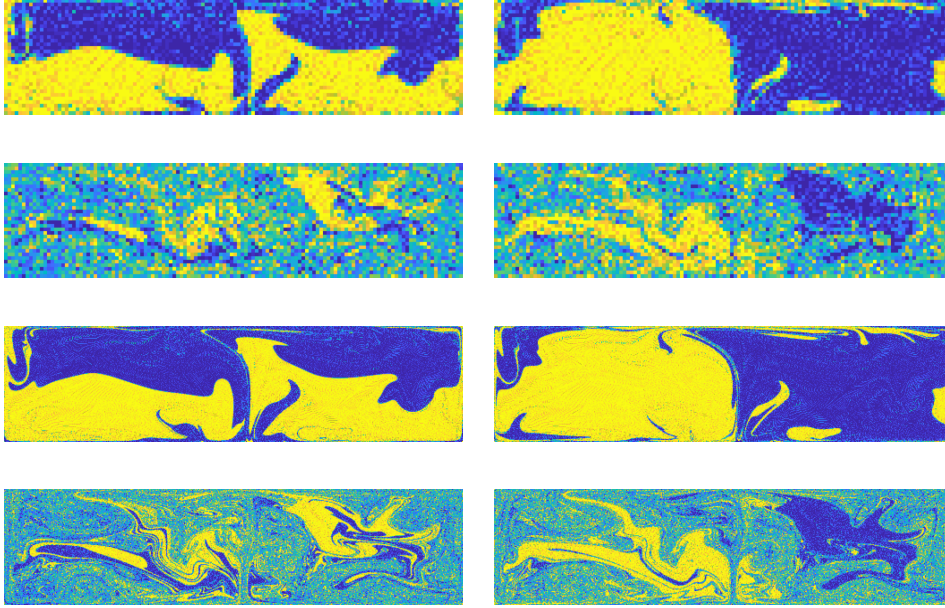


Figure C.9.: Evolved signed mass distributions – horizontally placed (left column) and vertically placed (right column) – in the RBC system. The first two rows show the mass distributions after the short and long time span using 2^{12} boxes and the last two rows show these using 2^{16} boxes and 16 test points per box.

List of figures

2.1.	One iteration of the Smale’s horseshoe map contracts the square (left), expands it, folds it around into the shape of a horseshoe and places it back on itself (right).	11
2.2.	State-transition diagram (restricted to transient states) of an absorbing Markov chain with two self-communicating classes. . . .	20
4.1.	Signed mass distributions on a discretized domain.	36
5.1.	Streamlines of the double gyre flow with $\alpha = 0.5$ and $\epsilon = 0.4$ at $t = 0$ (left) and $t = 0.25$ (right).	40
5.2.	Left: Leading 10 eigenvalues of R for time span $\tau = 1$. Right: Leading 10 singular values of L for time span $\tau = 4.5$. Blue: $\epsilon = 0.1$, orange: $\epsilon = 0.2$, cyan: $\epsilon = 0.3$, red: $\epsilon = 0.4$. Dots: $\beta = 0$, circles: $\beta = 0.1$, stars: $\beta = 0.3$, squares: $\beta = 0.4$ crosses: $\beta = 0.5$	42
5.3.	Second eigenvectors of the time-symmetrized transition matrix R in the double gyre system with windage for time span $\tau = 1$ and different parameters of ϵ and β	42
5.4.	Third eigenvectors of the time-symmetrized transition matrix R in the double gyre system with windage for time span $\tau = 1$ and different parameters of ϵ and β	43
5.5.	Extraction of 3 clusters by using a k -means clustering on the leading eigenvectors of the time-symmetrized transition matrix R in the double gyre system with windage for time span $\tau = 1$ and different parameters of ϵ and β	43
5.6.	Left: We consider the cyan colored almost-invariant set extracted for $\beta = 0$ and show the coherence ratios of this set in the systems with windage parameter $\beta = 0, 0.1, 0.3, 0.4$. Right: We consider the cyan colored coherent pair extracted for $\beta = 0$ and show the coherence ratio of this pair in the system with windage. Blue: $\epsilon = 0.1$, orange: $\epsilon = 0.2$, cyan: $\epsilon = 0.3$, red: $\epsilon = 0.4$	45
5.7.	Second left singular vectors of L in the double gyre system with windage for time span $\tau = 4.5$ and different parameters of ϵ and β	45
5.8.	Third left singular vectors of L in the double gyre system with windage for time span $\tau = 4.5$ and different parameters of ϵ and β	46
5.9.	Second right singular vectors of L in the double gyre system with windage for time span $\tau = 4.5$ and different parameters of ϵ and β	46
5.10.	Third right singular vectors of L in the double gyre system with windage for time span $\tau = 4.5$ and different parameters of ϵ and β	46

5.11. Extraction of 3 clusters by using a k -means clustering on the leading left singular vectors of L in the double gyre system with windage for time span $\tau = 4.5$ and different parameters of ϵ and β .	47
5.12. Extraction of 3 clusters by using a k -means clustering on the leading right singular vectors of L in the double gyre system with windage for time span $\tau = 4.5$ and different parameters of ϵ and β .	47
5.13. Image of the indicator vector of the cyan colored coherent set extracted for $\beta = 0$ in the systems with windage parameter $\beta = 0, 0.1, 0.3, 0.4$.	48
5.14. Evolution of the mass distribution \mathbf{v}_k (vertical and horizontal) for the closed double gyre mixer with parameters $\alpha = 0.5$ and different choices of ϵ .	50
5.15. $FTE(\cdot, 1)$ and $FTE(\cdot, 5)$ fields in backward time for $\epsilon = 0.2$	51
5.16. Mixing measures applied to \mathbf{v}_k . Left: Sample variance. Middle: Relative mix-norm. Right: Mean length scale. Blue: $\epsilon = 0.2$, red: $\epsilon = 0.3$, green: $\epsilon = 0.4$. Circles: vertically placed initial distribution, dots: horizontally placed initial distribution.	51
5.17. Instantaneous velocity field of the RBC system, changed from [62]. Hot temperatures are colored in red and cool temperature are colored in blue.	52
5.18. Forward time FTE field for 2^{16} boxes (top left) and FTLE field (bottom left) computed over the short time interval [2000, 2020]. Forward time FTE field for 2^{16} boxes and 100 test points per box (top right) and FTLE field (bottom right) computed over the long time interval [2000, 2200]. Dark regions are characterized by large stretching and correspond to dominant transport barriers.	54
5.19. Leading 12 singular values of the modified transition matrix calculated over the short time interval (left) and long time interval (right) for 2^{16} boxes and 100 test points per box (stars), 2^{16} boxes and 16 test points per box (filled dots) and 2^{12} boxes and 16 test points per box (circles).	55
5.20. Left singular vectors ψ_2, ψ_3, ψ_4 of the modified transition matrix L and corresponding right singular vectors $\varphi_2, \varphi_3, \varphi_4$ (right column). Here the short time interval [2000, 2020], 2^{16} boxes and 100 test points per box are used for setting up the transition matrix.	55
5.21. Extracted coherent sets at initial time (left) and final time (right) for the short time interval [2000, 2020] via an application of the standard k -means algorithm on the first three left singular vectors respective first three right singular vectors. Here 2^{16} boxes and 100 test points per box are used.	56
5.22. SEBA applied to the first three left singular vectors, 2^{16} boxes and 100 test points per box, time interval [2000, 2020]. The upper row shows two of the output sparse vectors. Lower left shows the third output sparse vector and lower right shows the superposition of the three sparse vectors, revealing an incoherent region in black.	56

5.23.	Left singular vectors ψ_2, ψ_3, ψ_4 of the modified transition matrix L and corresponding right singular vectors $\varphi_2, \varphi_3, \varphi_4$ (right column). Here the long time interval [2000, 2200] and 2^{16} boxes and 100 test points per box are used for setting up the transition matrix.	57
5.24.	Extracted coherent sets at initial time (left) and final time (right) for the long time interval [2000, 2200] via an application of the standard k -means algorithm on the first three left singular vectors respective first three right singular vectors. Here 2^{16} boxes and 100 test points per box are used.	57
5.25.	SEBA applied to the first four left singular vectors, 2^{16} boxes and 100 test points per box, time interval [2000, 2200]. The first and second row show the four output sparse vectors. The third row the superposition of the four sparse vectors.	57
5.26.	Evolution of two signed mass distributions in the RBC system.	59
5.27.	FTE fields in backward time computed for the short time interval [2000, 2020] and long time interval [2000, 2200].	59
6.1.	Schematic representation of the dynamics on an infinite strip X that is divided into an unmixed region X_1 , a mixing region X_2 and an mixed region X_3	61
7.1.	Setup of the double gyre mixer.	71
7.2.	Evolution of the mass distribution \mathbf{v}_k for the double gyre mixer with parameters $\alpha = 0.5, \epsilon = 0.4$ and $\beta = 0.5$	72
7.3.	Evolution of a set of particles for the double gyre mixer on the unbounded domain X with system parameters $\alpha = 0.5, \epsilon = 0.4$ and $\beta = 0.5$. Position of the particles after 0, 1, 2, 3, 4, 5, 6, 7, 8 time steps. Particles that stay longer in the mixing region (red) reveal the stable and unstable manifolds.	73
7.4.	Evolution of a set of particles for the double gyre mixer on the unbounded domain X with system parameters $\alpha = 0.5, \epsilon = 0.35$ and $\beta = 0.5$. Position of the particles after 0 and 8 time steps. Particles that stay longer in the mixing region (red) reveal the stable and unstable manifolds.	74
7.5.	Self-communicating classes of P for the double gyre mixer with system parameters $\alpha = 0.5, \epsilon = 0.4$, and $\beta = 0.5$ (a) and with system parameters $\alpha = 0.5, \epsilon = 0.35$, and $\beta = 0.5$ (b). There are two self-communicating classes: Boxes that belong to the first self-communicating class are colored in blue and boxes that belong to the second second are colored in orange.	75
7.6.	Double gyre mixer with system parameters $\alpha = 0.5, \epsilon = 0.4$, and $\beta = 0.5$. First left eigenvector \mathbf{w}_1 (a), first right eigenvector $\hat{\mathbf{w}}_1$ (b), second left eigenvector \mathbf{w}_2 (d) and second right eigenvector $\hat{\mathbf{w}}_2$ (e) of P . The support of these left and right eigenvectors (c), (f), where entries $< 10^{-12}$ are treated as zero. The intersection (dark blue, orange) approximates each a chaotic saddle.	75

7.7.	Double gyre mixer with system parameters $\alpha = 0.5$, $\epsilon = 0.35$, and $\beta = 0.5$. First left eigenvector \mathbf{w}_1 (a), first right eigenvector $\hat{\mathbf{w}}_1$ (b), second left eigenvector \mathbf{w}_2 (d) and second right (signed) eigenvector $\hat{\mathbf{w}}_2$ (e) of P . The support of these left and right eigenvectors (c), (f), where entries $< 10^{-12}$ are treated as zero. The intersection (dark blue, orange) approximates each a chaotic saddle.	76
7.8.	Double gyre mixer with system parameters $\alpha = 0.5$, $\epsilon = 0.4$ and $\beta = 0.5$. Expected residence times $E(T \cdot)$ in forward (left) and backward time (right).	76
7.9.	Number of self-communicating classes in the double gyre mixer with different choices of ϵ .	77
7.10.	The real parts of the first and second eigenvalues of the transition matrix P for the double gyre mixer with different choices of ϵ ; and a selection of extracted self-communicating classes.	77
7.11.	Expected residence times for different choices of ϵ .	78
7.12.	\mathbf{v}_{inv} (top) and $E(T \cdot)$ in backward time, shown in A_3 , for the double gyre mixer for different choices of ϵ . $\alpha = 0.5$ and $\beta = 0.5$ are fixed.	79
7.13.	Different measures of mixing applied to \mathbf{v}_{inv} restricted to A_3 for the double gyre mixer for different choices of ϵ . $\alpha = 0.5$ and $\beta = 0.5$ are fixed. Crosses: sample variance, circles: relative mix-norm, dots: mean length scale using $\delta = 0.0095$ (dashed line) and $\delta = 0.0051$ (solid line).	80
7.14.	Right eigenvectors $\hat{\mathbf{w}}_1$ (left) and $\hat{\mathbf{w}}_2$ (middle) restricted to the inlet region and the residence times field in backward time restricted to the outlet region (right).	81
7.15.	Source distributions for $\alpha = 0, 1, 1.8, 2.5$ and the respective invariant mass distribution on the outlet region.	82
7.16.	Left: sample variance (red) and relative mix-norm (blue). Right: $ (\hat{\mathbf{w}}_1 + \hat{\mathbf{w}}_2)^T \boldsymbol{\sigma}(\alpha) + (\hat{\mathbf{w}}_1 - \hat{\mathbf{w}}_2)^T \boldsymbol{\sigma}(\alpha) $.	83
7.17.	Streamlines of the lid-driven cavity flow with $U_1 = 9$ and $U_2 = 8$ at $t = 0$ (left) and $t = 0.5$ (right).	83
7.18.	Evolution of the mass distribution $\mathbf{v}_k, k = 1, 2, 3, \dots, 12$, for the lid-driven cavity mixer with system parameters $U_1 = 9, U_2 = 8$ and $\beta = 1$.	84
7.19.	Lid-driven cavity mixer with system parameters $U_1 = 9, U_2 = 8$ and $\beta = 1$. First left eigenvector \mathbf{w}_1 (a), first right eigenvector $\hat{\mathbf{w}}_1$ (b) and the support of these eigenvectors, where entries $< 10^{-3}$ are treated as zero. The intersection (dark blue) approximates the chaotic saddle.	85
7.20.	Different measures of mixing applied to \mathbf{v}_{inv} restricted to A_3 for the lid-driven cavity mixer for different choices of U_2 . $U_1 = 9$ and $\beta = 1$ are fixed. Crosses: sample variance; dots: mean length scale using $\delta = 0.0163$ (dashed line) and $\delta = 0.0094$ (solid line); circles: relative mix-norm.	86
7.21.	Simplified 2D domain of the mixing valve with indicated velocity field for the first time slice.	86

7.22. Evolution of a signed mass distribution in the mixing valve. . . .	87
7.23. Extracted self-communicating classes in the mixing valve.	88
7.24. Right eigenvectors corresponding to $\lambda_1, \lambda_2, \lambda_3$ and λ_7	88
7.25. Left eigenvectors corresponding to $\lambda_1, \lambda_2, \lambda_3$ and λ_7	88
8.1. Particles plotted with coevolved color vector z_k (vertical) in the closed double gyre system with parameters $\alpha = 0.5, \epsilon = 0.2$ at different times k	93
8.2. Mixing Measures applied to the color vectors z_k (vertical) for the closed double gyre mixer with parameters $\alpha = 0.5, \epsilon = 0.2$. Sample variance (left). Relative mix-norm (middle). Mean length scale based measure (right).	94
8.3. Leading eigenvalues of Q_s for $\tau = 1$ (left) and $\tau = 5$ (right). . . .	95
8.4. Result of a k -means clustering for $\tau = 1$ on the first two (top left), four (top right), 6 (bottom left) and 12 eigenvectors (bottom right) of Q_s , shown at time slice $t = 0$	95
8.5. $\tau = 1$: Superpositions of the output vectors obtained by SEBA using two (top left), four (top right), 6 (bottom left) and 12 eigenvectors (bottom right) Q_s , shown at time slice $t = 0$	95
8.6. $\tau = 1$: Result of a k -means clustering and superposition of the output vectors obtained by SEBA using six eigenvectors of Q , when no new particles enter A , shown at time slice $t = 0$	96
8.7. $\tau = 5$. Results of a k -means clustering on the first two (left) and on the first six eigenvectors (right) of Q_s , shown at time slice $t = 0$. Bottom row:	96
8.8. $\tau = 5$. Top row: Output sparse vectors obtained by SEBA using the first two eigenvectors of Q_s , shown at timeslice $t = 0$. Bottom row: Superpositions of the output vectors obtained by SEBA using two (left) and six eigenvectors (right) of Q_s , shown at timeslice $t = 0$	96
8.9. $\tau = 5$. Left: Superposition of two vectors obtained by SEBA, shown at different time slices.	97
8.10. Particles with coevolved color vector by $Q(i)$ in the channel with an obstacle.	99
8.11. Particles with coevolved color vector by $Q(i)$ in the mixing valve. Here new particles enter the system.	100
8.12. Color vector z_5 computed by using $Q_s(i)$ in the mixing valve. . .	100
8.13. Leading 30 eigenvalues of $Q(i)$ (blue) $Q_s(i)$ (cyan), for $i = 1$ (dots), 2 (plus signs), 3 (circles), 4 (asterisks), 5 (crosses), and their corresponding average matrices \bar{Q} (purple) and \bar{Q}_s (green).	101
8.14. Output sparse vectors obtained by SEBA using \bar{Q} , shown at the initial time slice.	102
8.15. Output sparse vectors obtained by SEBA applied to the first 10 eigenvectors of \bar{Q} , shown at the final time slice.	103
8.16. Superposition of the vectors obtained by SEBA using \bar{Q} , shown at the final time slice.	104

8.17. Superposition of the vectors obtained by SEBA using \bar{Q}_s , shown at the final time slice.	104
B.1. Comparison of the dominant eigenvalues in the different double gyre systems. Leading second (dark green) and third (green) largest eigenvalues of \bar{P}_c , real part of the second (dark blue) and third (blue) largest eigenvalues of \bar{P}_p , and real part of first (red) and second (orange) largest eigenvalues of P_o	110
B.2. Rough approximations of the box-counting dimensions of the extracted self-communicating class on the left of the mixing region (blue) and of the self-communicating class on the right of the mixing region (orange) in the double gyre mixer with different choices of ϵ	112
B.3. Expected residence times (smaller than 10) for different choices of ϵ . Expected residence times higher than 10 are shown in white.	112
B.4. Means (dots) and standard deviations (circles) of the expected residence times in the double gyre mixer with different choices of ϵ . Blue are the statistics for boxes in the inlet region and gray are the statistics for all boxes. The y-axis is cutted at 12. For small ϵ , the statistics for all boxes are much higher, since there are relatively large almost-invariant sets.	113
C.1. Left singular vectors ψ_2, ψ_3, ψ_4 of the modified transition matrix L and corresponding right singular vectors $\varphi_2, \varphi_3, \varphi_4$ (right column). Here the short time interval [2000, 2020] and 2^{12} boxes are used for setting up \bar{P}	114
C.2. Left singular vectors ψ_2, ψ_3, ψ_4 of the modified transition matrix L and corresponding right singular vectors $\varphi_2, \varphi_3, \varphi_4$ (right column). Here the long time interval [2000, 2200] and 2^{12} boxes are used for setting up \bar{P}	114
C.3. Left singular vectors ψ_2, ψ_3, ψ_4 of the modified transition matrix L and corresponding right singular vectors $\varphi_2, \varphi_3, \varphi_4$ (right column). Here the short time interval [2000, 2020], 2^{16} boxes and 16 test points per box are used for setting up \bar{P}	115
C.4. Left singular vectors ψ_2, ψ_3, ψ_4 of the modified transition matrix L and corresponding right singular vectors $\varphi_2, \varphi_3, \varphi_4$ (right column). Here the long time interval [2000, 2200], 2^{16} boxes and 16 test points per box are used for setting up \bar{P}	115
C.5. Forward time FTE fields computed over the short time interval [2000, 2020] (left column) and the long time interval [2000, 2200] (right column). The first row show these using 2^{12} boxes and the second rows show these using 2^{16} boxes and 16 test points per box. 116	

C.6.	Extracted coherent sets at initial time (left column) and final time (right column) via an application of the standard k -means algorithm. The first two rows show these for the short time interval and long time interval using 2^{12} boxes. The last two rows show these using 2^{16} boxes and 16 test points per box.	116
C.7.	Output sparse vectors obtained by SEBA applied to the first four left singular vectors, 2^{16} boxes and 16 test points per box, time interval [2000, 2200].	117
C.8.	Superpositions of the output sparse vectors obtained by SEBA applied to the first three left singular vectors for time interval [2000, 2020] (left column) and to the first four left singular vectors for time interval [2000, 2200] (right column). The first row show these using 2^{12} boxes and the second row show these using show these using 2^{16} boxes and 16 test points per box.	117
C.9.	Evolved signed mass distributions – horizontally placed (left column) and vertically placed (right column) – in the RBC system. The first two rows show the mass distributions after the short and long time span using 2^{12} boxes and the last two rows show these using 2^{16} boxes and 16 test points per box.	118

Bibliography

- [1] E. Van Sebille, M. H. England, and G. Froyland, “Origin, dynamics and evolution of ocean garbage patches from observed surface drifters,” *Environmental Research Letters*, vol. 7, no. 4, p. 044040, 2012.
- [2] G. Froyland, R. M. Stuart, and E. van Sebille, “How well-connected is the surface of the global ocean?,” *Chaos: An Interdisciplinary Journal of Nonlinear Science*, vol. 24, no. 3, p. 033126, 2014.
- [3] P. Miron, F. Beron-Vera, L. Helfmann, and P. Koltai, “Transition paths of marine debris and the stability of the garbage patches,” *Chaos: An Interdisciplinary Journal of Nonlinear Science*, vol. 31, no. 3, p. 033101, 2021.
- [4] H. Aref, “Stirring by chaotic advection,” *J. Fluid Mech.*, vol. 143, pp. 1–21, 1984.
- [5] G. Mathew, L. Petzold, and R. Serban, “Computational techniques for quantification and optimization of mixing in microfluidic devices,” 2002.
- [6] M. F. Eggl and P. J. Schmid, “Mixing by stirring: Optimizing shapes and strategies,” *Physical Review Fluids*, vol. 7, no. 7, p. 073904, 2022.
- [7] H. Aref, J. R. Blake, M. Budišić, S. S. S. Cardoso, J. H. E. Cartwright, H. J. H. Clercx, K. El Omari, U. Feudel, R. Golestanian, E. Guillard, G. F. van Heijst, T. S. Krasnopolskaya, Y. Le Guer, R. S. MacKay, V. V. Meleshko, G. Metcalfe, I. Mezić, A. P. S. de Moura, O. Piro, M. F. M. Speetjens, R. Sturman, J.-L. Thiffeault, and I. Tuval, “Frontiers of chaotic advection,” *Rev. Mod. Phys.*, vol. 89, p. 025007, 2017.
- [8] S. Balasuriya, *Barriers and transport in unsteady flows: a Melnikov approach*. SIAM, 2016.
- [9] M. R. Allshouse and T. Peacock, “Lagrangian based methods for coherent structure detection,” *Chaos: An Interdisciplinary Journal of Nonlinear Science*, vol. 25, no. 9, p. 097617, 2015.
- [10] A. Hadjighasem, M. Farazmand, D. Blazeovski, G. Froyland, and G. Haller, “A critical comparison of Lagrangian methods for coherent structure detection,” *Chaos: An Interdisciplinary Journal of Nonlinear Science*, vol. 27, no. 5, p. 053104, 2017.

- [11] R. T. Pierrehumbert and H. Yang, “Global chaotic mixing on isentropic surfaces,” *Journal of the atmospheric sciences*, vol. 50, no. 15, pp. 2462–2480, 1993.
- [12] G. Haller, “Lagrangian coherent structures,” *Annu. Rev. Fluid Mech.*, vol. 47, no. 1, pp. 137–162, 2015.
- [13] M. Dellnitz and A. Hohmann, “A subdivision algorithm for the computation of unstable manifolds and global attractors,” *Numerische Mathematik*, vol. 75, no. 3, pp. 293–317, 1997.
- [14] M. Dellnitz and O. Junge, “Almost invariant sets in chua’s circuit,” *International Journal of Bifurcation and Chaos*, vol. 7, no. 11, pp. 2475–2485, 1997.
- [15] M. Dellnitz and O. Junge, “On the approximation of complicated dynamical behavior,” *SIAM Journal on Numerical Analysis*, vol. 36, no. 2, pp. 491–515, 1999.
- [16] G. Froyland, “Statistically optimal almost-invariant sets,” *Physica D: Nonlinear Phenomena*, vol. 200, no. 3-4, pp. 205–219, 2005.
- [17] G. Froyland and K. Padberg, “Almost-invariant sets and invariant manifolds – connecting probabilistic and geometric descriptions of coherent structures in flows,” *Physica D: Nonlinear Phenomena*, vol. 238, no. 16, pp. 1507–1523, 2009.
- [18] S. Ulam, “Problems in Modern Mathematics,” Interscience, 1964.
- [19] G. Froyland, S. Lloyd, and N. Santitissadeekorn, “Coherent sets for nonautonomous dynamical systems,” *Physica D: Nonlinear Phenomena*, vol. 239, no. 16, pp. 1527–1541, 2010.
- [20] G. Froyland, N. Santitissadeekorn, and A. Monahan, “Transport in time-dependent dynamical systems: Finite-time coherent sets,” *Chaos: An Interdisciplinary Journal of Nonlinear Science*, vol. 20, no. 4, p. 043116, 2010.
- [21] G. Froyland, “An analytic framework for identifying finite-time coherent sets in time-dependent dynamical systems,” *Physica D: Nonlinear Phenomena*, vol. 250, pp. 1–19, 2013.
- [22] G. Froyland and K. Padberg-Gehle, “Almost-invariant and finite-time coherent sets: directionality, duration, and diffusion,” in *Ergodic Theory, Open Dynamics, and Coherent Structures*, pp. 171–216, Springer, 2014.
- [23] G. Froyland and K. Padberg-Gehle, “Finite-time entropy: A probabilistic approach for measuring nonlinear stretching,” *Physica D: Nonlinear Phenomena*, vol. 241, no. 19, pp. 1612–1628, 2012.

- [24] G. Froyland, K. Padberg, M. H. England, and A. M. Treguier, “Detection of coherent oceanic structures via transfer operators,” *Physical review letters*, vol. 98, no. 22, p. 224503, 2007.
- [25] M. Dellnitz, G. Froyland, C. Horenkamp, K. Padberg-Gehle, and A. Sen Gupta, “Seasonal variability of the subpolar gyres in the southern ocean: a numerical investigation based on transfer operators,” *Nonlinear Processes in Geophysics*, vol. 16, no. 6, pp. 655–663, 2009.
- [26] G. Froyland, C. Horenkamp, V. Rossi, N. Santitissadeekorn, and A. S. Gupta, “Three-dimensional characterization and tracking of an agulhas ring,” *Ocean Modelling*, vol. 52, pp. 69–75, 2012.
- [27] N. Santitissadeekorn, G. Froyland, and A. Monahan, “Optimally coherent sets in geophysical flows: A transfer-operator approach to delimiting the stratospheric polar vortex,” *Physical Review E*, vol. 82, no. 5, p. 056311, 2010.
- [28] G. Froyland, “Dynamic isoperimetry and the geometry of Lagrangian coherent structures,” *Nonlinearity*, vol. 28, no. 10, p. 3587, 2015.
- [29] G. Froyland and O. Junge, “Robust FEM-based extraction of finite-time coherent sets using scattered, sparse, and incomplete trajectories,” *SIAM Journal on Applied Dynamical Systems*, vol. 17, no. 2, pp. 1891–1924, 2018.
- [30] G. Froyland and K. Padberg-Gehle, “A rough-and-ready cluster-based approach for extracting finite-time coherent sets from sparse and incomplete trajectory data,” *Chaos: An Interdisciplinary Journal of Nonlinear Science*, vol. 25, no. 8, p. 087406, 2015.
- [31] A. Hadjighasem, D. Karrasch, H. Teramoto, and G. Haller, “Spectral-clustering approach to Lagrangian vortex detection,” *Physical Review E*, vol. 93, no. 6, p. 063107, 2016.
- [32] K. L. Schlueter-Kuck and J. O. Dabiri, “Coherent structure colouring: identification of coherent structures from sparse data using graph theory,” *Journal of Fluid Mechanics*, vol. 811, pp. 468–486, 2017.
- [33] K. Padberg-Gehle and C. Schneide, “Network-based study of Lagrangian transport and mixing,” *Nonlinear Processes in Geophysics*, vol. 24, no. 4, pp. 661–671, 2017.
- [34] R. Banisch and P. Koltai, “Understanding the geometry of transport: diffusion maps for Lagrangian trajectory data unravel coherent sets,” *Chaos: An Interdisciplinary Journal of Nonlinear Science*, vol. 27, no. 3, p. 035804, 2017.
- [35] G. Froyland and O. Stancevic, “Escape rates and Perron-Frobenius operators: Open and closed dynamical systems,” *Discrete Contin. Dyn. Syst. Ser. B*, vol. 14, no. 2, pp. 457–472, 2010.

- [36] G. Froyland, P. K. Pollett, and R. M. Stuart, “A closing scheme for finding almost-invariant sets in open dynamical systems,” *J. Comput. Dynamics*, vol. 1, pp. 135–162, 2014.
- [37] A. Moura, U. Feudel, and E. Gouillart, “Mixing and chaos in open flows,” vol. 45 of *Advances in Applied Mechanics*, pp. 1 – 50, Elsevier, 2012.
- [38] C. Jung, T. Tél, and E. Ziemniak, “Application of scattering chaos to particle transport in a hydrodynamical flow,” *Chaos: An Interdisciplinary Journal of Nonlinear Science*, vol. 3, no. 4, pp. 555–568, 1993.
- [39] Z. Neufeld and T. Tél, “Advection in chaotically time-dependent open flows,” *Physical Review E*, vol. 57, no. 3, pp. 2832–2842, 1998.
- [40] Y.-C. Lai and T. Tél, *Transient Chaos: Complex Dynamics on Finite Time Scales*. Springer, 2011.
- [41] P. V. Danckwerts, “The definition and measurement of some characteristics of mixtures,” *Applied Scientific Research, Section A*, vol. 3, no. 4, pp. 279–296, 1952.
- [42] G. Mathew, I. Mezić, and L. Petzold, “A multiscale measure for mixing,” *Physica D: Nonlinear Phenomena*, vol. 211, no. 1-2, pp. 23–46, 2005.
- [43] A. Kukukova, J. Aubin, and S. M. Kresta, “Measuring the scale of segregation in mixing data,” *The Canadian Journal of Chemical Engineering*, vol. 89, no. 5, pp. 1122–1138, 2011.
- [44] J.-L. Thiffeault, “Using multiscale norms to quantify mixing and transport,” *Nonlinearity*, vol. 25, no. 2, pp. R1–R44, 2012.
- [45] E. Gouillart, O. Dauchot, and J.-L. Thiffeault, “Measures of mixing quality in open flows with chaotic advection,” *Physics of Fluids*, vol. 23, no. 1, p. 013604, 2011.
- [46] R. Pierrehumbert, “Tracer microstructure in the large-eddy dominated regime,” *Chaos, Solitons & Fractals*, vol. 4, no. 6, pp. 1091 – 1110, 1994. Special Issue: Chaos Applied to Fluid Mixing.
- [47] D. Rothstein, E. Henry, and J. P. Gollub, “Persistent patterns in transient chaotic fluid mixing,” *Nature*, vol. 401, no. 6755, pp. 770–772, 1999.
- [48] G. A. Voth, T. C. Saint, G. Dobler, and J. P. Gollub, “Mixing rates and symmetry breaking in two-dimensional chaotic flow,” *Physics of Fluids*, vol. 15, no. 9, pp. 2560–2566, 2003.
- [49] W. Liu and G. Haller, “Strange eigenmodes and decay of variance in the mixing of diffusive tracers,” *Physica D*, vol. 188, pp. 1–39, 2004.
- [50] J.-L. Thiffeault, “The strange eigenmode in Lagrangian coordinates,” *Chaos: An Interdisciplinary Journal of Nonlinear Science*, vol. 14, no. 3, pp. 531–538, 2004.

- [51] P. H. Haynes and J. Vanneste, “What controls the decay of passive scalars in smooth flows?,” *Physics of Fluids*, vol. 17, p. 097103, 2005.
- [52] E. Gouillart, O. Dauchot, J.-L. Thiffeault, and S. Roux, “Open-flow mixing: Experimental evidence for strange eigenmodes,” *Physics of Fluids*, vol. 21, no. 2, p. 023603, 2009.
- [53] G. Mathew, I. Mezić, S. Grivopoulos, U. Vaidya, and L. Petzold, “Optimal control of mixing in Stokes fluid flows,” *Journal of Fluid Mechanics*, vol. 580, pp. 261–281, 2007.
- [54] Z. Lin, J.-L. Thiffeault, and C. R. Doering, “Optimal stirring strategies for passive scalar mixing,” *Journal of Fluid Mechanics*, vol. 675, pp. 465–476, 2011.
- [55] S. Ober-Blöbaum and K. Padberg-Gehle, “Multi-objective optimal control of fluid mixing,” *Proceedings in Applied Mathematics and Mechanics*, vol. 15, pp. 639–640, 2015.
- [56] M. F. Eggl and P. J. Schmid, “Mixing enhancement in binary fluids using optimised stirring strategies,” *Journal of Fluid Mechanics*, vol. 899, 2020.
- [57] G. Froyland, C. González-Tokman, and T. Watson, “Optimal mixing enhancement by local perturbation,” *SIAM Review*, vol. 58, no. 3, pp. 494–513, 2016.
- [58] G. Froyland and N. Santitissadeekorn, “Optimal mixing enhancement,” *SIAM Journal on Applied Mathematics*, vol. 77, no. 4, pp. 1444–1470, 2017.
- [59] P. Grover and K. Elamvazhuthi, “Optimal perturbations for nonlinear systems using graph-based optimal transport,” *Communications in Nonlinear Science and Numerical Simulation*, vol. 59, pp. 197–215, 2018.
- [60] M. Farazmand, “Optimal initial condition of passive tracers for their maximal mixing in finite time,” *Phys. Rev. Fluids*, vol. 2, p. 054601, May 2017.
- [61] S. C. Shadden, F. Lekien, and J. E. Marsden, “Definition and properties of Lagrangian coherent structures from finite-time Lyapunov exponents in two-dimensional aperiodic flows,” *Physica D: Nonlinear Phenomena*, vol. 212, no. 3-4, pp. 271–304, 2005.
- [62] C. Schneide, M. Stahn, A. Pandey, O. Junge, P. Koltai, K. Padberg-Gehle, and J. Schumacher, “Lagrangian coherent sets in turbulent Rayleigh-Bénard convection,” *Physical Review E*, vol. 100, no. 5, p. 053103, 2019.
- [63] A. Klünker, C. Schneide, G. Froyland, J. Schumacher, and K. Padberg-Gehle, “Set-oriented and finite-element study of coherent behavior in Rayleigh-Bénard convection,” in *Advances in Dynamics, Optimization and Computation: A volume dedicated to Michael Dellnitz on the occasion of his 60th birthday*, pp. 86–108, Springer, 2020.

- [64] K. Ward and Z. H. Fun, “Mixing in microfluidic devices and enhancement methods,” *J. Micromech. Microeng.*, vol. 25, p. 094001, 2015.
- [65] E. Floriani, R. Lima, O. Ourrad, and L. Spinelli, “Flux through a Markov chain,” *Chaos, Solitons & Fractals*, vol. 93, pp. 136–146, 2016.
- [66] H. Berthiaux and V. Mizonov, “Applications of Markov chains in particulate process engineering: a review,” *The Canadian Journal of Chemical Engineering*, vol. 82, no. 6, pp. 1143–1168, 2004.
- [67] P. Grover, S. D. Ross, M. A. Stremler, and P. Kumar, “Topological chaos, braiding and bifurcation of almost-cyclic sets,” *Chaos: An Interdisciplinary Journal of Nonlinear Science*, vol. 22, no. 4, p. 043135, 2012.
- [68] A. Klünker, K. Padberg-Gehle, and J.-L. Thiffeault, “Open-flow mixing and transfer operators,” *Philosophical Transactions of the Royal Society A*, vol. 380, no. 2225, p. 20210028, 2022.
- [69] R. Neubauer, M. Reikat, and E. Steuwe, “Semester project in ‘Computational Fluid Dynamics in Process Engineering Lagrangian Transport in Turbulent Flows’.” Module held by M. Schlüter and A. von Kameke, Summer Semester 2021, TUHH; project task designed by R. Colombi and T. Frey.
- [70] A. Lasota and M. C. Mackey, *Chaos, fractals, and noise: stochastic aspects of dynamics*, vol. 97. New York: Springer, 1998.
- [71] J. Guckenheimer and P. Holmes, *Nonlinear oscillations, dynamical systems, and bifurcations of vector fields*, vol. 42. New York: Springer, 1983.
- [72] S. Wiggins, S. Wiggins, and M. Golubitsky, *Introduction to applied nonlinear dynamical systems and chaos*, vol. 2. Springer, 2003.
- [73] E. Seneta, *Non-negative matrices and Markov chains*. New York: Springer, 2 ed., 1981.
- [74] P. Collet, S. Martínez, and J. San Martín, “Quasi-stationary distributions,” *Markov chains, diffusions and dynamical systems*, 2013.
- [75] S. Smale, “Differentiable dynamical systems,” *Bulletin of the American mathematical Society*, vol. 73, no. 6, pp. 747–817, 1967.
- [76] Y.-C. Lai, C. Grebogi, J. Yorke, and I. Kan, “How often are chaotic saddles nonhyperbolic?,” *Nonlinearity*, vol. 6, no. 5, p. 779, 1993.
- [77] H. Crauel and P. E. Kloeden, “Nonautonomous and random attractors,” *Jahresbericht der Deutschen Mathematiker-Vereinigung*, vol. 117, no. 3, pp. 173–206, 2015.
- [78] C. M. Dafermos, “An invariance principle for compact processes,” *Journal of Differential Equations*, vol. 9, no. 2, pp. 239–252, 1971.

- [79] L. Arnold, “Random dynamical systems,” *Dynamical systems*, pp. 1–43, 1995.
- [80] G. Pianigiani and J. A. Yorke, “Expanding maps on sets which are almost invariant. decay and chaos,” *Transactions of the American Mathematical Society*, vol. 252, pp. 351–366, 1979.
- [81] M. F. Demers and L.-S. Young, “Escape rates and conditionally invariant measures,” *Nonlinearity*, vol. 19, no. 2, p. 377, 2005.
- [82] A. Mohapatra and W. Ott, “Memory loss for nonequilibrium open dynamical systems,” *Discrete & Continuous Dynamical Systems*, vol. 34, no. 9, p. 3747, 2014.
- [83] A. Lasota and M. C. Mackey, “Probabilistic Properties of Deterministic Systems,” Cambridge University Press, 1985.
- [84] E. A. van Doorn and P. K. Pollett, “Quasi-stationary distributions for reducible absorbing Markov chains in discrete time,” *Markov Process. Related Fields*, vol. 15, no. 2, pp. 191–204, 2009.
- [85] J. N. Darroch and E. Seneta, “On quasi-stationary distributions in absorbing discrete-time finite markov chains,” *Journal of Applied Probability*, vol. 2, no. 1, pp. 88–100, 1965.
- [86] C. M. Grinstead and J. L. Snell, *Introduction to probability*. American Mathematical Soc., 1997.
- [87] M. Dellnitz, G. Froyland, and O. Junge, “The algorithms behind GAIO - Set oriented numerical methods for dynamical systems,” in *Ergodic theory, analysis, and efficient simulation of dynamical systems*, pp. 145–174, Springer, 2001.
- [88] G. Froyland and M. Dellnitz, “Detecting and locating near-optimal almost-invariant sets and cycles,” *SIAM Journal on Scientific Computing*, vol. 24, no. 6, pp. 1839–1863, 2003.
- [89] M. Dellnitz and C. Horenkamp, “The efficient approximation of coherent pairs in non-autonomous dynamical systems,” *Discrete & Continuous Dynamical Systems*, vol. 32, no. 9, p. 3029, 2012.
- [90] R. Tarjan, “Depth-first search and linear graph algorithms,” *SIAM Journal on Computing*, vol. 1, no. 2, pp. 146–160, 1972.
- [91] S. Lloyd, “Least squares quantization in pcm,” *IEEE transactions on information theory*, vol. 28, no. 2, pp. 129–137, 1982.
- [92] G. Froyland, C. P. Rock, and K. Sakellariou, “Sparse eigenbasis approximation: Multiple feature extraction across spatiotemporal scales with application to coherent set identification,” *Communications in Nonlinear Science and Numerical Simulation*, vol. 77, pp. 81–107, 2019.

- [93] C. R. Doering and C. Nobili, “Lectures on stirring, mixing and transport,” in *Transport, Fluids, and Mixing* (G. Crippa and A. Mazzucato, eds.), pp. 8–34, Boston, USA: De Gruyter Open Poland, 2017.
- [94] A. Kukukova, J. Aubin, and S. M. Kresta, “A new definition of mixing and segregation: three dimensions of a key process variable,” *Chemical engineering research and design*, vol. 87, no. 4, pp. 633–647, 2009.
- [95] S. F. Carle and G. E. Fogg, “Transition probability-based indicator geostatistics,” *Mathematical geology*, vol. 28, no. 4, pp. 453–476, 1996.
- [96] K. R. Pratt, J. D. Meiss, and J. P. Crimaldi, “Reaction enhancement of initially distant scalars by Lagrangian coherent structures,” *Physics of Fluids*, vol. 27, no. 3, p. 035106, 2015.
- [97] K. Sulalitha Priyankara, S. Balasuriya, and E. Bollt, “Quantifying the role of folding in nonautonomous flows: The unsteady double-gyre,” *International Journal of Bifurcation and Chaos*, vol. 27, no. 10, p. 1750156, 2017.
- [98] M. R. Allshouse, G. N. Ivey, R. J. Lowe, N. L. Jones, C. Beegle-Krause, J. Xu, and T. Peacock, “Impact of windage on ocean surface Lagrangian coherent structures,” *Environmental Fluid Mechanics*, vol. 17, no. 3, pp. 473–483, 2017.
- [99] D. P. Foures, C. P. Caulfield, and P. J. Schmid, “Optimal mixing in two-dimensional plane poiseuille flow at finite pécelet number,” *Journal of Fluid Mechanics*, vol. 748, pp. 241–277, 2014.
- [100] F. Chillà and J. Schumacher, “New perspectives in turbulent Rayleigh-Bénard convection,” *The European Physical Journal E*, vol. 35, no. 7, pp. 1–25, 2012.
- [101] A. Klünker and K. Padberg-Gehle, “Robustness of coherent sets computations,” in *Proceedings of the 9th European Nonlinear Dynamics Conference, Budapest, Hungary*, pp. 25–30, 2017.
- [102] E. Ott, *Chaos in dynamical systems*. Cambridge University Press, 2002.
- [103] R. R. Coifman and S. Lafon, “Diffusion maps,” *Applied and computational harmonic analysis*, vol. 21, no. 1, pp. 5–30, 2006.
- [104] B. Nadler, S. Lafon, R. R. Coifman, and I. G. Kevrekidis, “Diffusion maps, spectral clustering and reaction coordinates of dynamical systems,” *Applied and Computational Harmonic Analysis*, vol. 21, no. 1, pp. 113–127, 2006.
- [105] S. Lafon and A. B. Lee, “Diffusion maps and coarse-graining: A unified framework for dimensionality reduction, graph partitioning, and data set parameterization,” *IEEE transactions on pattern analysis and machine intelligence*, vol. 28, no. 9, pp. 1393–1403, 2006.

- [106] C. Schneide, P. P. Vieweg, J. Schumacher, and K. Padberg-Gehle, “Evolutionary clustering of Lagrangian trajectories in turbulent Rayleigh–Bénard convection flows,” *Chaos: An Interdisciplinary Journal of Nonlinear Science*, vol. 32, no. 1, p. 013123, 2022.
- [107] G. Froyland and P. Koltai, “Detecting the birth and death of finite-time coherent sets,” *arXiv preprint arXiv:2103.16286*, 2021.
- [108] T. G. Anderson, M. Bonnet, and S. Veerapaneni, “Quantifying mixing in arbitrary fluid domains: A padé approximation approach,” *Numerical Algorithms*, pp. 1–18, 2022.
- [109] S. Siegmund and P. Taraba, “Approximation of box dimension of attractors using the subdivision algorithm,” *Dynamical Systems*, vol. 21, no. 1, pp. 1–24, 2006.